System Design, Noise Reduction and Improved Dimension Reconstruction for High-Performance Ellipsometry

by

Bo Jiang

Submitted to the Department of Mechanical Engineering
in partial fulfillment of the requirements for the degree of

Doctor of Philosophy

at the

MASSACHUSETTS INSTITUTE OF TECHNOLOGY

February 2022

© Massachusetts Institute of Technology 2022. All rights reserved.

Author . . . .
Department of Mechanical Engineering
January 19, 2022

Certified by . . . .
Kamal Youcef-Toumi
Professor of Mechanical Engineering
Thesis Supervisor

Accepted by . . . .
Nicolas Hadjiconstantinou
Chairman, Department Committee on Graduate Theses

System Design, Noise Reduction and Improved Dimension Reconstruction for High-Performance Ellipsometry

by

Bo Jiang

Submitted to the Department of Mechanical Engineering
on January 19, 2022, in partial fulfillment of the
requirements for the degree of
Doctor of Philosophy

Abstract

The advancement in nano-manufacturing and many other industries calls for high-performance metrology and inspection methods. Nano-manufacturing has witnessed shrinking critical dimension and demonstrated mass production capability: the lithography process has reached 5nm node and could potentially reach 2nm node by 2024; one production line can produce 125 wafers in one hour, each 300mm in diameter. Therefore, the desired metrology method must be non-invasive to achieve full sample and batch inspection, have high resolution to keep up with the shrinking critical dimensions, and feature high speed to be compatible with high-throughput manufacturing needs.

Ellipsometry gains popularity due to its advantages of non-invasiveness, high speed, and high resolution. The technology is an important metrology and inspection tool in many industries. Ellipsometry is a major tool in new material characterization, and considered an important metrology method for the next generation of semiconductor devices in nano-manufacturing. In addition, the technology finds its application in biomedical detection and surface roughness estimation. The working principles of ellipsometry are as follows. An ellipsometer experimentally measures the samples' changing effects on a light beam's polarization state, quantified by ellipsometric parameters or a Mueller matrix. The experimental results are then fitted to an optical model to extract the sample's critical dimensions and/or optical properties.

This thesis improves the performance of ellipsometry through three aspects.

The first part of this thesis quantifies and mitigates the mixed Poisson-Gaussian noise induced errors to improve ellipsometer's measurement accuracy and precision. The measurement accuracy can be significantly affected by the existence of Poisson-Gaussian noise originated from detection and environment. This work characterizes and quantifies the noise through experiments on an in-house setup. Error propagation analysis is then performed to quantify the measurement error in terms of normalized Mueller matrix elements. The effects of system parameters on the Poisson-Gaussian noise induced errors are studied, including signal strength, the signal sampling fre-

quency, and the first-order coefficient between the signal variance and mean. This thesis then proposes a signal demodulation method in spectroscopic ellipsometry based on maximum likelihood, in order to reduce the effects of Poisson-Gaussian noise. The method accounts for the signal's statistical distribution and solves for the Fourier coefficients by maximizing the probability of the observed signal. The method's capability of achieving higher Mueller matrix accuracy as well as higher dimension precision is demonstrated.

The second part develops a reconstruction method for dimensions. The objective is to improve the dimension reconstruction precision and the reconstruction's sensitivity to changes in dimensions. The reconstruction algorithm along with weights' selection are formulated. The method assigns higher weights to the more important configurations, where the measurement is sensitive to dimension changes. The selection is based on partial derivatives of the Mueller matrix elements with respect to dimensions. Improved precision is demonstrated through experimental measurements of thin film standards and gratings.

The third part of this thesis shows the design and effectiveness of a Faraday effect-based photometric ellipsometer. The new instrument eliminates mechanical motions and enables high-speed and controllable modulation frequency. In addition, it features a linear relationship between the applied current and the rotation of the polarization plane and thus enables fast and easy demodulation. This thesis presents the design, data reduction and the calibration procedure. Air and thin film sample experiments validate the effectiveness of the prototype.

Thesis Supervisor: Kamal Youcef-Toumi
Title: Professor of Mechanical Engineering

Acknowledgments

I would first and foremost thank my advisor, Professor Kamal Youcef-Toumi. His insights were invaluable in every step of my research. I am deeply gratefully to him for continuously guiding me with his knowledge and efforts. While keeping me on a good track, he gave me the freedom to explore new ideas and believed in me. This cultivation of critical thinking will benefit me for a lifetime. He is a most caring advisor and a friend. His support and encouragement accompanied me throughout my time at MIT, especially when I was faced with challenges. I am lucky and proud to know and work with him.

I greatly appreciate my committee members for their time and invaluable feedback. When I took Professor Hunter's class in instrumentation, I was amazed at his depth and breadth of knowledge. His feedback and advice motivated me to pursue higher standards. I am also honored to have Professor Barbastathis on my committee. In his class, I was amazed at his deep understanding of knowledge from different disciplines and ability to unifying the disciplines. I greatly value his feedback and help.

I take this opportunity to express my gratitude to my sponsor, Wuxi Friedrich Measurement and Control Instruments. Only with their support can I finish this work. I sincerely thank Dr. Kai. It was a great experience to work him during the past few years.

I would like to thank Dr. Harrison Chin, our lab instructor during my times as a lab TA. His expertise and ability to convey knowledge to students set the example.

I would like to thank the Mechanical Engineering Department staff. I thank Ms. Barbra Williams and Ms. Dorothy Hanna especially for helping me navigate through MIT's purchasing system so I could have everything I needed for experiments. I thank Ms. Leslie Regan and Ms. Saana McDaniel for all the help since the day I was admitted to the department.

I would like to thank the entire Mechatronics Research Laboratory. I am always filled with joy when Joni brings pastries and holiday decorations to lab meetings. I thank my labmates and especially Amith, You, Iman, and Fangzhou. They are always open to discussions and ready to lend their expertise. I appreciate the supportive

environment where we share knowledge and grow together.

I am grateful for the company and support of my friends. Graduate school would not been so memorable without them. Dr. Yang's encouragement is a source of my confidence and helped me through difficult periods. I was lucky to have my apartment mates Di, Yi, Lei, Qifang, and Jing. Now we are in different cities, but our friendship stand distance. I thank Yu and Emily for all the fun time we had together.

I am blessed with my most wonderful parents. Because of their unconditional love and understanding, I always have the courage and passion to greet and enjoy life. I wish them every happiness.

Contents

1 Introduction **19**

1.1 Objective of High-Performance Ellipsometry 19

1.2 Background 22

1.3 Thesis Contributions and Outline 25

2 Quantification and Reduction of Poisson-Gaussian Noise Induced Errors in Spectroscopic Ellipsometry **27**

2.1 Introduction 27

2.2 Experimental Noise Characterization and Quantification 28

2.3 Quantification of Poisson-Gaussian Noise Induced Errors 32

2.3.1 Statistical Analysis 32

2.3.2 Monte Carlo Simulations 38

2.4 Maximum Likelihood-Based Signal Demodulation for Noise Mitigation 43

2.4.1 Review and Technical Gaps of Existing Demodulation and Noise-Mitigation Methods 44

2.4.2 Maximum Likelihood-Based Signal Demodulation 45

2.4.3 Monte Carlo Simulations 48

2.5 Conclusion 49

3 Dimension Reconstruction **53**

3.1 Introduction 53

3.2 Review of Dimension Reconstruction and Technical Gaps 54

3.3 Improved Dimension Reconstruction Method 55

3.3.1 Problem Formalism 55

3.3.2 Improved Dimension Reconstruction Sensitivity 56
3.4 Experimental Verification of Improved Sensitivity 56
3.4.1 Reconstructed Dimension 57
3.4.2 Thin Film Measurement 59
3.4.3 Grating Measurement 61
3.5 Conclusion 62

4 Faraday Effect-Based Photometric Spectroscopic Ellipsometry 65

4.1 Introduction 65
4.2 Background and Motivation 66
4.2.1 Motivation of Faraday Effect-Enabled Ellipsometry 66
4.2.2 Background 69
4.3 Design and Analysis 71
4.3.1 System Design 71
4.3.2 Data Reduction 76
4.3.3 System Calibration 78
4.4 Experimental Calibration and Measurement 80
4.4.1 Verdet Constant Calibration 80
4.4.2 Sample Measurement 82
4.5 Conclusion 84

5 Experiment Setup and Procedures 87

5.1 Introduction 87
5.2 Ellipsometer Setup 87
5.3 Faraday Rotator Integration 91
5.4 Experimental Procedure 92
5.4.1 Sample Mount 92
5.4.2 Motion Control 93
5.4.3 Data Collection 94
5.5 Summary 95

6 Conclusions & Recommendations **97**
6.1 Conclusions 97
6.2 Recommendations 99

A Supplementary Results **101**
A.1 Supplementary Results of Chapter 2 101
A.2 Supplementary Results of Chapter 3 104
A.3 Supplementary Results of Chapter 4 109

B Bill of Materials **111**

C Fundamental concepts in statistics and computation **117**
C.1 Statistics 117
C.2 Processes: 117
C.3 Computation methods 118

D Codes **119**

Nomenclature **143**

List of Figures

1-1 Dual rotating-compensator ellipsometry setup illustration 23

2-1 Temporal noise 30

2-2 Light intensity variance vs. mean 30

2-3 Cumulative density function of experimental and simulated processes 31

2-4 Integrated intensity histogram at 873 nm 31

2-5 Integrated intensities autocorrelation 32

2-6 SEM image of the grating sample 39

2-7 Histogram of normalized M_{33}^n values from simulations 39

2-8 Normal probability plot of normalized Mueller matrix values from simulations 40

2-9 Normal plot of M_{33} using 200 simulations 41

2-10 Averaged Mueller matrix elements converges 41

2-11 The induced measurement error increases with γ_1 42

2-12 Histogram of reconstructed pitch from a signal wavelength 50

3-1 Illustration of grating 59

3-2 Thin film sample 1 60

3-3 Experimental and fitted Mueller matrix spectrum of thin film sample 1 at 40° incident angle 60

3-4 Experimental and fitted Mueller matrix spectrum of thin film sample 3 at 40° incident angle 61

3-5 Mounted grating sample 62

3-6 AFM image of grating sample 62

3-7 Experimental and fitted Mueller matrix spectrum *TGZ2* at 40° incident angle . . . 62

4-1 Illustration of Faraday rotation . . . 69
4-2 Illustration of the designed Faraday rotator . . . 72
4-3 A single loop of the solenoid . . . 74
4-4 Setup illustration . . . 77
4-5 Verdet constant calibration setup . . . 81
4-6 Calibration curve at four wavelengths . . . 81
4-7 Wavelength dependency of Verdet constant . . . 82
4-8 Signal following performance . . . 83
4-9 Ellipsometer setup incorporating Faraday rotators . . . 83
4-10 Ellipsometric parameters' spectra of air . . . 84
4-11 Ellipsometric parameters' spectra of thin film . . . 85

5-1 In-house dual-rotating compensator ellipsometer . . . 88
5-2 DRCE in reflection mode . . . 88
5-3 DRCE in reflection mode zoomed . . . 89
5-4 Broadband and laser light sources . . . 89
5-5 Incident arm fixture . . . 90
5-6 Spectrometer . . . 90
5-7 Vertically aligned rotary stages . . . 90
5-8 6-DOF sample stage . . . 91
5-9 The ellipsometer at two different incident angles . . . 91
5-10 Glass holder . . . 92
5-11 A Faraday rotator in light path . . . 92
5-12 Mounted thin film sample . . . 93
5-13 Mounted grating sample . . . 93
5-14 Motion control of rotary mounts. . . . 94
5-15 DFT analysis of measurement . . . 94
5-16 Motion control of the stage and the light arms . . . 95
5-17 Trigger from controller to spectrometer . . . 96

A-1 Histogram of normalized air M_{33}^n values from simulations 101
A-2 Normal probability plot of normalized air MM from simulations . . . 102
A-3 Normal plot of M_{33} using 200 simulations 103
A-4 Averaged Mueller matrix elements converges 103
A-5 The induced measurement error increases with γ_1 104
A-6 Simulated Mueller matrix spectrum of a grating sample with a step height of 1250 nm 105
A-7 Color map 105
A-8 Mounted thin film standards 106
A-9 Experimental and fitted Mueller matrix spectrum of thin film sample 1 at 50° incident angle 106
A-10 Experimental and fitted Mueller matrix spectrum of thin film sample 1 at 60° incident angle 107
A-11 Experimental and fitted Mueller matrix spectrum of thin film sample 2 at 40° incident angle 107
A-12 Experimental and fitted Mueller matrix spectrum of thin film sample 2 at 50° incident angle 108
A-13 Experimental and fitted Mueller matrix spectrum of thin film sample 2 at 60° incident angle 108
A-14 Experimental and fitted Mueller matrix spectrum of thin film sample 3 at 50° incident angle 109
A-15 Experimental and fitted Mueller matrix spectrum of thin film sample 3 at 60° incident angle 110

B-1 Isometric, side, and back view of the 6-DOF sample stage 115
B-2 Mounted polarizer 116
B-3 Mounted compensator 116
B-4 Solenoid 116
B-5 Glass rod and its holder 116

List of Tables

2.1 Percent reduction in Mueller matrix mean absolute error 49

3.1 Reconstructed dimensions of thin film standards and a grating sample 58

4.1 Faraday rotator design parameters 73

4.2 Faraday rotator design criterion 73

B.1 Bill of materials - light sources and detection system 111

B.2 Bill of materials - major optical components 111

B.3 Bill of materials - motors and motion control components 112

B.4 Bill of materials - Faraday rotators and the required electronics . . . 112

B.5 Bill of materials - construction components 112

B.6 Bill of materials - optical cage system construction components 113

B.7 Bill of materials - fasteners 114

B.8 Bill of materials - samples 114

Listings

D.1 Spectrometer data parser 120
D.2 Monte Carlo simulations of broadband light source 121
D.3 Monte Carlo simulations at a single wavelength 124
D.4 Top-level file of DRCE processing 130
D.5 Thin film thickness reconstruction 132
D.6 Verdet constant calibration 134
D.7 Faraday effect-enabled photometric ellipsometer codes 137

Chapter 1

Introduction

1.1 Objective of High-Performance Ellipsometry

The advancement in many industries calls for high-performance metrology and inspection methods. One major application requiring such a metrology method is nanomanufacturing. The field has been experiencing rapid advancements. A prominent advancement is the shrinking critical dimensions: lithography had a linewidth of 10 nm back in year 2016, and now has achieved 5 nm node, and is expected to reach 2 nm by 2024 [1]. In addition, the manufacturing speed has increased. Wafer mass production has been demonstrated and one line can produce 125 wafers in an hour, up to 300 mm in diameter [2]. It is also a multi-stage process [3] and increase the necessity of high-speed or high-throughput. The quality control in the industry renders challenges to the metrology and inspection methods. And more importantly, if full inspection is needed, the method have to be fast and non-invasive to avoid sample damage. Nowadays the golden standard is the scanning electron microscopy, which can only perform selective examination due to the cost and the complex sample preparation. Current inspections also rely a lot on functionality test. In manufacturing process, a desired method will enable inline batch inspection instead of selective examination. Such a method can be integrated with the manufacturing process so it can detect defects even at intermediate stages. For this, the method needs to be compatible with large-range measurements.

The metrology or inspection method is important in many other industries and applications in addition to nano-manufacturing. One example is surface roughness examination. Currently painting surfaces such as those on luxury cars rely entirely on human visual and haptic inspection. To automate the process, the inspection method must be capable of large range and high speed. The thin film thickness measurement application requires a metrology method to be of high resolution and non-invasive to avoid sample damage. Another application lies in medical testing, which generally favors non-invasiveness. An example is glucose measurement through optical methods. Finally, the material characterization application also requires high precision and non-invasiveness.

The above-mentioned applications require high-performance metrology methods. Firstly, to achieve full sample and batch examination, the method must be non-invasive. Secondly, the metrology needs high resolution to keep up with the shrinking critical dimensions. Thirdly the method needs to be of high speed to be compatible with high-throughput processes, and the multi-stage processes increase the workload and further promote the necessity of high speed.

Many of the existing metrology methods do not meet the industries' needs. A lot of high-resolution methods are invasive. The commercial atomic force microscopes (AFM) achieve angstrom lateral resolution, but are slow and for small-range applications. Recent development on high-speed imaging AFM enabled 37 Hz on 50 μm scanning size [4–7], far below the large-throughput and large-range requirements. Moreover, AFM is invasive in its contact mode, where the mechanical contact between the probe and the sample introduces wear to the tip and the sample. Scanning Electron Microscopy (SEM) [8,9] and Transmission Electron Microscopy [10,11] achieve nm resolution by scanning with a focused beam of electrons, but is invasive as the scanning process leaves the sample radioactive. The method also requires vacuum environment and is time-consuming in sample preparation. In addition, the method only acquires 2D images. Coherent diffraction imaging uses X-rays or electrons [12,13] to achieve high resolution, and the high-energy beam could leave the sample radioactive. The method is also costly for high-volume and large-range in-

spection. Fluorescence labeling-based methods such as stimulated emission depletion (STED) [14,15] and photoactivated localization microscopy (PLAM) [16,17] are limited to large molecular-weight samples. Capacitive and optical methods are two important non-invasive metrology methods, but often do not have the desired resolution. A scanning electrostatic force microscope is an example of capacitive sensing [18,19]. Optical methods are are subject to the diffraction limit. Conventional structured illumination improves the diffraction limit by 2 times and is incapable of resolving the critical dimensions in nano-manufacturing [20, 21]. Near-field methods capture evanescent wave to get the diffraction-free information [22–24]. However, the optical probe must be kept at a distance under one wavelength from the sample surface, and has the disadvantage of slow scanning. Near field and far-field superlens and hyperlens have demonstrated resolving lines 125-nm apart at a wavelength of 365nm [25], but is not ready for wafer critical dimension inspection [26, 27].

Ellipsometry has the potential of meeting the industries' needs. The method is inherently non-invasive, compatible with large-throughput applications, and has the potential of high resolution. The method also has the additional benefits of being able to measure multi-layer and buried structures. Ellipsometry is suitable for a large range of applications, including metrology in nano-manufacturing [28–33], thin film thickness measurement [34–36], surface roughness estimation, and medical applications [37]. Moreover, the method can measure the critical dimensions of multi-layer and buried structures. The technology also finds its application in underwater imaging [38–40] and astronomy [41,42]. The working principles of ellipsometry are as follows. An ellipsometer experimentally measures the samples' changing effects on a light beam's polarization state. The experimental results are then fitted to an optical model to extract the sample's critical dimensions and/or optical properties, and the feature dimension below the diffraction limit can be extracted [43].

The goal of this thesis is to improve the performance of ellipsometry to make it more suitable for non-invasive, high-resolution, and high-throughput applications. Ellipsometry, in its current form, is incapable of industrial requirements and needs further study. Among factors affecting the ellipsometry performance, there are two

major sources of inaccuracy and imprecision: the effects of optical signal randomness causes inaccuracy and impression [37]; the limited sensitivity in inverse problem limits the dimension reconstruction precision. Among different configurations, rotating-component ellipsometry is the most common type of commercial product and is widely used [44, 45], the speed of which is fundamentally limited by the motor speed. The goal of this thesis is therefore to focus on the above-mentioned problems and improve ellipsometry performance.

1.2 Background

Ellipsometry has been applied in a plethora of industries as a metrology and inspection tool. The technology gains popularity due to its advantages of non-invasiveness, high-speed, and high-resolution. One major application lies in new material development, where material characterization relies heavily on ellipsometry [46–51]. The technology has been successful in thin film thickness measurement, and is considered a promising metrology tool for the next generation of semiconductor devices in nano-manufacturing industry [52–54]. In addition, ellipsometry finds its application in other fields including biomedical detection [37,55,56], surface inspection and roughness estimation [57,58] and environment monitoring such as dust formation in a large plasma device [59].

An ellipsometer measures the sample's changing effects on a light's polarization state, quantified by ellipsometric parameters or a Mueller matrix. There are ellipsometers based on temporal polarization changes [44] or spatial polarization distribution [59–62], and time-varying or spatially varying light intensity signal are obtained respectively during measurement.

Rotating-component ellipsometers fall under the category of temporal polarization change-based ellipsometers. These have been the most popular type of commercial ellipsometry products [44, 45], due to their simple design and implementation, wide spectral range, and capability of parallel broadband wavelength scanning for high speed in spectroscopic ellipsometry. The latest development features spectroscopic Mueller matrix ellipsometry [46], capable of parallel broadband wavelength scanning

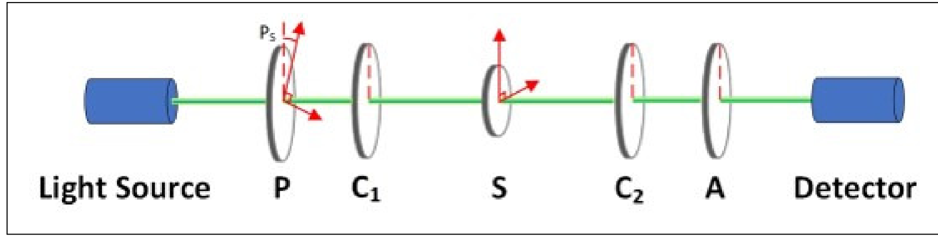

(a) DRCE setup illustration in transmission mode

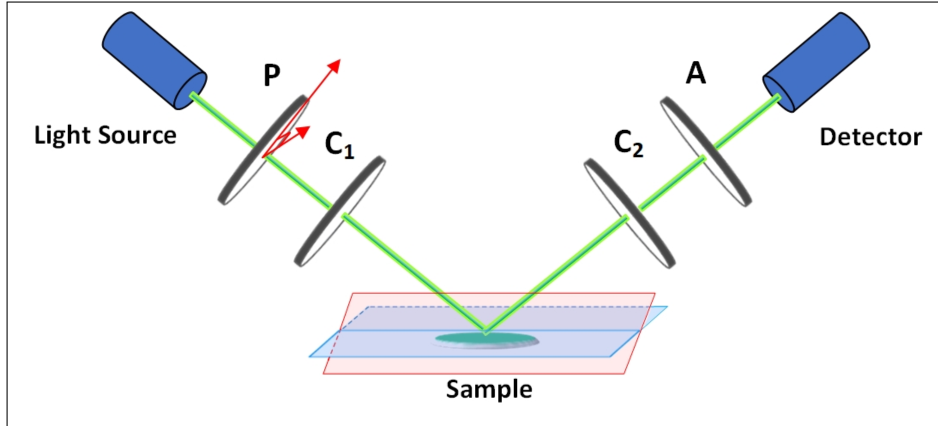

(b) DRCE setup illustration in reflection mode

Figure 1-1: Dual rotating-compensator ellipsometry setup illustration

as well as characterizing complex samples exhibiting inhomogeneity and anisotropy. Recently in academia, the Mueller matrix ellipsometer has been increasingly used to characterize anisotropic materials. In addition, the semiconductor industry is developing towards finer dimension and higher complexity from 2D to 3D, also calling for Mueller matrix measurements. Spectroscopic Mueller matrix ellipsometry is mostly achieved through dual-rotating component compensator ellipsometers (DRCE). Figure 1-1 illustrates the device in its transmission mode and reflection mode. The setup consists of a light source, an incident arm containing a polarizer (P) and the first rotating compensator (C_1), the mounted sample (S), a reflective arm containing the second rotating compensator (C_2) and an analyzer (A), and a detector. The azimuthal plane is marked by the attached coordinate. In transmission mode, the light beam goes through the components, and the output Stokes vector is the product of the input Stokes vector, the polarizing components' Mueller matrices, and the rotation matrices. During the experiment, the two compensators rotate at constant speeds at a fixed ratio. The output light intensity is a time-varying spectrum, and the time-domain

intensity output is a sum of harmonics at any specific wavelength. The principle is the same for the reflective mode.

Photoelastic modulator (PEM)-based ellipsometry is a well-established ellipsometry configuration. A PEM is excited at its resonance frequency, ranging from 20 kHz to 100 kHz and typically 50 kHz. The modulator acts as an oscillating retarder to provide the necessary polarization manipulation together with other polarizing components. PEMs have several advantages including high speed, resistance to low-frequency noise, low operating power requirements, and greater numerical aperture. On the other hand, PEMs have limitations. The high modulation frequency poses challenges on the detection system [45], and a PEM-based ellipsometry cannot achieve parallel measurement at multiple wavelengths ellipsometry for the same reason.

Ellipsometers enabled by magneto-optical components were developed in early years of ellipsometry. The Faraday effect is a phenomenon where a polarization plane is rotated in a material when a magnetic field is applied, and the rotation angle is proportional to the magnetic field projected on the light propagation direction. The first real-time spectroscopic ellipsometer took advantage of Faraday rotators [63]. The ellipsometer uses a "null" configuration, where the minimum irradiance is determined as a function of the azimuthal angle of the polarizer and the analyzer as well as the Faraday rotation angle, and the ellipsometric parameters are then determined [63–67]. The configuration has its drawbacks. Firstly, the configuration does not allow parallel measurement at multiple wavelengths. Secondly, the measurement is susceptible to random noises in determining the nulling position, especially when the light source is weak. In contrast, later development of photometric ellipsometers components is capable of parallel wavelength scanning [45] and can work with weak light sources [68].

There are temporal polarization changing ellipsometers based electro-optical components. The usage of liquid-crystal variable retarder (LCVR) was introduced in Mueller matrix ellipsometry in 2000 [69] to enable compact design [70]. The retardance of the electro-optical component changes with the voltage applied to it. Due to the voltage-retardance nonlinearity, most studies select a few voltage values to perform calibration and measurements. Because measurements are only taken at

discrete retardance values instead of a continuous range of retardance, the instrumentation is potentially more sensitive to calibration errors and random noises. To counter this problem, some studies focused on measuring the voltage-retardance relationship and the continuously variable voltage. Many earlier setups used only one or few wavelengths [69, 71, 72] due to wavelength dependency. Later research started to use broadband light sources and proposed calibration methods [73, 74]. There have also been studies to optimize the ellipsometer setups using LCVR [75, 76], and a Mueller matrix error lower than 0.5% has been reported for one wavelength on a polarizer sample [73]. In summary, excellent works have advanced the application of electro-optical components in ellipsometry, but the voltage-retardance nonlinearity and sensitivity to alignment errors remain challenging.

1.3 Thesis Contributions and Outline

This thesis improves the performance of ellipsometry through three contributions.

The first contribution lies in the quantification and mitigation of errors induced by mixed Poisson-Gaussian noise present in the ellipometer system. The measurement accuracy of ellipsometry could be significantly affected by the existence of Poisson-Gaussian mixed noise. This thesis first characterizes and quantifies the noise through experiments on an in-house setup. This is then followed by an error quantification in terms of normalized Mueller matrix calculation through error propagation analysis. Finally the thesis proposes an approach to ellipsometry demodulation, in order to reduce the effects of Poisson-Gaussian noise. The method is based on maximum likelihood, and takes into account the statistical model of the signal randomness.

The second contribution is an improved dimension reconstruction method. After the experimental measurement is obtained, the result is fitted to an optical model for dimension reconstruction. A method is developed to improve the reconstruction's sensitivity to changes in dimensions, and in turn improve the precision of the dimension reconstruction.

The third contribution is the design and implementation of Faraday effect-enabled photometric ellipsometry. The design utilizes Faraday effect for polarization manipu-

lation to overcome the speed limit from motor rotation in rotating-component ellipsometer. The design has the additional benefits of eliminating mechanical rotation, vibration, and reduces the induced errors.

The rest of this thesis is organized as follows. In Chapter 2, the error quantification and mitigation is presented. In Chapter 3, a reconstruction method is proposed as well as its experimental verification. Chapter 4 presents the design and validation of the proposed Faraday effect-based photometric ellipsometry. The experiments are described in detail in Chapter 5. Chapter 6 provides the conclusion and recommendations.

Chapter 2

Quantification and Reduction of Poisson-Gaussian Noise Induced Errors in Spectroscopic Ellipsometry

2.1 Introduction

The measurement accuracy of ellipsometry can be significantly affected by the existence of Poisson-Gaussian mixed noise. This chapter focuses on rotating-component ellipsometry and the Faraday effect-enabled photometric ellipsometer proposed in Chapter 4.

This chapter achieves three goals. The first goal is noise characterization and quantification through experiments on an in-house setup.

The second goal is a detailed error characterization and quantification in terms of normalized Mueller matrix in the presence of Poisson-Gaussian noise. Specifically, the distribution of the normalized Mueller matrix elements error is derived, accounting for the nonlinear error propagation occurring at the normalization step. The derivation is verified with Monte Carlo simulations. The derivation considers system parameters including the signal strength, the signal sampling frequency, and the correlation between the noise and signal. The effects of the parameters on the induced errors are also studied.

The third goal of this chapter is the development of a maximum likelihood method to spectroscopic ellipsometry demodulation, in order to reduce the effects of Poisson-Gaussian noise. Compared to the most commonly used method of DFT, the major improvement of the proposed method is that it accounts for the signal's probabilistic distribution induced by the Poisson-Gaussian noise. The method then solves for the Fourier coefficients by maximizing the probability of observed signal. he improved performance of the method is demonstrated against DFT in terms of Mueller matrix measurement accuracy and sample dimension reconstruction accuracy.

The rest of this chapter is organized as follows. In Section 2.2, the experimental noise characterization and quantification are presented. Section 2.3 contains the analysis of the induced normalized Mueller matrix error, and the verification of the analysis through Monte Carlo simulations. Section 2.4 presents the proposed maximum likelihood method to signal demodulation, and the method's capability of achieving higher Mueller matrix accuracy as well as higher dimension reconstruction accuracy and precision. The chapter's conclusion is in Section 2.5.

2.2 Experimental Noise Characterization and Quantification

In this section, the experimental noise characterization and quantification is presented.

To characterize and quantify the noise, measurements are taken on an in-house dual rotating-compensator ellipsometer (DRCE) setup. Fig. 1-1 is an illustration of the device. The setup consists of a light source, a polarizer (P), the first compensator (C_1), a sample (S), the second compensator (C_2), an analyzer (A), and a detector. Fig. 1-1a and 1-1b show the setup in its transmission and reflective mode respectively. The coordinates attached to the optical components indicate the azimuthal angles. The description and figures of the in-house setup is shown in Chapter 5. During the experiment, the setup is kept stationary in its transmission mode. The integrated light intensity depends on the integration time, and light spot size, varied by adjusting iris aperture. Given the light source in the setup, the intensity is also

different at different wavelengths. Intensities are collected at different combinations of integration time, spot size, and wavelength. The spectrometer reads a spectrum at different wavelengths, and 3000 integrated intensities are taken consecutively. In this experiment, results from 1256 wavelengths are analyzed, ranging from 450 nm to 1000 nm. The same procedure is repeated for an integration time of 30 ms and 100 ms, and at several light source intensities. The integration time can be changed in the user interface software of the spectrometer.

The experiments indicate a mixed Poisson-Gaussian noise, and the distribution properties are obtained. Ideally the integrated intensities are identical given the same wavelength, integration time, and light source intensity. However the integrated intensities involve noise. Fig. 2-1 shows 3000 consecutive measurements at 873 nm as an example. The temporal noise is observed. Fig. 2-2 plots the signal variance versus its mean and a linear fit. For each set of parameters, the variance and mean are calculated from 3000 integrated intensities. The variance is observed to be linearly correlated with the mean. The rest of this chapter is based on this uncertainty measurement. To better understand the noise, the cumulative density function is plotted for the experimental data and a simulated process, as in Fig. 2-3. The simulated process is a mixed Poisson-Gaussian process, where the variable of the Poisson process is multiplied by a constant. The blue line is from the experimental data, and the dashed red line is from the simulated Poisson-Gaussian process. The match indicate the signal collection approximating a Poisson-Gaussian process. The first-order behavior originates from a Poisson process in photon detection. The first-order coefficient is 0.32, representing the property of the CCD detector. The offset magnitude is 51.95 from fitting, owing to a Gaussian process. Higher orders of the variance-mean curve represent other noise sources [77]. In this thesis, Poisson-Gaussian is recognized as the dominant random noise in the setup, and the focus of this chapter is the study of its effects in signal processing and mitigation.

In the case of mixed Poisson-Gaussian noise, the variance of each integrated intensity is linearly related with its magnitude as in Eq. (2.1), where σ_k^2 is the variance associated with the k_{th} integrated intensity. Both coefficients γ_1 and γ_2 are constants.

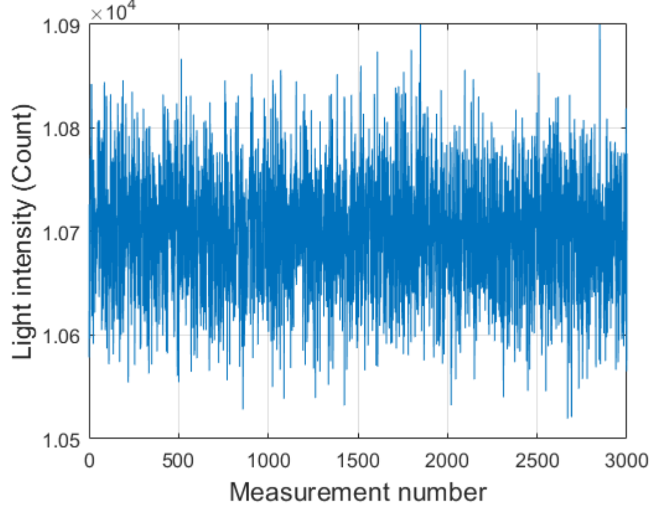

Figure 2-1: Temporal noise

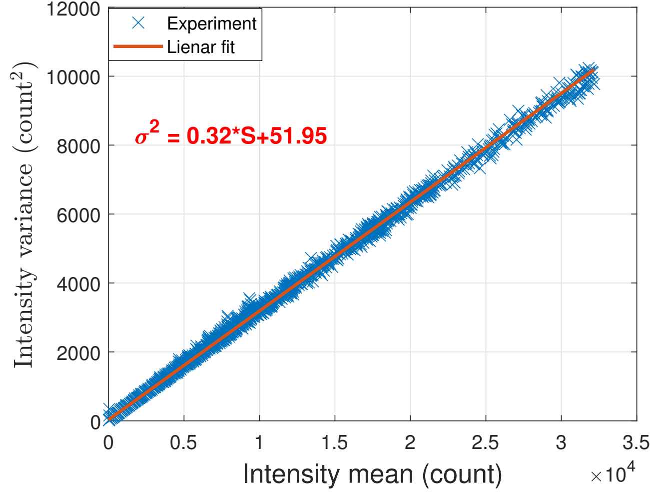

Figure 2-2: Light intensity variance vs. mean

The offset γ_2 represents Gaussian noise. The first order coefficient γ_1 originates from the photon shot noise. When the spectral irradiance incidents on the photodetector, the generated photoelectrons follow a Poisson distribution. The scaling factor γ_1 represents the integrated intensity being proportional to the generated photoelectrons [78]. To further reduce the variance, binning N pixels improves the signal-to-noise ratio from $\sqrt{\mathrm{S}}$ to $\sqrt{\mathrm{N} \cdot \mathrm{S}}$ and the variance-to-mean ratio retains its linear behavior.

$$\sigma_k^2 = \gamma_1 \cdot E[S_k] + \gamma_2 \tag{2.1}$$

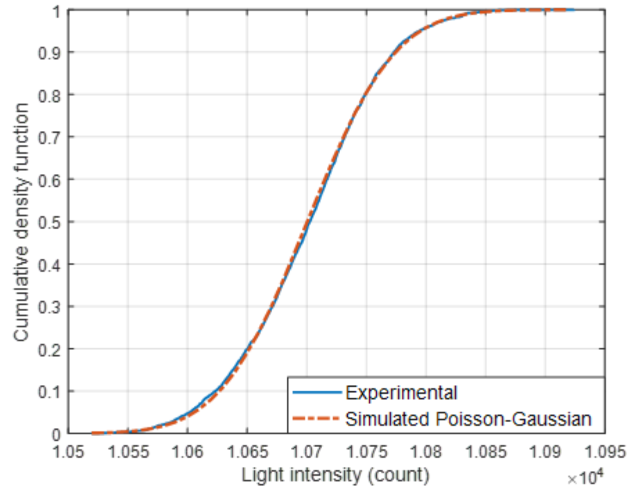

Figure 2-3: Cumulative density function of experimental and simulated processes

As the number of experiments increases, each integrated intensity follows a Gaussian distribution according to the Central Limit Theorem (CLT). Fig. 2-4 shows the histogram of integrated intensities at 873 nm using a 30 ms integration time and fixed light source intensity. The probability density function is calculated using $MATLAB$ function *normpdf*. The integrated intensities follow a Gaussian distribution according to the Central Limit Theorem. In Fig. 2-5, the noise's auto-correlation is plotted for a lag of 1 to 100 integration period, and has a maximum magnitude of 0.043, indicating the noise from integrated intensities are independent from or very weakly correlated with each other.

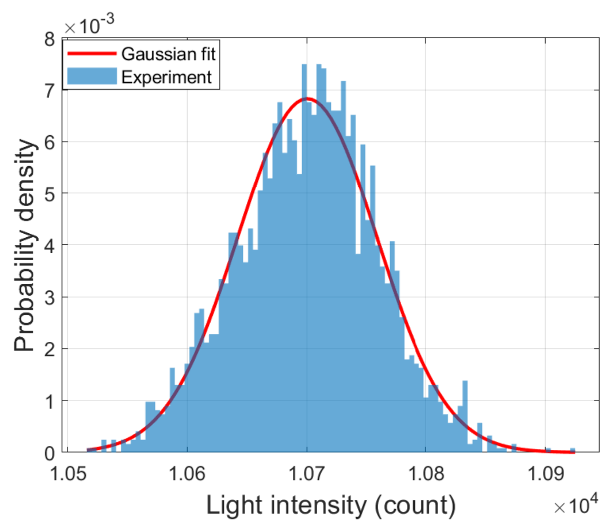

Figure 2-4: Integrated intensity histogram at 873 nm

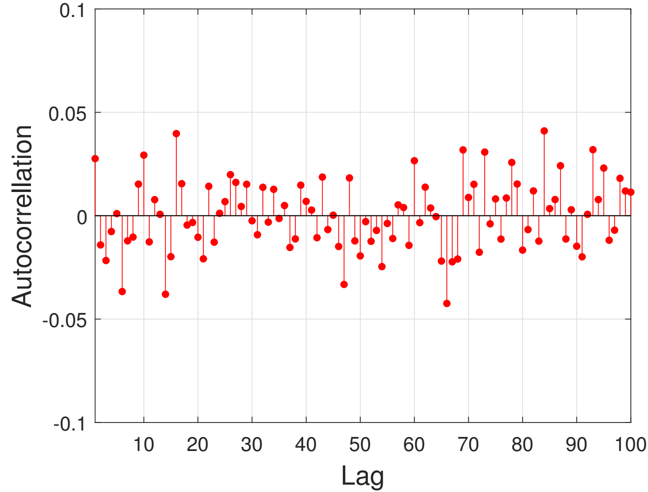

Figure 2-5: Integrated intensities autocorrelation

2.3 Quantification of Poisson-Gaussian Noise Induced Errors

In this section, the quantification of the measurement uncertainty and errors induced by mixed Poisson-Gaussian noise is presented. The uncertainty and errors are quantified by normalized Mueller matrix and reconstructed dimensions. In Subsection 2.3.1, the statistical analysis of the error quantification is presented. First, the distributions of the normalized Mueller matrix elements are derived. The properties of the distributions are also derived as functions of three parameters: light intensity, sampling frequency, and the first-order coefficient between the signal variance and mean. Second, the expected mean absolute error of the Mueller matrix elements are then computed. In Subsection 2.3.2, Monte Carlo simulations are carried out to verify the assumptions and results in the statistical analysis.

2.3.1 Statistical Analysis

In this subsection, the statistical analysis of the induced error on normalized Mueller matrix is performed.

The linear transformation between the measured signal and unnormliazed Mueller matrix elements is first established. The transformation could be decomposed into two parts: the linear transformation from the signal to the Fourier coefficients, and the linear transformation from the Fourier coefficients to the unnormalized Mueller matrix elements. As to the first part, the direct output of a rotating-component spectroscopic ellipsometry is a time-varying spectrum resulting from the rotation of designated polarizing components. The light intensity is a sum of harmonics at any specific wavelength as in Eq. (2.2), where $I(t)$ is the light intensity exiting the light path at time t, I_o is the DC term, $2n$ is the harmonic order, $2N$ is the maximum harmonic order, α_{2n} and β_{2n} are the Fourier coefficients associated with order $2n$, and ω is the rotating components' fundamental frequency. During experiments, the polarizing components rotate at a constant speed. Broadband waveform integration is commonly adopted: the spectrometer measures the integrated intensity over a period of time. Integrating Eq. (2.2) gives the measured signal in Eq. (2.3), where S_k is the k_{th} integrated intensity, t_1 and t_2 are the starting and ending time of the integration period, and Δt is the integration duration. Throughout this thesis, vectors and matrices will be in bold.

$$I(t) = I_o + \sum_{n=1}^{N} [\alpha_{2n}\cos(2n\omega t) + \beta_{2n}\sin(2n\omega t)] \tag{2.2}$$

$$S_k = \int_{t_1}^{t_2} I(t)dt \tag{2.3a}$$

$$\begin{aligned} &= \Delta t \cdot I_o + \sum_{n=1}^{N} \frac{\sin(n\omega\Delta t)}{n\omega} \cos[n\omega(2k-1)\Delta t]\alpha_{2n} \\ &\quad + \sum_{n=1}^{N} \frac{\sin(n\omega\Delta t)}{n\omega} \sin[n\omega(2k-1)\Delta t]\beta_{2n} \end{aligned} \tag{2.3b}$$

Each measured light intensity is therefore a linear function of the DC term and the Fourier coefficients, which are to be determined during signal demodulation. Up to now, the formalism follows the well-defined Hadamard equation method [79]. Define

a column vector $\boldsymbol{\theta}$ consisting of the DC term and the Fourier coefficients as in Eq. (2.4). These are all the parameters to be solved for in signal demodulation. Eq. (2.3) can then be rewritten as Eq. (2.5), where $\boldsymbol{\phi}_k$ is the coefficient vector associated with the k_{th} integrated intensity. The coefficient vector associated with each measurement is explicitly written out in Eq. (2.6).

$$\boldsymbol{\theta} = [I_o, \alpha_2, ..., \alpha_{2N}, \beta_2, ..., \beta_{2N}]^T \tag{2.4}$$

$$S_k = \boldsymbol{\phi}_k^T \boldsymbol{\theta} \tag{2.5}$$

$$\begin{aligned}\boldsymbol{\phi}_k = [\Delta t, &\frac{\sin(\omega\Delta t)}{\omega}\cos[\omega(2k-1)\Delta t], ..., \frac{\sin(n\omega\Delta t)}{n\omega}\cos[n\omega(2k-1)\Delta t], ..., \\ &\frac{\sin(N\omega\Delta t)}{N\omega}\cos[N\omega(2k-1)\Delta t], \frac{\sin(\omega\Delta t)}{\omega}\sin[\omega(2k-1)\Delta t], ..., \\ &\frac{\sin(n\omega\Delta t)}{n\omega}\sin[n\omega(2k-1)\Delta t], ..., \frac{\sin(N\omega\Delta t)}{N\omega}\sin[N\omega(2k-1)\Delta t]]^T\end{aligned} \tag{2.6}$$

Integrated light intensities are measured consecutively with the same integration time, leading to a system of linear equations as in Eq. (2.7), where $\mathbf{S}$ is the integrated intensities vector, and K is the number of integrated intensities in one optical period. The elements in coefficient matrix $\boldsymbol{\Phi}$ involve the rotation speed and sampling frequency. The linear transformation between the integrated light intensities signal and the Fourier coefficients is thus established.

$$\mathbf{S} = \begin{bmatrix} S_1 & ... & S_k & ... & S_K \end{bmatrix}^{\mathrm{T}} \tag{2.7a}$$

$$\boldsymbol{\Phi} = \begin{bmatrix} \boldsymbol{\phi}_1 & ... & \boldsymbol{\phi}_k & ... & \boldsymbol{\phi}_K \end{bmatrix}^{\mathrm{T}} \tag{2.7b}$$

$$\mathbf{S} = \boldsymbol{\Phi} \cdot \boldsymbol{\theta} \tag{2.7c}$$

A linear relationship can further be established between the unnormalized Mueller matrix elements and the integrated light intensities signal. The unnormalized Mueller matrix elements are solved from $\boldsymbol{\theta}$ through a system of linear equations, well established in literature [80]. Here the transformation is written in Eq. (2.8). The elements of the coefficient matrix $\mathbf{B}$ involve the optical components' initial positions and the

compensators' retardance. Eq. (2.9) describes the demodulation, a linear transformation from the integrated intensities to unnormalized Mueller matrix elements. Here the unnormalized Mueller matrix is reshaped to a 16 by 1 column vector $\mathbf{M}^u$. The linear regression solution is given in Eq. (2.9) and (2.10).

$$\boldsymbol{\theta} = \mathbf{B} \cdot \mathbf{M}^u \tag{2.8}$$

$$\mathbf{M}^u = \mathbf{A} \cdot \mathbf{S} \tag{2.9}$$

$$\mathbf{A} = (\mathbf{B}^T\mathbf{B})^{-1} \cdot \mathbf{B}^T \cdot (\mathbf{\Phi}^T\mathbf{\Phi})^{-1} \cdot \mathbf{\Phi}^T \tag{2.10}$$

An unnormalized Mueller matrix element can be modeled as following a Gaussian distribution. From Eq. (2.9), an unnormalized Mueller matrix element is a linear combination of integrated intensities. Given the assumption of independent integrated intensities and Gaussian distribution of each integrated intensity, the unnormalized Mueller matrix elements follow Gaussian distributions, as in Eq. (2.11), where M_k^u is the k_{th} element in $\mathbf{M}^u$, $\mathbf{A}$ is the k_{th} row of $\mathbf{A}$, $\mathbf{S}_n$ is a vector consisting of the noisy integrated intensity variables.

$$M_k^u = \mathbf{A}_k \cdot \mathbf{S}_n \tag{2.11}$$

The properties of error distribution are derived for each normalized Mueller matrix element. The Mueller matrix is only independent of the incidence intensity after normalization. When the matrix is normalized to the first element in the first row as in Eq. (2.12), the normalized Mueller matrix describes the change in polarization state without accounting for the change in light intensity. Theoretically, the first element in the first row of the unnormalized Mueller matrix is the largest number in the unnormalized Mueller matrix. In Eq. (2.12), $\mathbf{M}^n$ is the column vector consisting of the normalized Mueller matrix elements, and M_1^u is the first element in $\mathbf{M}^u$.

$$\mathbf{M}^n = \frac{\mathbf{M}^u}{M_1^u} \tag{2.12}$$

Combined with Eq. (2.9), the normalized Mueller matrix elements are given in Eq.

(2.13), where $\mathbf{A}_1$ is the first row of $\mathbf{A}$.

$$M_k^n = \frac{\mathbf{A}_k \cdot \mathbf{S}_n}{\mathbf{A}_1 \cdot \mathbf{S}_n} \tag{2.13}$$

Each element in the normalized Mueller matrix therefore follows a ratio distribution from the quotient of two Gaussian variables, or a Cauchy distribution, which does not have a finite mean or variance. However, all normalized Mueller matrix elements pass a Lilliefors test with 1% significance level in simulations, and therefore can be approximated with a Gaussian distribution. This approximation is verified through Monte Carlo simulations in the next subsection. The properties of the approximated Gaussian distributions are derived as follows. The mean and variance of the numerator and denominator are derived in Eq. (2.14) and Eq. (2.15) respectively, where Q_N denotes the numerator of the normalized Mueller matrix elements and is a scalar, $\mu_{Q_N}$is the mean of the numerator, $\sigma_{Q_N}^2$ is the variance of the numerator, Q_D denotes the denominator of the normalized Mueller matrix elements and is a scalar, μ_{Q_D} is the mean of the denominator, and $\sigma_{Q_D}^2$ is the variance of the denominator. In the equations, $\Delta\mathbf{S}$ is a K by 1 vector representing the noise, which is the difference between the clean and noisy signal, $\cdot$ represents the inner product, and $\odot$ represents element-wise multiplication. The order of operations in the equations is: parentheses, element-wise multiplication, inner product, and addition and subtraction.

$$Q_N = \mathbf{A}_k \cdot \mathbf{S}_n = \mathbf{A}_k(\mathbf{S} + \Delta\mathbf{S}) \tag{2.14a}$$

$$\mu_{Q_N} = \mathbf{A}_k \cdot \mathbf{S} \tag{2.14b}$$

$$\sigma_{Q_N}^2 = \mathbf{A}_k \odot \mathbf{A}_k \cdot \sigma_S^2 = \mathbf{A}_k \odot \mathbf{A}_k \cdot (\gamma_1 \cdot \mathbf{S} + \gamma_2) \tag{2.14c}$$

$$Q_D = \mathbf{A}_1 \cdot \mathbf{S}_n = \mathbf{A}_1(\mathbf{S} + \Delta\mathbf{S}) \tag{2.15a}$$

$$\mu_{Q_D} = \mathbf{A}_1 \cdot \mathbf{S} \tag{2.15b}$$

$$\sigma_{Q_D}^2 = \mathbf{A}_1 \odot \mathbf{A}_1 \cdot (\gamma_1 \cdot \mathbf{S} + \gamma_2) \tag{2.15c}$$

The covariance of the numerator and denominator is calculated in Eq. (2.16), where $cov(Q_N, Q_D)$ is the covariance function, $E[\cdot]$ is the expected value, A_{kj} is the element of $\mathbf{A}$ in the k_{th} row and j_{th} column, similarly A_{1i} is the element of $\mathbf{A}$ in the first row and the i_{th} column, A_{ki} is the element of $\mathbf{A}$ in the k_{th} row and the i_{th} column, and $\mathcal{N}$ refers to a normal distribution. The simplification in Eq. (2.16c) is based on independent noise from each integrated light intensity. The expectation in Eq. (2.16e) is obtained from the property of a Chi-squared distribution.

$$cov(Q_N, Q_D) = E\left[(\mathbf{A}_1\mathbf{S}_n)(\mathbf{A}_k\mathbf{S}_n)\right] - E\left[\mathbf{A}_1\mathbf{S}_n\right]E\left[\mathbf{A}_k\mathbf{S}_n\right] \tag{2.16a}$$

$$= E\left[(\mathbf{A}_1\mathbf{S})(\mathbf{A}_k\Delta\mathbf{S}) + (\mathbf{A}_1\Delta\mathbf{S})(\mathbf{A}_k\mathbf{S}) + (\mathbf{A}_1\Delta\mathbf{S})(\mathbf{A}_k\Delta\mathbf{S})\right] \tag{2.16b}$$

$$= E\left[(\sum_{i=1}^{n} A_{1i}\Delta S_i)(\sum_{j=1}^{n} A_{kj}\Delta S_j)\right] \tag{2.16c}$$

$$= \sum_{i=1}^{n} E\left[(A_{1i}\Delta S_i)(A_{ki}\Delta S_i)\right] \tag{2.16d}$$

$$= \sum_{i=1}^{n} A_{1i}A_{ki}\sigma_{\Delta S}E[(\mathcal{N}(0,1))^2] \tag{2.16e}$$

$$= \mathbf{A}_1 \odot \mathbf{A}_k(\gamma_1\mathbf{S} + \gamma_2) \tag{2.16f}$$

The mean and variance of the approximated Gaussian distribution of a normalized Mueller matrix element, $E[M_k^n]$ and $\sigma^2_{M_k^n}$, are then obtained from a second-order Taylor expansion as in Eq. (2.17).

$$E[M_k^n] = \frac{\mu_{Q_N}}{\mu_{Q_D}} + \frac{\sigma^2_{Q_D}\cdot\mu_N}{\mu^3_{Q_D}} - \frac{cov(Q_N, Q_D)}{\sigma^2_{Q_D}} \tag{2.17a}$$

$$\sigma^2_{M_k^n} = \frac{\sigma^2_{Q_D}\cdot\mu^2_{Q_N}}{\mu^4_{Q_D}} + \frac{\sigma^2_{Q_N}}{\mu^2_{Q_D}} - \frac{2cov(Q_N, Q_D)\cdot\mu_{Q_N}}{\mu^3_{Q_D}} \tag{2.17b}$$

Error of the k_{th} normalized Mueller matrix element is the difference between M_k and the true value, which is a constant, and therefore is also a Gaussian distribution. The mean and variance of the error are μ_e and σ_e^2, and are given in Eq. (2.18).

$$\mu_e = \frac{\sigma^2_{Q_D}\cdot\mu_{Q_N}}{\mu^3_{Q_D}} - \frac{cov(Q_N, Q_D)}{\sigma^2_{Q_D}} \tag{2.18a}$$

$$\sigma_e^2 = \sigma_{M_k^n}^2 \tag{2.18b}$$

Finally, the mean absolute error of a normalized Mueller matrix is a folded normal distribution, and its expectation $E[|\Delta M_k^n|]$ is given by Eq. (2.19).

$$E[|\Delta M_k^n|] = \sigma_e \sqrt{\frac{2}{\pi}} e^{-(\mu_e^2/2\sigma_e^2)} - \mu_e \left(1 - 2h(\frac{\mu_e}{\sigma_e})\right) \tag{2.19}$$

where h is the normal cumulative distribution function.

2.3.2 Monte Carlo Simulations

In this subsection, in order to verify the statistical analysis in Subsection 2.3.1, Monte Carlo simulations are carried out. The expressions of induced normalized Mueller matrix error are verified, as well as the Gaussian distribution approximation of normalized Mueller matrix elements.

Monte Carlo simulations are carried out for different values of light intensity, sampling frequency, and noise magnitude. For each set of parameters, the experiment is simulated for 4000 times. In the simulations, the noise-free integrated intensities are simulated given the sample and the light source intensity. For each simulated noise-free integrated intensity,

the probabilistic distribution of the noisy integrated intensity is obtained according to Eq. (2.1), where the variance is a first-order function of the noise-free integrated intensity. By sampling from the distribution, the noisy integrated intensity is simulated. The simulations are performed for air and a grating sample. The simulations of both air and grating support the assumptions and results of the error propagation analysis. For brevity of this chapter, only the simulation results for a grating sample are presented. The results for air can be found in Appendix A. The SiO_2 on S_i grating sample has a pitch of 3 μm, a step height of 1 μm, and its theoretical Mueller matrix is computed through rigorous coupled-wave analysis (RCWA) at an incident wavelength of 384 nm, an incident angle of 55 and an azimuthal angle of 0°. Fig. 2-6 shows the SEM image of a grating sample.

The Gaussian approximation of normalized Mueller matrix elements is verified

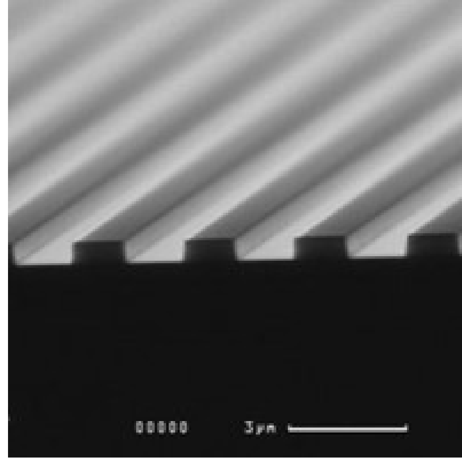

Figure 2-6: SEM image of the grating sample

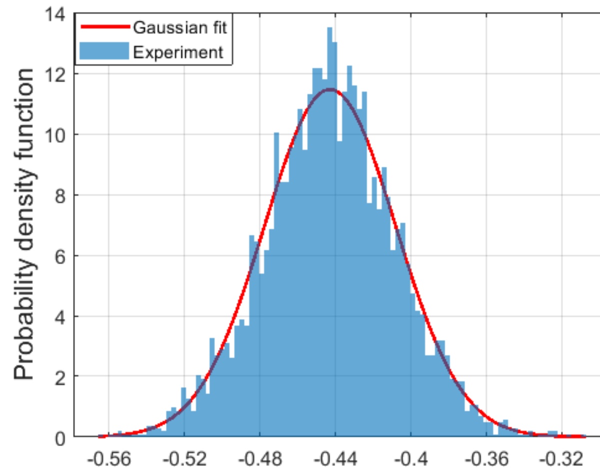

Figure 2-7: Histogram of normalized M_{33}^{n} values from simulations

through simulations. All simulations are conducted at fixed nominal normalized Mueller matrix elements values, obtained from simulation on the above-mentioned grating. Due to presence of Poisson-Gaussian noise, the values of each normalized Mueller matrix element form a distribution. For example, the fixed nominal value of M_{33}^{n} is -0.4437, and the simulated measurements form a distribution ranging from -0.5647 to -0.3072. Fig. 2-7 shows the histogram of normalized Mueller matrix elements measurements from simulations. The blue bars represent the probability density function from the simulations, and the red lines show the Gaussian fit. Fig. 2-8 shows the probability-probability plot (P-P plot) of each Mueller matrix element against a Gaussian distribution. The blue markers show the data from simulations, and the red line

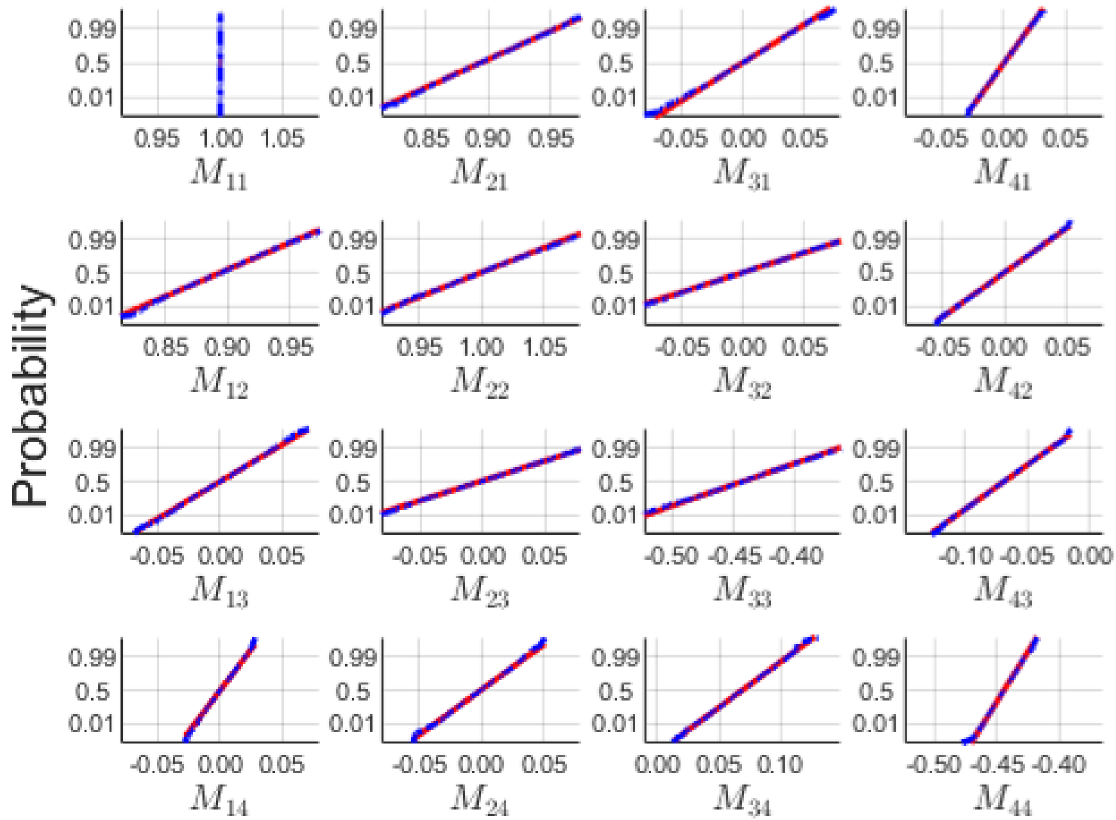

Figure 2-8: Normal probability plot of normalized Mueller matrix values from simulations

shows the normal distribution reference line. The match further validates the statement that each normalized MM element statistically form a Gaussian distribution. All normalized Mueller matrix elements present a valid Gaussian distribution, except for M_{11}, which is at a constant value of 1, due to the normalization with respect to M_{11}. The Gaussian approximation is also examined and verified for a smaller number of simulations. Fig. 2-9 is for 200 simulations. The Gaussian approximations pass a Lilliefors test with 2% significance level. There are some discrepancies at both ends of the lines, due to the small simulation set containing fewer samples from the low probability region. For the major part with a cumulative density function from 0.03 to 0.97, the two lines show good agreement, indicating the Gaussian approximation is valid.

The expression for induced Mueller matrix error is then verified. During each simulation, the mean absolute error of the Mueller matrix elements is calculated

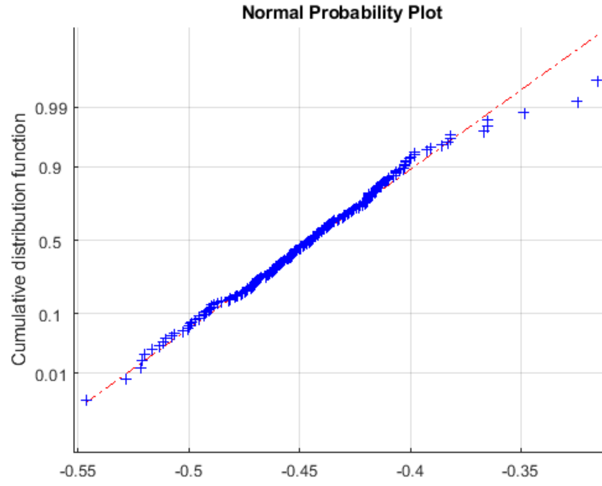

Figure 2-9: Normal plot of M_{33} using 200 simulations

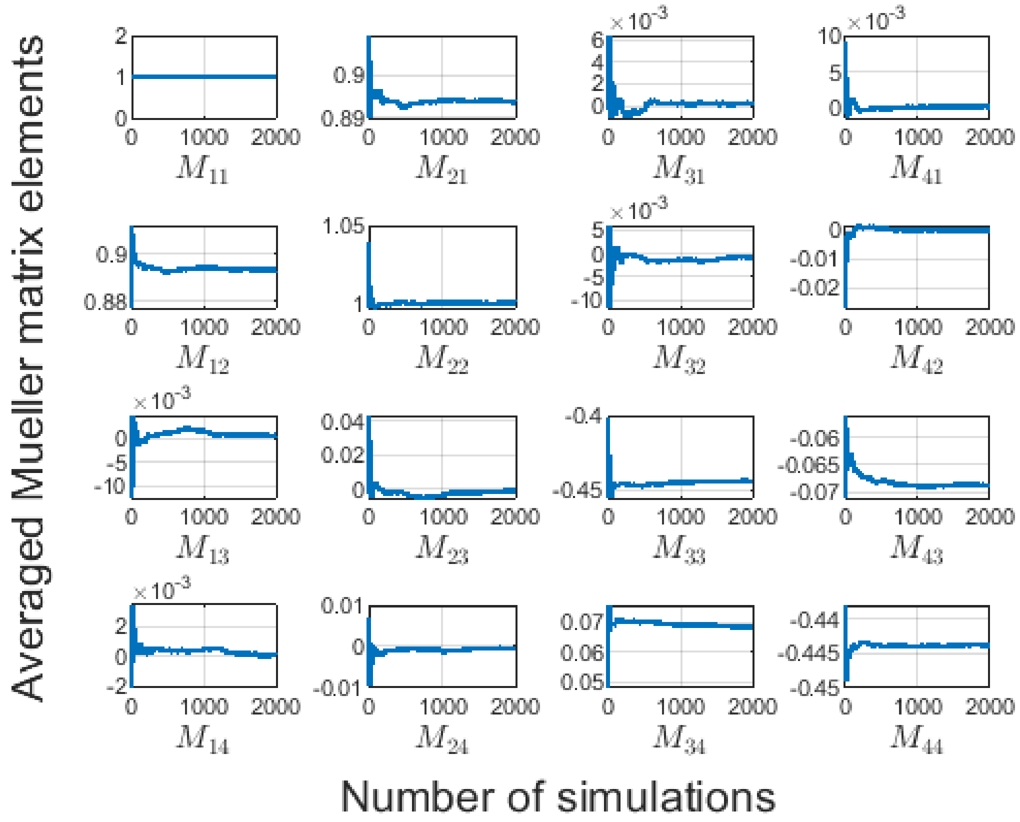

Figure 2-10: Averaged Mueller matrix elements converges

by averaging the absolute error over all elements. The mean absolute error is then averaged over all simulations. The effects of three parameters are studied, namely the first-order coefficient between an integrated intensity's variance and mean γ_1, the

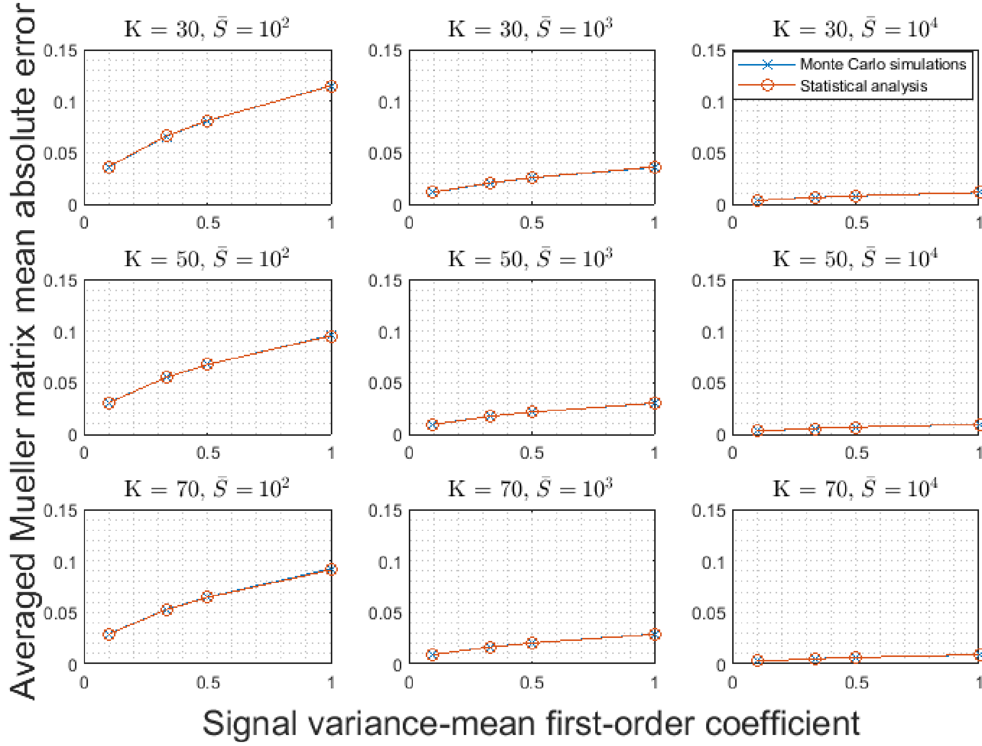

Figure 2-11: The induced measurement error increases with γ_1

sampling frequency, and the light intensity. Fig.2-10 shows the averaged Mueller matrix elements converge as the number of simulation increases. By inspecting the simulation result, the averaged Mueller matrix elements converge after around 500 simulations. The large number of simulations ensures convergence.

Fig.2-11 plots the averaged mean absolute error versus the first-order coefficient of signal variance to mean. Each subfigure represents a scenario with a different combination of light intensity and sampling frequency. The light intensity is increased from left to right, with the averaged light intensity $\bar{S}$ obtained by averaging the noise-free integrated intensities. The sampling frequency is increased from top to bottom. Two parameters, optical period and sampling frequency, can both affect the measurement accuracy, and the effects are dependent. By fixing one parameter, the effects of the other can be studied. In the simulations, the total time is selected as one optical period and fixed at 36s, and the sampling frequency is varied, and therefore the number of integrated intensities. In the subfigures' titles, K is the number of integrated intensities, and therefore, a larger K indicates a higher sampling rate. In

each subfigure, the mean absolute error is plotted with respect to the variance-mean first-order coefficient. The red curves are obtained from the probabilistic analysis, and the blue curves are obtained from the Monte Carlo simulations. The match indicates that the probabilistic analysis is verified by Monte Carlo simulation. In all scenarios, the error increases with increased γ_1 as expected. The error significantly decreases with increased light intensity. However, high intensity is not always feasible. For example, larger electrode gaps are required for the operation of higher power lamps, where the arc is susceptible to wandering [45]. Moreover, to be compatible with high-throughput requirements, the ellipsometer should operate with high speed, and therefore the integration time is shortened, and the integrated intensity magnitude is lowered. Lastly, the signal strength could be further lowered when the sample is absorbing. With respect to the effects of sampling frequency, the error slightly decreases with increasing sampling frequency. However, when operating at higher speed, only fewer integrated intensities can be obtained within one optical period with the same detector sampling capability.

2.4 Maximum Likelihood-Based Signal Demodulation for Noise Mitigation

In this section, a signal demodulation method is proposed to mitigate the Poisson-Gaussian noise induced errors in spectroscopic ellipsometry. In Subsection 2.4.1, the existing signal demodulation methods and noise-mitigation approaches are reviewed, and the technical gaps are identified. In Subsection 2.4.2, a demodulation method is proposed based on maximum likelihood method. The formalism and solution of the maximum likelihood signal demodulation method is derived. In Subsection 2.4.3, Monte Carlo simulations are

2.4.1 Review and Technical Gaps of Existing Demodulation and Noise-Mitigation Methods

Discrete Fourier Transform is the most recognized signal demodulation approach to rotating-component spectroscopic ellipsometry. Signal demodulation involves two steps: solving for the Fourier coefficients from the intensity signal, and in turn solving for the Mueller matrix from the Fourier coefficients. The most popular methods to solve for the Fourier coefficients are Discrete Fourier Transform (DFT) [45, 81–86] and Hadamard transform [44, 79], with the same underlying approach. The work in [79] unifies the two methods by establishing the relationship between the Fourier coefficients found by DFT and by Hadamard equations.

Many of the current demodulation methods, such as DFT, are not designed to tackle the signal-dependent noise. Poisson-Gaussian mixed noise exists in an optical system, and introduces errors on measurements. Gaussian noise represents the random and thermal noise. Poisson noise rises from the photon detection being a Poisson process, and its presence means the noise has strong correlation with the signal, and can potentially induce significant errors on the Mueller matrix and in turn the sample measurement. In addition, environmental vibrations and the setup's thermal expansion affect the light path and therefore generate signal-correlated noise. The error propagation analysis and error estimation for systematic random noise have been studied in [77], covering major error sources including setup errors, random errors in experiment, and reconstruction errors. In addition, the chapter accounts for other types of random noise than Poisson-Gaussian noise. Excellent works have been devoted to DFT and its advanced variants in optical system: Fourier domain peak phase (FDPP), Fast Peak Locating (FPL), and linear regression (LR) have been applied to estimate the optical path in spectral interferometry in the presence of additive Gaussian noise [87]. However, the above-mentioned methods do not account for the noise at the signal frequency or signal-noise correlation. To achieve Poisson denoising, an efficient way is transforming Poisson to white Gaussian distribution through Anscombe transform. However, signal in rotating-component ellipsometry changes in the temporal domain, and a different Gaussian distribution is generated after trans-

formation for each time point on the signal. The Fourier coefficients are then obtained from all signal points with varying Gaussian distribution properties. Therefore, the popular filters for white Gaussian noise such as DFT do not apply, because the noise distribution varies from each integrated intensity to another. Other works use redundant spatial or temporal information to achieve high imaging performance [88], but the methods do not apply to temporal varying ellipsometry. Similarly [89] uses redundant information, where the authors merge multiple frames to restore an image. In addition to signal post-processing, there are studies seeking to reduce the sensitivity to noise through setup optimization, and choosing specific polarization generation and analysis states in order to minimize the measurement variance when the system is subject to Gaussian and/or Poisson noise [90–94]. These works take an important step towards noise mitigation, but is only suitable for discrete measurement method. This chapter focuses on continuously-rotating measurement method, having its advantages of being compatible with high-speed and accurate measurement and imposing fewer motion control requirements.

2.4.2 Maximum Likelihood-Based Signal Demodulation

This subsection proposes an alternative maximum likelihood method to spectroscopic ellipsometry demodulation for improved accuracy. This subsection derives the maximum likelihood formalism for general rotating-component spectroscopic elllipsometry signal demodulation, as well as its solution as a system of nonlinear equations.

The maximum likelihood method described here solves for the Fourier coefficients, taking into account the probabilistic distribution of the signal. In the existing Hadamard method, to obtain the Fourier coefficients, linear regression minimizes the root mean squared error (RMSE) of the expected integrated intensities. Linear regression is based on the assumption of independent and identical noise distribution at each integrated intensity, which is violated in the case of the ellipsometry system. In practice, the ellipsometry system is subject to dominant Poisson-Gaussian noise, and therefore the noise distribution depends on the signal, and its distribution varies from each integrated intensity to another. Instead of minimizing the RMSE of the

expected integrated intensities, this chapter finds the Fourier coefficients by maximizing the probability of the signal as in Eq. (2.20), where $\hat{\boldsymbol{\theta}}$ is the expected unknown parameters, and S_k^n is the k_{th} element of $\mathbf{S}^n$.

$$\hat{\boldsymbol{\theta}} = \underset{\theta}{\text{argmax}}\ P(\{S_1^n, ..., S_k^n, ..., S_K^n\}|\boldsymbol{\theta}) \tag{2.20}$$

The probability of one integrated intensity taking on its observed value is in Eq. (2.21) when it follows a Gaussian distribution, where $P(S_k^n)$ is the probability of the k_{th} integrated intensity taking on the value of S_k^n, σ_k is the variance of the k_{th} integrated intensity. The probability of all observations assuming independence is shown in Eq. (2.22), where p is the likelihood function of the all integrated intensities taking on the observed values.

$$P(S_k^n) = \frac{1}{\sqrt{2\pi\sigma_k^2}}\text{exp}\left[\frac{-(S_k^n - S_k)^2}{2\sigma_k^2}\right] \tag{2.21}$$

$$p = P(\{S_1^n, ..., S_k^n, ..., S_K^n\}|\boldsymbol{\theta}) = \prod_{k=1}^{K} \frac{1}{\sqrt{2\pi\sigma_k^2}}\text{exp}\left[\frac{-(S_k^n - S_k)^2}{2\sigma_k^2}\right] \tag{2.22}$$

$$\mathrm{S_k} = \mathrm{\hat{S}_k} = \boldsymbol{\phi}_{\mathrm{k}}^{\mathrm{T}}\boldsymbol{\theta}\ \ \forall\, \mathrm{k} = 1, ..., \mathrm{K} \tag{2.23}$$

The clean signal is unknown, and the expected signal is used instead as in Eq. (2.24),where $\hat{S}_k$ is the expected k_{th} integrated intensity. Taking the natural log of the likelihood function yields the log-likelihood function in Eq. (2.25).

$$p = \prod_{k=1}^{K} \left(\frac{1}{2\pi\sigma_k^2}\right)^{\frac{1}{2}} \text{exp}\left[\frac{-(\hat{S}_k - S_k^n)^2}{2\sigma_k^2}\right] \tag{2.24}$$

$$\ln p = -\frac{K}{2}\ln(2\pi) - \frac{1}{2}\sum_{k=1}^{K} \ln \sigma_k^2 - \frac{1}{2}\sum_{k=1}^{K} \frac{1}{\sigma_k^2}\left(\boldsymbol{\phi}_k^T\boldsymbol{\theta} - S_k^n\right)^2 \tag{2.25}$$

Due to the monotonic nature of the natural log function, the objective is to maximize the log-likelihood function. After a sign flip, the formalism is equivalent to minimizing the objective function f, defined in Eq. (2.26a). The optimization problem is shown in Eq. (2.26). The constraint function $g_k(\boldsymbol{\theta})$ dictates that all the

predicted integrated intensities are non-negative as in Eq. (2.26c). The optimal condition is described by Eq. (2.26d) through (2.26h) from the Karush-Kuhn-Tucker (KKT) conditions, where $\mathbf{H}$ is the Hessian matrix, and μ_k is a slack variable.

$$f = \sum_{k=1}^{K} \ln \sigma_k^2 + \sum_{k=1}^{K} \frac{1}{\sigma_k^2} (\boldsymbol{\phi}_k^T \boldsymbol{\theta} - S_k^n)^2 \tag{2.26a}$$

$$\hat{\boldsymbol{\theta}} = \underset{\boldsymbol{\theta}}{\operatorname{argmin}} \, f \tag{2.26b}$$

$$g_k(\boldsymbol{\theta}) = -\boldsymbol{\phi}^T \boldsymbol{\theta} \leq 0 \;\; \forall \, k = 1, ..., K \tag{2.26c}$$

$$\frac{\partial f}{\partial \boldsymbol{\theta}} + \sum_{k=1}^{K} \frac{\partial g_k}{\partial \boldsymbol{\theta}} = \mathbf{0} \tag{2.26d}$$

$$\mathbf{H} = \frac{\partial^2 f}{\partial \boldsymbol{\theta}^2} \text{ is positive definite} \tag{2.26e}$$

$$\mu_k \geq 0 \;\; \forall \, k = 1, ..., k, ..., K \tag{2.26f}$$

$$\mu_k \boldsymbol{\phi}_k^T \boldsymbol{\theta} = 0 \;\; \forall \, k = 1, ..., k, ..., K \tag{2.26g}$$

$$-\boldsymbol{\phi}_k^T \boldsymbol{\theta} \leq 0 \;\; \forall \, k = 1, ..., k, ..., K \tag{2.26h}$$

After equation manipulation and simplification, Eq. (2.27) gives the solution to the optimization problem.

$$\sum_{k=1}^{K} \left[\frac{\gamma_1 + \boldsymbol{\phi}_k^T \boldsymbol{\theta}}{\gamma_1 \boldsymbol{\phi}_k^T \boldsymbol{\theta} + \gamma_2} + \frac{\gamma_2 \boldsymbol{\phi}_k^T \boldsymbol{\theta} - 2\gamma_2 S_k^n - \gamma_1 (S_k^n)^2}{(\gamma_1 \boldsymbol{\phi}_k^T \boldsymbol{\theta} + \gamma_2)^2} - \mu_k \right] \cdot \boldsymbol{\phi}_k = \mathbf{0} \tag{2.27a}$$

The Hessian matrix H is positive definite with elements H_{ij} given by

$$\begin{aligned} H_{ij} = \sum_{k=1}^{K} & \left[\frac{(\gamma_2 - \gamma_1^2) \phi_{ki} \phi_{kj}}{(\gamma_1 \boldsymbol{\phi}_k^T \boldsymbol{\theta} + \gamma_2)^2} \right. \\ & \left. + \frac{\gamma_1 \phi_{ki} \phi_{kj} (\gamma_1 \boldsymbol{\phi}_k^T \boldsymbol{\theta} - 2\gamma_2 \boldsymbol{\phi}_k^T \boldsymbol{\theta} + \gamma_2 + 4\gamma_2 S_k^n + 2\gamma_1 (S_k^n)^2)}{(\gamma_1 \boldsymbol{\phi}_k^T \boldsymbol{\theta} + \gamma_2)^3} \right] \end{aligned} \tag{2.27b}$$

$$\mu_k \geq 0 \;\; \forall \, k = 1, ..., k, ..., K \tag{2.27c}$$

$$\mu_k \boldsymbol{\phi}_k^T \boldsymbol{\theta} = 0 \;\; \forall \, k = 1, ..., k, ..., K \tag{2.27d}$$

$$-\boldsymbol{\phi}_k^T\boldsymbol{\theta} \leq 0 \ \ \forall\, k = 1, ..., k, ..., K \tag{2.27e}$$

$$\sum_{\mathrm{k=1}}^{\mathrm{K}}[\frac{\mathrm{c_1} + \boldsymbol{\phi}_{\mathrm{k}}^{\mathrm{T}}\boldsymbol{\theta}}{\mathrm{c_1}\boldsymbol{\phi}_{\mathrm{k}}^{\mathrm{T}}\boldsymbol{\theta} + \mathrm{c_2}} + \frac{\mathrm{c_2}\boldsymbol{\phi}_{\mathrm{k}}^{\mathrm{T}}\boldsymbol{\theta} - 2\mathrm{c_2}\mathrm{S_k} - \mathrm{c_1}\mathrm{S_k^2}}{(\mathrm{c_1}\boldsymbol{\phi}_{\mathrm{k}}^{\mathrm{T}}\boldsymbol{\theta} + \mathrm{c_2})^2}] \cdot \boldsymbol{\phi_k} = \mathbf{0} \tag{2.28a}$$

In practice when the signal is strong, all measurements are much greater than zero, and solving the unconstrained optimization will result in positive expected intensity. Therefore to save computation time, it is often sufficient to solve the unconstrained optimization as a first step, the solution of which is given in Eq. (2.29) and (2.27b). If the constraint is violated, then Eq. (2.27) should be solved.

$$\sum_{\mathrm{k=1}}^{\mathrm{K}}\left[\frac{\mathrm{c_1} + \boldsymbol{\phi}_{\mathrm{k}}^{\mathrm{T}}\boldsymbol{\theta}}{\mathrm{c_1}\boldsymbol{\phi}_{\mathrm{k}}^{\mathrm{T}}\boldsymbol{\theta} + \mathrm{c_2}} + \frac{\mathrm{c_2}\boldsymbol{\phi}_{\mathrm{k}}^{\mathrm{T}}\boldsymbol{\theta} - 2\mathrm{c_2}\mathrm{S_k} - \mathrm{c_1}\mathrm{S_k^2}}{(\mathrm{c_1}\boldsymbol{\phi}_{\mathrm{k}}^{\mathrm{T}}\boldsymbol{\theta} + \mathrm{c_2})^2}\right] \cdot \boldsymbol{\phi}_{\mathrm{k}} = \mathbf{0} \tag{2.29}$$

2.4.3 Monte Carlo Simulations

The improved performance of the proposed maximum likelihood method is demonstrated comparing to the existing DFT method. The Fourier coefficients are solved from the maximum likelihood formalism in *MATLAB* using *fsolve* function. The performance indicators are the Mueller matrix mean absolute error and the grating's reconstructed pitch. Table 2.1 tabulates the reduction in averaged Mueller matrix mean absolute error by using the maximum likelihood method compared to using DFT in Monte Carlo simulations. In all scenarios, the maximum likelihood method outperforms the linear regression method. Intuitively the maximum likelihood accounts for the varying variance and puts less confidence on the noisier integrated intensities.

The performance of the maximum likelihood method is then evaluated in terms of reconstructed grating pitch. During the reconstruction, the RCWA model is realized with different pitch values, and the closest match to the measurement is used to determine the sample pitch. In this chapter, the reconstruction has a resolution of 1 nm. Due to the presence of noise, the reconstructed pitch value shows a variation. Fig. 2-12a shows the histogram of the reconstructed pitch, where the blue and red bars are the results from the DFT and maximum likelihood method respectively. Fig. 2-12b presents another scenario where the light intensity is increased, and therefore

Table 2.1: Percent reduction in Mueller matrix mean absolute error

		$\gamma_1 = 0.1$	$\gamma_1 = 0.32$	$\gamma_1 = 0.5$	$\gamma_1 = 1$
K = 50	$\bar{S} = 10^2$	3.99%	3.15%	2.89%	2.46%
	$\bar{S} = 10^3$	3.47%	4.50%	3.19%	3.04%
	$\bar{S} = 10^4$	3.55%	3.33%	3.45%	2.93%
K = 70	$\bar{S} = 10^2$	3.59%	3.27%	2.46%	2.63%
	$\bar{S} = 10^3$	3.48%	3.25%	3.82%	3.28%
	$\bar{S} = 10^4$	3.77%	3.72%	3.03%	3.24%

the error is reduced. In both cases, the result from the maximum likelihood method is more centered at the pitch nominal value of 3 micrometer. The maximum likelihood method reduces the standard deviation from 3.9 nm to 3.8 nm in the first case, and from 2.3 nm to 2.1 nm in the second case. The result shows that the signal-correlated noise, specifically Poisson-Gaussian noise, can induce large errors on the reconstructed dimension, and the maximum likelihood method mitigates the effect to some extent.

2.5 Conclusion

Ellipsometry, as a metrology and inspection tool, plays an important role in many industries. However, the existence of Poisson-Gaussian mixed noise can significantly affect the measurement accuracy in ellipsometry.

This chapter then quantifies the induced measurement error by deriving the expression for the expected error of normalized Mueller matrix elements. The expression is verified through Monte Carlo simulations for various scenarios of light intensity, sampling frequency, and the first order coefficient of the integrated intensity's variance and mean. As expected, the error is reduced with increasing signal strength, increasing sampling frequency, and decreasing first order coefficient of the signal's variance to mean. The method can be also generalized to other types of random noises such as light source uncertainty using the same procedure. The distribution of the noise is first obtained, and the signal demodulation is carried out using maximum likelihood method. The error quantification serves as a guide in identifying the system's

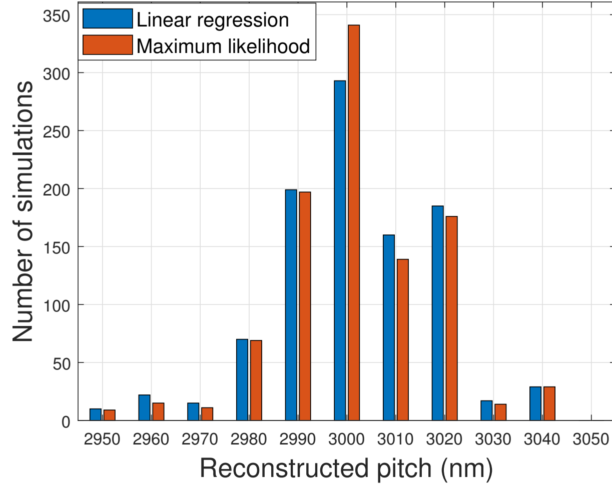

(a) Histogram at K = 50, $\bar{S} = 10^2$, $\gamma = 0.32$

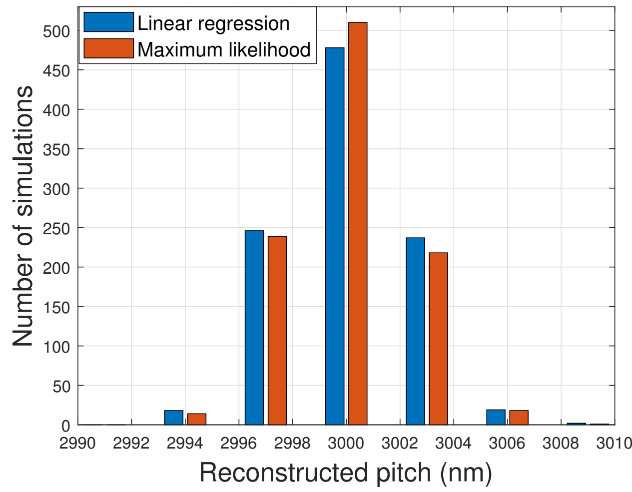

(b) Histogram at K = 50, $\bar{S} = 10^3$, $\gamma = 1$

Figure 2-12: Histogram of reconstructed pitch from a signal wavelength

optimal operating conditions and providing an evaluation to measurements. These are the major takeaways from this analysis. The Poisson-Gaussian noise originating from detection and environment is identified as a significant error source in Mueller matrix and in turn dimension measurement, and the Poisson-Gaussian noise induced error is quantified. In practice, this analysis gives the confidence interval for various experiment configuration on a spectroscopic ellipsometer, and can serve as a guidance for improving the system performance or making trade-offs in an industrial scenario. For example, higher light intensity is not always feasible: larger electrode gaps are required for the operation of higher power lamps, where the arc is susceptible to wan-

dering. In another example, pixel binning and averaging will reduce the first-order coefficient of variance to mean.

This chapter then proposes a maximum likelihood estimation approach to signal demodulation in spectroscopic ellipsometry, in order to mitigate the effects of Poisson-Gaussian noise. The method is compared to the existing DFT method, and shows improvements in terms of normalized Mueller matrix accuracy and dimension reconstruction performance. The method could be applied in many applications and provide more accurate measurements.

Chapter 3

Dimension Reconstruction

3.1 Introduction

This chapter focuses on the dimension reconstruction of ellipsometry. The experimental results are fitted to an optical model, and the closest match determines the dimensions of the sample. The fitting, together with the experimental measurement and optical modeling, determines the accuracy and precision of the reconstructed dimensions. In order to improve the precision of reconstructed dimensions, an algorithm is proposed to improve the reconstruction sensitivity. Higher weights are given to the more important configurations, where the measurement is sensitive to changes in dimensions. Lower weights are given to measurements at less critical configurations to reserve robustness. In this chapter, the reconstruction method and weight selection are studied.

For the rest of this chapter, the current reconstruction methods are reviewed in Section 3.2. In Section 3.3, the reconstruction problem is formulated, and the proposed algorithm is presented. Section 3.4 presents the experimental results to validate the proposed algorithm, and its improved precision is demonstrated. Conclusions are summarized in Section 3.5.

3.2 Review of Dimension Reconstruction and Technical Gaps

Dimension reconstruction is a critical step in ellipsometry measurement. In recent years, there has been work aiming to improve the accuracy of reconstruction.

The first problem that attracted attention is the limited dimension resolution during library search. When fitting the experimental result to a library generated by an optical model, the number of dimensions stored in the library is finite, and therefore the dimension resolution in the library is limited. To solve this problem, Chen et al. proposed two methods to go beyond the library's dimension resolution. Reference [95] proposed interpolating the fitting error to obtain values between the entries stored in the library. The work in [96] estimated the difference between the reconstructed dimensions and the library search solution using a linear model. Zhu et al. proposed two methods for higher reconstruction accuracy. In [97] and [98], Zhu et al. proposed a least trimmed squared estimator regression, where the authors use a squared error objective and iteratively remove the data that generate large fitting errors. In [99], [100] and [101], the authors extended the work in [96] by pre-storing Jacobian and introducing robust correction to the inverse problem.

The second problem in reconstruction is the capability of optical model to capture the properties of the experiment setup and/or the sample, which calls for work on the optical modeling. One factor that attracted attention in literature is the depolarizing effects. Reference [102] modeled depolarization from numerical aperture, finite bandwidth, and the residual layer thickness variation. The work in [103] also modeled and experimentally determined the depolarization from focus lens and finite spectral resolution. The Jones matrix quality factor was proposed in [104] to estimate depolarization. The proper modeling of the above-mentioned depolarizing effect will improve the modeling accuracy and in turn reduce the error carried over to dimension reconstruction.

There has also been work to improve the reconstruction speed. In [105], a dependence analysis was performed on the measured data to eliminate redundant data.

Specifically the authors used eigen-decomposition of the Jacobian matrix to identify the most independent measurements. The reconstruction was sped up due to the shrunken data set. A second approach is to use faster matching algorithm, for example [106] used SVM to match experimental and simulated profiles.

3.3 Improved Dimension Reconstruction Method

In this section, a method is proposed to improve the sensitivity of the dimension reconstruction. The dimension reconstruction is first formulated in Subsection 3.3.1, and the proposed method is described in Subsection 3.3.2.

3.3.1 Problem Formalism

The dimension reconstruction problem is formulated as follows. The sample is measured at different configurations, sequentially or simultaneously. The configurations include incident angle, wavelength, and the sample's azimuthal orientation. The quantity to characterize the sample is often referred to as "signature" in the literature. From these experiments, the measured signature, Mueller matrix elements in this case, can be obtained. The measured signature is fitted to simulated signatures generated by an optical model, and the closest match determines the reconstructed critical dimensions.

The goal of the reconstruction is to minimize the difference between measured and simulated signature. In Eq. (3.1), $\mathbf{x}$ is an n_x by 1 vector representing the dimensions, $\hat{\mathbf{x}}$ is the reconstructed dimension vector with the same dimension, Ω is the dimension's domain, $\mathbf{y}$ is the measured signature and is an m by 1 vector, $\mathbf{f}(\mathbf{x})$ is the simulated signature and is an m by 1 vector, $\mathbf{W}$ is the weight matrix and is an m by m diagonal matrix, and w_i is the matrix's ii_{th} element. The squared error is minimized.

$$\hat{\mathbf{x}} = \underset{\mathbf{x}\in\Omega}{\operatorname{argmin}}[\mathbf{y} - \mathbf{f}(\mathbf{x})]^T \mathbf{W} [\mathbf{y} - \mathbf{f}(\mathbf{x})] \tag{3.1}$$

While optimal reconstructed dimensions can always be obtained from the standard in Eq. (3.1), the range of the dimension should be given to account for the uncer-

tainties of measurement and simulation. Two criterion for determining the range are used in this chapter. Using the first criterion, a dimension is within the range if its fitting error is within the minimum fitting error multiplied by a constant, formulated as in Eq. (3.2), where J is a constant.

$$[\mathbf{y} - \mathbf{f}(\mathbf{x})]^T \mathbf{W} [\mathbf{y} - \mathbf{f}(\mathbf{x})] \leq J [\mathbf{y} - \mathbf{f}(\hat{\mathbf{x}})]^T \mathbf{W} [\mathbf{y} - \mathbf{f}(\hat{\mathbf{x}})] \tag{3.2}$$

Using the second criterion, a dimension is within the range if its fitting error is within 3σ from the minimum fitting error, and σ is the standard deviation of the fitting error originated only from random error. The criterion is described in Eq. (3.3).

$$[\mathbf{y} - \mathbf{f}(\mathbf{x})]^T \mathbf{W} [\mathbf{y} - \mathbf{f}(\mathbf{x})] \leq 3\sigma + [\mathbf{y} - \mathbf{f}(\hat{\mathbf{x}})]^T \mathbf{W} [\mathbf{y} - \mathbf{f}(\hat{\mathbf{x}})] \tag{3.3}$$

3.3.2 Improved Dimension Reconstruction Sensitivity

To improve the reconstruction sensitivity, different weights are given to the measurements from different configurations. The weights are chosen such that the reconstruction is sensitive to dimensions, and reserves information at less critical configurations to keep robustness.

The algorithm below outlines the implementation of the method. The dimensions are initialized to their nominal or estimated values. While the dimensions do not converge, in each step, the weights are selected to be proportional to the partial derivative of the simulated signature to the dimension at the current dimension values. Therefore, if the signature is sensitive to change in a dimension, it is given higher weight when that dimension is being reconstructed.

3.4 Experimental Verification of Improved Sensitivity

In this section, the experimental results are presented to validate the proposed reconstruction methods. Two types of samples are used. The first type is a S_iO_2 on S_i

Algorithm Improved reconstruction sensitivity with one parameter

$\hat{\mathbf{x}} \leftarrow \mathbf{x}_n$ ▷ Initialize the dimension to its nominal value

while $\hat{\mathbf{x}}$ does not converge **do**

  for j in $[1, 2, ..., n]$ **do**

    for i in $[1, 2, ..., m]$ **do**

      $w_i \propto \frac{\partial f_i(\mathbf{x})}{\partial \mathbf{x}_j}|_{\hat{x}_j}$ ▷ Update weight to improve sensitivity

    end for

    $\hat{x}_j = \underset{x_j \in \Omega_j}{\operatorname{argmin}}[\mathbf{y} - \mathbf{f}(\mathbf{x})]^T \mathbf{W} [\mathbf{y} - \mathbf{f}(\mathbf{x})]$ ▷ Update reconstructed dimension

  end for

end while

thin film standard. The thickness of the S_iO_2 layer is either about 310 nm for the first and the second sample, and about 1000 nm for the third sample. The dimension of interest is the thickness of the S_iO_2 layer. The second type of sample is a grating, usually used for AFM calibration. The S_iO_2 grating is formed on S_i layer. The dimensions to be measured are the step height and the ridge width. The grating is illustrated in Fig. 3-1. The experiments are performed on a in-house dual-rotating compensator ellipsometer, due to the device's advantages introduced in Chapter 1 and 2. Two experiment setup systems have been implemented, and the experimental results presented in this chapter were obtained only from the dual-rotating compensator ellipsometer. The Mueller matrix at different incident angles are measured sequentially. At each incident angle, the Mueller matrix at all wavelengths are measured simultaneously using a broadband light source. The experimental setup is described in detail in Chapter 5.

3.4.1 Reconstructed Dimension

Table 3.1 shows the measurement results. The first three samples are thin film standards. The thickness measured by the manufacturer and on the in-house setup are

Table 3.1: Reconstructed dimensions of thin film standards and a grating sample

Sample	Reference measurement	Experimental result Criterion 1	Experimental result Criterion 2
Thin film 1	Thickness: 302.5 ± 3.0 nm	Averaged: 302.5 ± 3.6 nm Weighted: 302.4 ± 1.2 nm	Averaged: 302.5 ± 0.6 nm Weighted: 302.4 ± 0.3 nm
Thin film 2	Thickness: 322.2 ± 3.0 nm	Averaged: 322.1 ± 3.8 nm Weighted: 322.0 ± 2.1 nm	Averaged: 322.1 ± 0.5 nm Weighted: 322.0 ± 0.3 nm
Thin film 3	Thickness: 1031.9 ± 3.1 nm	Averaged: 1028.0 ± 3.4 nm Weighted: 1028.1 ± 1.7 nm	Averaged: 1028.0 ± 0.6 nm Weighted: 1028.1 ± 0.2 nm
Grating	Height: 110 ± 10 nm AFM: 101.5 ± 1.0 nm	Averaged: 101.9 ± 7.1 nm Weighted: 101.8 ± 2.6 nm	Averaged: 101.9 ± 0.6 nm Weighted: 101.8 ± 0.3 nm
	Ridge width: no data AFM: 1617 ± 10.0 nm	Averaged: 1623.4 ± 170.4 nm Weighted: 1616.0 ± 85.0 nm	Averaged: 1623.4 ± 14.6 nm Weighted: 1616.0 ± 9.0 nm

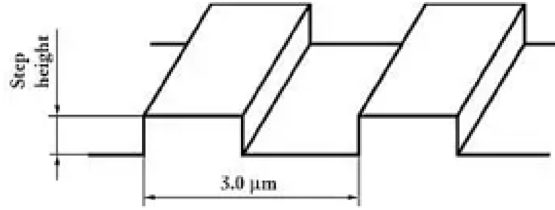

Figure 3-1: Illustration of grating

tabulated. The measurement and range is in the resolution of 0.1 nm. The fourth sample is a grating and is measured in our lab using an AFM and the ellipsometer. The ridge height given by the manufacturer is in the resolution of 1 nm, and measured with a resolution of 0.1 nm by the AFM and ellipsometer.

A range is given for all measurement to compensate for the uncertainties and errors involved in the measurement and optical modeling. The range for all ellipsometer measurements are calculated using the two criterion described in the last section. In all the scenarios, the range is smaller using the proposed method compared to fitting without weight adjustment. Therefore, reconstruction precision is improved.

3.4.2 Thin Film Measurement

Three S_iO_2 on S_i thin film samples are measured, each at an incident angle of 40°, 50°, and 60°.

The first thin film sample is mounted on a 3D-printed disk, shown in Fig. 3-2. The experimental and fitted Mueller matrix spectrum at an incident angle of 40° is presented in Fig. 3-3. Each subfigure shows the spectrum for one Mueller matrix element. The wavelength ranges from 450 nm to 1000 nm. The blue lines are experimental, and the red lines are best fitted spectra from simulation. A good fit is demonstrated. The fitted spectrum for sample 1 at incident angles of 50° and 60° can be found in Appendix A.

Similarly, sample 2 is mounted on 3D-printed disk. Sample 2 has a similar thickness with sample 1, and therefore leads to similar experiment result. For brevity, the result of sample 2 is presented in Appendix A, where a picture of the mounted sample is presented, as well as the experimental and fitted Mueller matrix spectrum of it at incident angles of 40°, 50°, and 60°.

Figure 3-2: Thin film sample 1

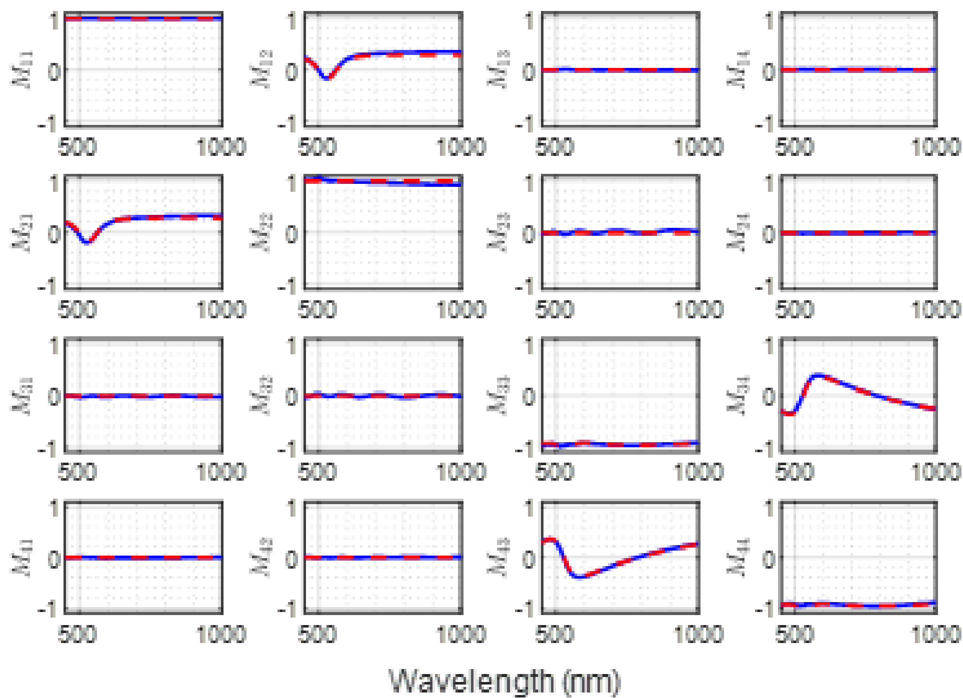

Figure 3-3: Experimental and fitted Mueller matrix spectrum of thin film sample 1 at 40° incident angle

The experimental and fitted Mueller matrix spectrum of the third sample is presented in Fig 3-4. Each subfigure shows the spectrum for one Mueller matrix element. The result is significantly different from that of sample 1 because the thickness is different. The wavelength ranges from 450 nm to 1000 nm. The blue lines are experimental, and the red lines are best fitted spectra from simulation. A good fit is demonstrated. The picture of mounted sample 3, and the fitted spectrum for sample 3 at incident angles of 50° and 60° can be found in Appendix A.

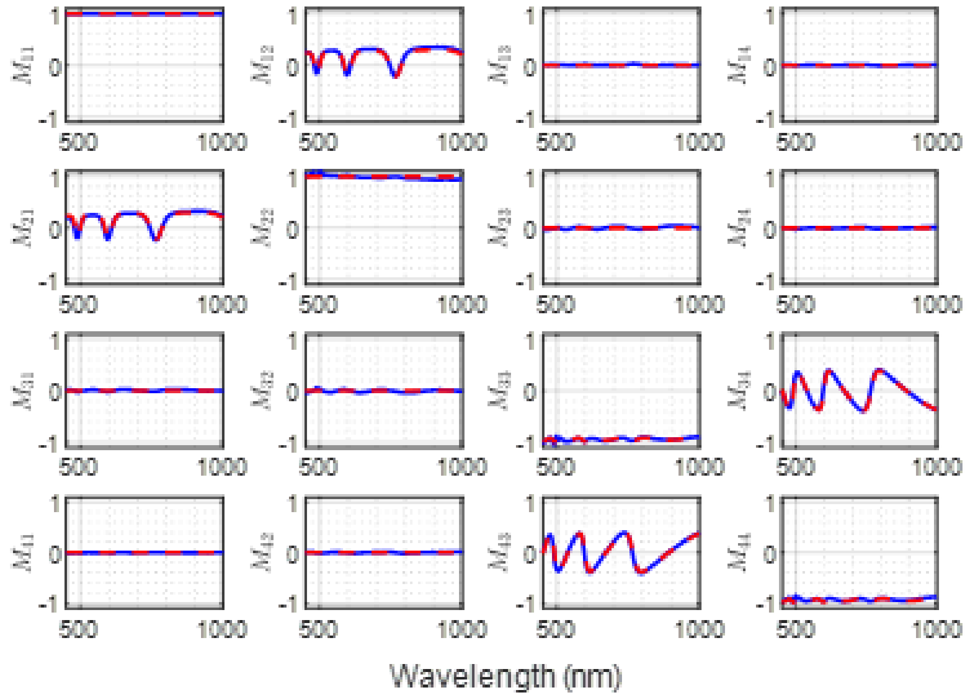

Figure 3-4: Experimental and fitted Mueller matrix spectrum of thin film sample 3 at 40° incident angle

3.4.3 Grating Measurement

A grating sample, *TGZ2* from *K-TEK Nanotechnology*, is measured. The sample is mounted on a metallic disk and then a 3D-printed disk, as shown in Fig. 3-5. Fig. 3-6 shows the AFM picture taken in our lab.

Fig. 3-7 is the experimental and fitted Mueller matrix spectrum of this grating at an incident angle of 50 degree. Each subfigure shows the spectrum for one Mueller matrix element. The wavelength ranges from 450 nm to 1000 nm. The blue lines are experimental, and the red lines are best fitted spectra from simulation. A good fit is demonstrated. The most noisy region falls under 450 nm to 550 nm, due to the light source having the lowest intensity in this range. The size of the grating sample is small, and light intensity reflected off the sample is small. Therefore, the noise-induced error is the largest in this region.

Figure 3-5: Mounted grating sample

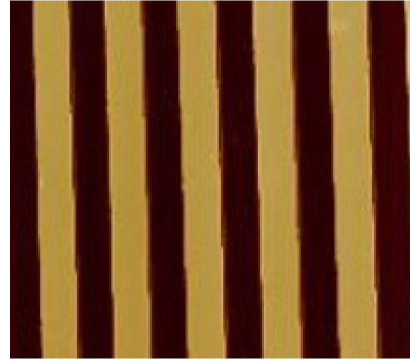

Figure 3-6: AFM image of grating sample

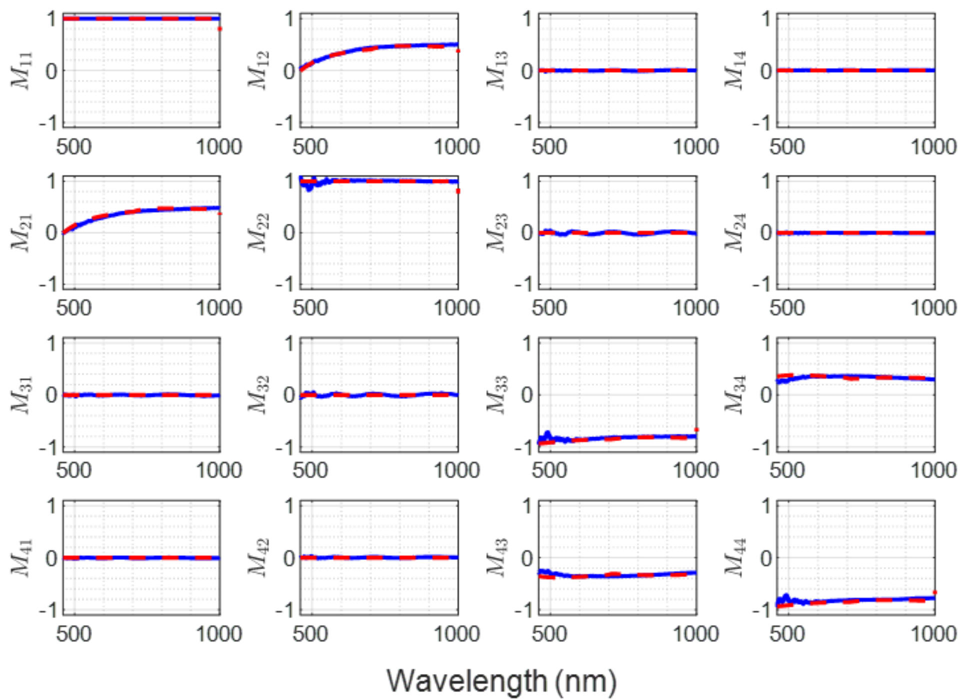

Figure 3-7: Experimental and fitted Mueller matrix spectrum *TGZ2* at 40° incident angle

3.5 Conclusion

This chapter focused on improving the dimension reconstruction precision. A method is proposed to improve the reconstruction sensitivity to changes in dimensions. High weights are given to the critical configurations. The weight selection and reconstruction method are formulated.

Two types of samples are experimentally measured to verify the improved precision resulted from the proposed method. The first type of samples are thin film

standards, and the thickness of which is reconstructed. The second type of sample is a grating sample, and the step height and ridge width of which are reconstructed. Two criterion are proposed to determine the range of reconstructed dimension. In all scenarios, the proposed reconstruction and weight selection demonstrated higher dimension reconstruction precision.

Chapter 4

Faraday Effect-Based Photometric Spectroscopic Ellipsometry

4.1 Introduction

Most popular commercial ellipsometers are based on moving polarizing components. However, the mechanical motion causes vibrations and inaccuracy, and limits the measurement speed. This chapter presents the design and demonstration of a Faraday effect-based photometric ellipsometer. The proposed design has several advantages. The elimination of mechanical motion enables high-speed and high-accuracy. In addition, the linear relationship between the applied current and the rotation of the polarization plane enables fast and easy demodulation. Lastly, the operating frequency of the Faraday rotator is controllable, making it compatible with most detection systems. The proposed instrument is useful in industrial applications where time resolution is critical, such as film growth and etching observations. This chapter presents the proposed ellipsometry's setup, data reduction, calibration procedures, and validation. The measurements on air and thin film is presented.

The rest of this chapter develops as follows. Section 4.2 motivates the Faraday effect-enabled photometric ellipsometry and provides a background. Section 4.3 presents the system design, calibration and data reduction of the proposed device. Section 4.4 shows the experimental results of calibration, sample measurements and

validates the design. Conclusions are summarized in 4.5.

4.2 Background and Motivation

There has been a lot of interest in eliminating mechanical motion in ellipsometry. The methods to remove moving components in ellipsometry for higher accuracy and speed include the following: electro-optics, photoelastic modulation (PEM), and magneto-optics. Among the methods, polarization manipulation through Faraday rotation is advantageous due to their high speed and high precision, high degree of current-polarization angle linearity, controllable modulation frequency, and capability of parallel wavelength scanning. The usage of Faraday-rotation enabled polarization manipulation is motivated in Subsection 4.2.1.

4.2.1 Motivation of Faraday Effect-Enabled Ellipsometry

There has been a lot of interest in eliminating mechanical motion in ellipsometry. Rotating-component ellipsometers have been the most popular commercial ellipsometers due to its simple implementation and parallel scanning over a wide spectral range [44, 45]. However, the rotation of polarizing components come with its disadvantages: mechanical vibrations cause measurement inaccuracy and position shift over time [107], and the speed of rotating-component ellipsometry is fundamentally limited by the mechanical rotation speed [45]. The methods to remove moving components in ellipsometry for higher accuracy and speed include the following: electro-optics, photoelastic modulation (PEM), and magneto-optics.

The use of electro-optical components in ellipsometry serves the purpose of eliminating mechanical rotating components. Liquid-crystal variable retarder (LCVR) was introduced in Mueller matrix ellipsometry in 2000 [69]. In addition to removing mechanical rotation and its associated errors, the utilization of LCVR also enables compact design [70]. However, electro-optical components do come with their disadvantages, and a major one is the nonlinear voltage-retardance behavior [108]. The nonlinear behavior has been demonstrated and measured in previous studies [107,109,110].

Due to the nonlinearity, most studies select a few voltage values to perform calibration and measurements. While the method enables a non-moving ellipsometer, it is potentially less robust, because measurements are only taken at discrete retardance values instead of a continuous range of retardance, which is potentially more sensitive to calibration errors and random noises. To counter this problem, some studies are devoted to the measurement of nonlinear voltage-retardance relationship and the usage of continuously variable voltage. Unfortunately, the effort did not report higher accuracy [107]. The second disadvantage is that LCVR exhibits retardance variations with ray incidence angle and ray position in the aperture, rendering challenges on calibration procedures and instrument design that are not previously found [70, 111]. The last disadvantage of wavelength dependency is not unique to ellipsometers using LCVR. Many earlier setups use only one or few wavelengths [69,71,72]. Later research started to use broadband light sources and proposed calibration methods [73, 74]. There have also been studies to optimize the ellipsometer setups using LCVR [75,76], and a Mueller matrix error lower than 0.5% has been reported for one wavelength on a polarizer sample in [73]. In summary, excellent works have advanced the application of electro-optical components in ellipsometry, but the voltage-retardance nonlinearity and sensitivity to alignment errors remains a challenge.

Photoelastic modulator (PEM)-based ellipsometry is a well-established ellipsometry configuration with advantages including no mechanically moving parts. In such an ellipsometer, a PEM is excited at its resonance frequency, ranging from 20 kHz to 100 kHz and typically 50 kHz. The modulator acts as an oscillating retarder to provide the necessary polarization manipulation together with other polarizing components. PEMs have several advantages including high speed, resistance to low-frequency noise, low operating power requirements, and greater numerical aperture. On the other hand, PEMs have limitations. First, the high modulation frequency poses challenges on the detection system. A charge-coupled device that is commonly used in 2-dimensional imaging cannot be used with PEM due to the readout time difference [45]. Second, a PEM-based ellipsometry cannot achieve parallel measurement at multiple wavelengths as a rotating-component ellipsometry for the same reason.

Therefore, the experiment time significantly increases when measurements at many spectral positions are required. Lastly, the time dependence of the light intensity from PEM is complex [45] and therefore so is the demodulation.

Magneto-optical components also enable ellipsometers with no moving parts, and therefore enables high-speed and high-precision modulation. The Faraday's effect is a phenomenon where a polarization plane is rotated in a material when a magnetic field is applied, and the rotation angle is proportional to the magnetic field projected on the light propagation direction. Faraday rotators have been applied in ellipsometry before. The first real-time spectroscopic ellipsometer took advantage of Faraday rotators [63]. The ellipsometer uses a "null" configuration, where the minimum irradiance is determined as a function of the azimuthal angle of the polarizer and the analyzer as well as the Faraday rotation angle, and the ellipsometric parameters are then determined [63–67]. While the configuration does achieve accurate measurement, it has drawbacks. First, the configuration does not allow parallel measurement at multiple wavelengths. One separate measurement has to be performed for each wavelength, and therefore the measurements are slowed when many spectral positions are required. Second, the measurement is susceptible to random noises in determining the nulling position, especially when the light source is weak. In contrast, later development of photometric ellipsometers with moving components can work faster [45] and with weak light sources [68].

This chapter presents the design and demonstration of a Faraday effect-based photometric ellipsometer. Using a Faraday rotator together with other stationary polarization components for polarization manipulation is potentially very advantageous. First of all, polarization states can be varied without moving components, enabling high speed and accuracy. Secondly, the modulation frequency is easily controlled using a Faraday rotator, and the system could be easily compatible with most signal processing and detecion systems. The last advantage is easy signal processing. Due to the high degree of linearity between the polarization rotation angle and the magnetic field, the light intensity can be easily demodulated. Negligible non-linearity exist due to magnetostriction. In contrast to previous application of Faraday rotator in

"null" ellipsometers, the proposed instrument operates in a photometric manner, and therefore is capable of parallel wavelength measurement. The instrument has many advantages. The instrumentation combines the strength of using Faraday rotator and photometric ellipsometer.

4.2.2 Background

Faraday's effect is a rotation of the polarization plane using a magnetic field along the direction of the light propagation, as illustrated in Fig. 4-1 [112]. The rotation angle of the polarization plane β is a function of the magnetic field and the medium properties, and is given by Eq. (4.1) [113]. The variables are: β is the rotation angle of the polarization plane, V is the Verdet constant, B is the magnetic flux density, and L_m is the length of the optically active medium. The Verdet constant of a material depends on the wavelength and the temperature, shown in Eq. (4.2) [114], where γ is an empirical constant, e and m_e are electron charge and mass, λ is the wavelength of the incident light, c is the speed of light in vacuum, and n is the refractive index.

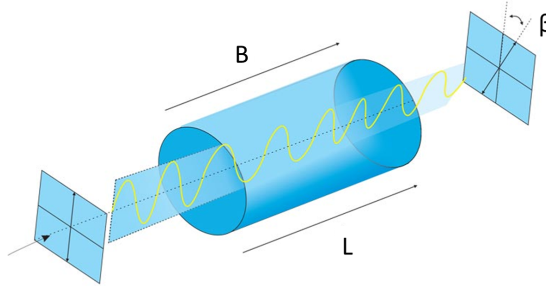

Figure 4-1: Illustration of Faraday rotation

$$\beta = V \int_0^{L_m} B(l)dl \tag{4.1}$$

$$V = \gamma \frac{-e\lambda}{2m_e c} \cdot \frac{dn}{d\lambda} \tag{4.2}$$

The Faraday-rotation only rotates the polarization plan and does not change the state of polarization for a linearly polarized light beam, meaning the exit light beam is still linearly polarized. The detailed derivation can be found in [115] and is outlined

below. A linearly polarized light can be decomposed into right-handed and left-handed polarized light with equal amplitude, as in Eq. (4.3), where E_{in} represents the electric field of the light beam before going through the Faraday rotator, z is the direction of light propagation, t is time, E_+ represents the electric field of the right-handed polarized light, E_- represents the electric field of the left-handed polarized light, ω_l is the light frequency, $\mathbf{u}$ and $\mathbf{v}$ are two orthogonal unit vectors and are both normal to the light's propagation direction. As in Eq. (4.3c), the superposition of the right-handed and left-handed circularly polarized light is indeed a linearly polarized light beam in the $\mathbf{u}$ direction.

$$E_{in}(z=0,t) = \frac{1}{\sqrt{2}}\Big[E_+(0,t) + E_-(0,t)\Big] \tag{4.3a}$$

$$= \frac{1}{2}\Big[(\mathbf{u}+i\mathbf{v})e^{-i\omega_l t} + (\mathbf{u}-i\mathbf{v})e^{-i\omega_l t}\Big] \tag{4.3b}$$

$$= \mathbf{u}e^{-i\omega_l t} \tag{4.3c}$$

The refractive index of the right-handed and left-handed polarized light are different in a Faraday medium. In Eq. (4.4), n_+ and n_- are the refractive index for right-handed and left-handed polarized light, $\bar{n}$ is the average of n_+ and n_-, Δn is the difference between n_+ and n_-,

$$n_+ = \bar{n} + \frac{\Delta n}{2} \tag{4.4a}$$

$$n_- = \bar{n} - \frac{\Delta n}{2} \tag{4.4b}$$

The electric field of the light beam, after going through Faraday rotator, is described by E_{out} in Eq. (4.5),

$$E_{out}(z=L,t) = \frac{1}{2}\left[(\mathbf{u}+i\mathbf{v})e^{\frac{i\omega_l n_+ L}{2c}}\, e^{-i\omega_l t} + (\mathbf{u}-i\mathbf{v})e^{\frac{i\omega_l n_- L}{2c}} e^{-i\omega_l t}\right] \tag{4.5a}$$

$$= \frac{1}{2}e^{-i\omega_l t}e^{\frac{i\omega_l L\bar{n}}{c}}\left[(\mathbf{u}+i\mathbf{v})e^{\frac{i\omega_l \Delta n L}{2c}} + (\mathbf{u}-i\mathbf{v})e^{-\frac{i\omega_l \Delta n L}{2c}}\right] \tag{4.5b}$$

Define the rotation angle in Eq. (4.6), and Eq. (4.7) is in turn obtained from Euler's

formula.

$$\Delta\theta = \frac{\omega_l \Delta n L}{2c} \tag{4.6}$$

$$e^{i\Delta\theta} = \cos\Delta\theta + i\sin\Delta\theta \tag{4.7a}$$

$$e^{-i\Delta\theta} = \cos\Delta\theta - i\sin\Delta\theta \tag{4.7b}$$

Eq. (4.5) can be rewritten and simplified in Eq. (4.8).

$$\begin{aligned} E_{out}(z = L, t) =& \frac{1}{2}\Big[(\mathbf{u} + i\mathbf{v})(\cos\Delta\theta + i\sin\Delta\theta) \\ &+ (\mathbf{u} - i\mathbf{v})(\cos\Delta\theta - i\sin\Delta\theta)\Big] e^{-i\omega_l t} e^{\frac{i\omega_l L\bar{n}}{c}} \end{aligned} \tag{4.8a}$$

$$\begin{aligned} =& \Big[\mathbf{u}\cos\Delta\theta - \mathbf{v}\sin\Delta\theta\Big] e^{-i\omega_l t} e^{\frac{i\omega_l L\bar{n}}{c}} \\ =& \mathbf{u}_n e^{-i\omega_l t} e^{\frac{i\omega_l L\bar{n}}{c}} \end{aligned} \tag{4.8b}$$

where

$$\mathbf{u}_n = \mathbf{u}\cos\Delta\theta - \mathbf{v}\sin\Delta\theta \tag{4.9}$$

Therefore, the light beam is still linearly polarized after going through Faraday rotator, and the plane of polarization is rotated by angle $\Delta\theta$.

4.3 Design and Analysis

In this section, the proposed Faraday effect-enabled photometric ellipsometer is described in detail. The design and instrumentation is presented in Subsection 4.3.1, the data reduction is presented in Subsection 4.3.2, and the calibration procedure is presented in Subsection 4.3.3.

4.3.1 System Design

In this subsection, the design of the Faraday rotator and the Faraday effect-enabled ellipsometer are presented.

Faraday Rotator Design

A Faraday rotator is designed to allow for controllable rotation angle of the polarization plane. It consists of three major components: a solenoid, Faraday-effect material, and the current controller. The current controller consists of a power source and an amplifier. Commercial products focus on Faraday isolators, where the rotation angle is fixed at 45°, and eliminate backward light [116–124]. In-house Faraday rotators with controllable rotation angle have been built for the purpose of material characterization and magnetic sensing [125–133].

In this work, SF-59 glass rod is chosen as the Faraday-effect material for its high Verdet constant and ease of procurement. Fig. 4-2 illustrates the design. The glass rod is placed in the holder, and inserted into the solenoid.

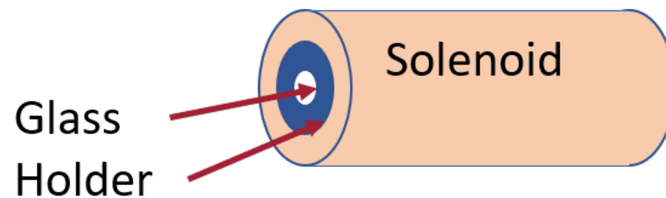

Figure 4-2: Illustration of the designed Faraday rotator

Table 4.1 lists four independent design parameters, and the eight design parameters that can be derived. The two major principle for the design are the capability of providing the necessary polarization rotation angle and the proper mechanical integration into the ellipsometer system. Table 4.2 lists the design criterion and the corresponding mathematical expressions.

Rotation angle of polarization plane - current linearity

The rotation angle of polarization plane as a function of the applied current is derived. Fig. 4-3 shows a single loop of the solenoid in free-space, where z is the longitudinal direction of the solenoid and also the light's propagation direction, and r is the loop's diameter. The coordinate's origin coincides with the center of the loop. A point T is arbitrarily selected along the z-axis, and an infinitesimal segment is arbitrarily selected on the loop, and the line connecting the point T to point Z on the infinitesimal

Table 4.1: Faraday rotator design parameters

Independent design parameters		Dependent design parameters	
L	length of holder	n_c	number of loops per layer
d_i	inner diameter of the holder	d_o	outer diameter of the holder
n_l	number of layers	d_w	diameter of electrical wire
G	electrical wire gauge	L_w	total length of electrical wire
		R	resistance per unit length
		L_m	material (glass rod) length
		W	wire weight
		w	wire weight per unit length

Table 4.2: Faraday rotator design criterion

Design criterion	Mathematical expression
The glass rod can be inserted into the holder	$d_i \geq 7.8mm$
The coil does not interfere with the cage system	$d_o \leq 54mm$ $d_o = d_i + 2n_l \cdot d_w$
Coils can be wrapped within the holder length	$n_c \cdot d_w \leq L$
Voltage across the coil	$V = L_w \cdot R \cdot I$ $L_w \approx \pi(d_i + d_o)/2 \cdot n_c \cdot n_l$
Polarization rotation angle Reasonable wire weight	$\beta = V \cdot B \cdot L_m$ $L_m = 99.1mm$ $V = 23rad/(Tm)$ $W = L_m * w$

segment is TZ. The angle between TZ and the z-axis is η, and the length of TZ is R_p. The magnetic field generated by the infinitesimal segment along the z-direction is given by dB_z in Eq. (4.10), where μ_0 is the vacuum permeability, I_c is the current through the solenoid, and dl is the length of the infinitesimal loop segment.

$$dB_z = \frac{\mu_0 \cdot I_c \cdot dl}{4\pi R_P^2} \cdot sin\theta \tag{4.10}$$

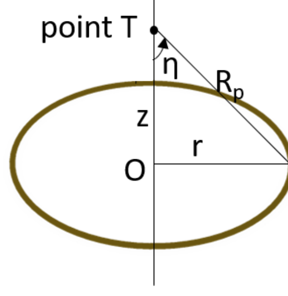

Figure 4-3: A single loop of the solenoid

The magnetic field generated by a single loop along the z-direction B_z is given by Eq. (4.11), where z is the distance from the center of the loop. Extending to a solenoid, the coordinate origin O coincide with the center of the coil in the middle.

$$B_z = \int dB_z \tag{4.11a}$$

$$= \frac{\mu_0 \cdot I_c \cdot 2\pi r}{4\pi R^2} * \frac{r}{R} \tag{4.11b}$$

$$= \frac{\mu_0 \cdot I_c \cdot r^2}{2(r^2 + z^2)^{3/2}} \tag{4.11c}$$

The magnetic field generated from multiple loops and multiple layers is then given in Eq. (4.12), where i_l is the index of the layers, i_c is the index of loops per layer, r_{i_l} is the radius of the loop in layer i_l, z_{i_c} is the longitudinal position of the loop i_c.

$$B(z) = I_c \sum_{i_l=1}^{n_l} \sum_{i_c=1}^{n_c} \left[\frac{\mu_o r_{i_l}^2}{2[r_{i_l}^2 + (z - z_{i_c})^2]^{\frac{3}{2}}} \right] \tag{4.12a}$$

$$r_{i_l} = \frac{d_i}{2} + d_w(i_l - \frac{1}{2}) \tag{4.12b}$$

$$z_{i_c} = \left(\frac{n_c + 1}{2} - i_c \right) d_w \tag{4.12c}$$

The rotation angle of polarization plane $\beta(\lambda)$ is given by Equation (4.13), where λ is the incident wavelength, $V(\lambda)$ is the Verdet constant as a function of the wavelength,

and D is a parameter of the solenoid and the material.

$$\beta(\lambda) = V(\lambda)\int_{-\frac{L_m}{2}}^{\frac{L_m}{2}} B(z)dz \tag{4.13a}$$

$$=V(\lambda)I_c\left[\sum_{i_l=1}^{n_l}\sum_{i_c=1}^{n_c}\left(\int_{-\frac{L_m}{2}}^{\frac{L_m}{2}} \frac{\mu_o r_i^2}{2[r_i^2+(z-z_i)^2]^{\frac{3}{2}}}dz\right)\right] \tag{4.13b}$$

$$=V(\lambda)I_cD \tag{4.13c}$$

Faraday effect on elliptically polarized light

This part addresses the Faraday effect on elliptically polarized light. An elliptically polarized light beam can be viewed as a combination of right-handed and left-handed polarized light with arbitrary amplitude, as in Eq. (4.14), where m_1 and m_2 are constants representing the amplitudes associated with the right-handed and left-handed polarized light.

$$E_{in}(z=0,t) = [m_1 \cdot E_+(0,t) + m_2 \cdot E_-(0,t)] \tag{4.14a}$$

$$= \frac{1}{\sqrt{2}}\left[(m_1\mathbf{u}+i\mathbf{v})e^{-i\omega t} + m_2(\mathbf{u}-i\mathbf{v})e^{-i\omega t}\right] \tag{4.14b}$$

$$= \frac{1}{\sqrt{2}}[(m_1+m_2)\mathbf{u}+(m_1-m_2)i\mathbf{v}]e^{-i\omega t} \tag{4.14c}$$

The light beam after going through a Faraday medium is described by E_{out} in Eq. (4.15).

$$E_{out}(z=L,t)$$
$$=\frac{1}{\sqrt{2}}\left[\ m_1(\mathbf{u}+i\mathbf{v})e^{\frac{i\omega\bar{n}L}{c}}e^{\frac{i\omega\Delta nL}{2c}} + m_2(\mathbf{u}-i\mathbf{v})e^{\frac{i\omega\bar{n}L}{c}}e^{-\frac{i\omega\Delta nL}{2c}}\ \right]e^{-i\omega t} \tag{4.15a}$$

$$= \frac{1}{\sqrt{2}}[m_1(\mathbf{u}+i\mathbf{v})e^{\frac{i\omega\Delta nL}{2c}} + m_2(\mathbf{u}-i\mathbf{v})e^{-\frac{i\omega\Delta nL}{2c}}]e^{\frac{i\omega\bar{n}L}{c}}e^{-i\omega_l t} \tag{4.15b}$$

Part of Eq. (4.15) can be rewritten and simplified as in Eq. (4.16).

$$m_1(\mathbf{u}+i\mathbf{v})e^{\frac{i\omega\Delta nL}{2c}}+m_2(\mathbf{u}-i\mathbf{v})e^{-\frac{i\omega\Delta nL}{2c}} \tag{4.16a}$$

$$=m_1(\mathbf{u}+i\mathbf{v})(\cos\Delta\theta+i\sin\Delta\theta)+m_2(\mathbf{u}-i\mathbf{v})(\cos\Delta\theta-i\sin\Delta\theta) \tag{4.16b}$$

$$=(m_1+m_2)(\cos\Delta\theta\mathbf{u}-\sin\Delta\theta\mathbf{v})+(m_1-m_2)i(\sin\Delta\theta\mathbf{u}+\cos\Delta\theta\mathbf{v}) \tag{4.16c}$$

The new unit vectors are defined as the following.

$$\mathbf{u}_n=\cos\Delta\theta\mathbf{u}-\sin\Delta\theta\mathbf{v} \tag{4.17a}$$

$$\mathbf{v}_n=\sin\Delta\theta\mathbf{u}+\cos\Delta\theta\mathbf{v} \tag{4.17b}$$

Rewriting the exit beam gives

$$E_{out}(z=L,t)=\frac{1}{\sqrt{2}}e^{\frac{i\omega\bar{n}L}{c}}e^{-i\omega_l t}[(m_1+m_2)\mathbf{u}_n+(m_1-m_2)\mathbf{v}_n] \tag{4.18}$$

Therefore, similar to a linearly polarized light beam, an elliptically polarized light beam maintains its polarization state after going through Faraday medium, and only experience a rotation.

Faraday Effect-Enabled Ellipsometer Design

The proposed setup consists of an incident light arm, a sample stage, and a reflective light arm. The incident arm is mounted with an optical fiber connected to a broadband light source, an iris, a collimator, a polarizer (P), and a Faraday rotator (FR_1). The reflective arm is mounted with a Faraday rotator (FR_2), an analyzer (A), and a fiber connected to a spectrometer. The setup with its major components are illustrated in Figure 4-4.

4.3.2 Data Reduction

The first Faraday rotator rotates the polarization plane of the light beam exiting the polarizer before it incidents on the sample, and the second Faraday rotator is used to cause rotation of polarization on the light beam reflected off the sample. During

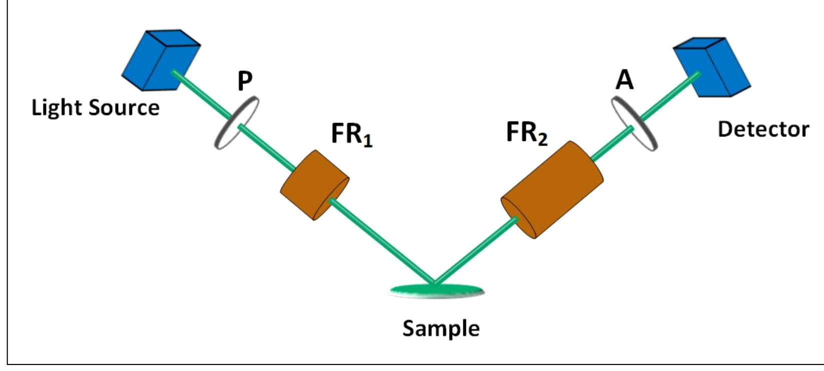

Figure 4-4: Setup illustration

each measurement, the current to the first Faraday rotator is kept constant, while the rotation angle of the second Faraday rotator is varied linearly with time. The equation of the light path is given by Equation (4.19), where $\mathbf{S}_o$ is the exit Stokes vector; $\mathbf{M}_A$ is the Mueller matrix of the analyzer A_s is the azimuthal offset of the analyzer; $\mathbf{R}(A_s)$ is the rotation matrix associated with A_s; $\mathbf{M}_{FR_2}$ is the Mueller matrix of the second Faraday rotator; $\mathbf{M}_S$ is the Mueller matrix of the sample; $\mathbf{M}_{FR_1}$ is the Mueller matrix of the first Faraday rotator; P_s is the azimuthal offset of the polarizer $\mathbf{R}(-P_s)$ is the rotation matrix associated with $-P_s$; $\mathbf{M}_P$ is the Mueller matrix of the polarizer; $\mathbf{S}_i$ is the Stokes vector of the incident light. The resulting time-varying light intensity curve is harmonic as in Equation (4.20a). In the designed ellipsometer, the exit light is measured by a CCD spectrometer, and the measurement is a series of integrated intensity. The Fourier coefficient can be solved through Hadamard transform as in [80] or the maximum likelihood method in Chapter 2. For an isotropic non-depolarizing sample, there are two ellipsometric parameters to fully characterize the sample.

$$\mathbf{S}_o = \mathbf{M}_A \cdot \mathbf{R}(A_s) \cdot \mathbf{M}_{FR_2} \cdot \mathbf{M}_S \cdot \mathbf{M}_{FR_1} \cdot \mathbf{R}(-P_s) \cdot \mathbf{M}_P \cdot \mathbf{S}_i \tag{4.19}$$

$$I = I_o \left[1 + \alpha_2' \cos(2VvDt) + \beta_2' \sin(2VvDt)\right] \tag{4.20a}$$

$$v = \frac{dI_c}{dt} \tag{4.20b}$$

$$\alpha_2 = \alpha_2' \cos(2A_s) + \beta_2' \sin(2A_s) \tag{4.21a}$$

$$\beta_2 = -\alpha_2' \sin(2A_s) + \beta_2' \cos(2A_s) \tag{4.21b}$$

The phase-corrected Fourier coefficients by the analyzer's azimuthal offset is given by Eq. (4.21) [134, eq. (4.60)]. The ellipsometric parameters ψ and Δ can be solved from the Fourier coefficients and the DC terms, as in Equations (4.22) [134, eq. (4.24)], where P_a is the polarizer's azimutha angle.

$$\tan\psi = \sqrt{\frac{1+\alpha_2}{1-\alpha_2}}|\tan P_a| \tag{4.22a}$$

$$\cos\Delta = \frac{\beta_2}{\sqrt{1-\alpha_2^2}} \tag{4.22b}$$

For an isotropic sample, the normalized Mueller matrix is given by Equation (4.23), where M is the normalized Mueller matrix. The normalized Mueller matrix elements can also be written out. Two elements are given in Equation (4.23) [45].

$$M = \begin{bmatrix} 1 & -\cos(2\psi) & 0 & 0 \\ -\cos(2\psi) & 1 & 0 & 0 \\ 0 & 0 & \sin(2\psi)\cos(\Delta) & \sin(2\psi)\sin(\Delta) \\ 0 & 0 & -\sin(2\psi)\cos(\Delta) & \sin(2\psi)\sin(\Delta) \end{bmatrix} \tag{4.23}$$

$$M_{12} = \frac{\alpha_2 - \cos(2P_s)}{1 - \alpha_2\cos(2P_s)} \tag{4.24a}$$

$$M_{33} = \frac{\beta_2 \sin(2P_s)}{1 - \alpha_2\cos(2P_s)} \tag{4.24b}$$

4.3.3 System Calibration

The calibration consists of the Verdet constant calibration, analyzer azimuthal angle calibration, and polarizer azimuthal angle calibration.

The Verdet constant calibration can be completed before mounted on the setup. The Malus law establishes the relationship between the intensity of light passing through a polarizer and an analyzer and the angle between their transmission axes, as in Equation (4.25), where I_l is the light intensity transmitted through the analyzer,

I_{lo} is the intensity of linearly polarized light incident on the analyzer, and ϕ is the angle between the polarizer and analyzer transmission axes. The transmission light arm consists of an optical fiber connect to a broadband light source, an iris, a collimator, a polarizer, the Faraday rotator to be calibrated, an analyzer, followed by an optical fiber connected to a spectrometer. The analyzer is first mounted such that its transmission axis is parallel with that of the polarizer. The solenoid is excited with currents at different positive and negative magnitudes, and the maximum transmitted intensity I_{lo} can be obtained. The Verdet constant is then estimated from the slope as in Eq. (4.26a). For maximum sensitivity of determining Verdet constant, the analyzer can be rotated such that its transmission axis is roughly 45 deg with respect to the polarizer's transmission axis. Nonlinear behavior might occur for reasons including heating. The degree of linearity needs to be studied and verified during the calibration process.

$$I_l = I_{lo} \cdot \cos^2(\phi + \beta) \tag{4.25}$$

$$\begin{aligned} V(\lambda) &= \frac{1}{I_c P}\beta && (4.26a) \\ &= \frac{1}{I_c P}\left(\cos^{-1}\sqrt{\frac{I(\lambda)}{I_o}} - \phi\right) && (4.26b) \end{aligned}$$

The analyzer azimuthal angle is calibrated on the ellipsometer in the transmission mode. The current to the second solenoid is varied, until a maximum or minimum measured intensity is observed or fitted. The angle offset between the polarizer and analyzer transmission axes, $P_s - A_s$, can be determined.

The azimuthal angle of the polarizer relative to the sample is calibrated using the residual function method described in [45]. On the proposed setup, current is supplied to the first Faraday rotator, and the second Faraday rotator is excited with linearly varied current. The polarizer azimuthal offset is determined by fitting and minimizing the residual function [45, Eq. (5.82)].

4.4 Experimental Calibration and Measurement

In this section, the experimental calibration of the Verdet constant are presented in Subsection 4.4.1, followed by the measurement results of air and a Si on SiO_2 thin film sample in Subsection 4.4.2.

4.4.1 Verdet Constant Calibration

The Verdet constant calibration was conducted for the Faraday rotators used on the ellipsometer.

The calibration setup consists of the light path and the current signal generation electronics. Figure 4-5a shows the light arm. The current generation is shown in Figure 4-5b. The signal generation user interface is implemented in LabVIEW, where the amplitude, frequency, and offset of the signal can be set. The real-time signal is then generated by MyRIO and amplified by the power amplifier. MyRIO also sends a trigger signal to the spectrometer, in order to synchronize the polarization modulation by the Faraday rotator and the light intensity measurement by the spectrometer. During the calibration, the solenoid is excited with a constant current, and consecutive light intensity measurements are taken and averaged. The light intensity measurement is repeated for different current values. The calibration is performed simultaneously over the spectral range from 450 nm to 950 nm

The calibration lines are presented in Figure 4-6. Four equally spaced wavelengths are arbitrarily selected for presentation, such that they span the spectral range. The rotation angle of the polarization plane is plotted versus the current applied to the solenoid. The experimental result is plotted in blue markers, and the best-fit lines are plotted in red. Nonlinear rotation angle and current relationship exists in the system due to solenoid heating and magnetostriction. To determine the degree of nonlinearity, the coefficient of determination R^2 is calculated. The minimum value of R^2 is above 0.99 over all spectral range, verifying a high degree of linearity between the applied current and the rotation angle. Therefore ignoring the nonlinearity is acceptable, and future research can further address the issue.

The Verdet constant versus the wavelength is plotted in Figure 4-7. The blue

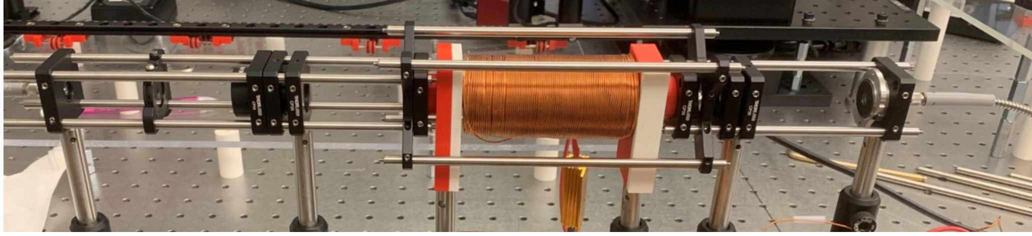

(a) Verdet constant calibration setup - optical arm

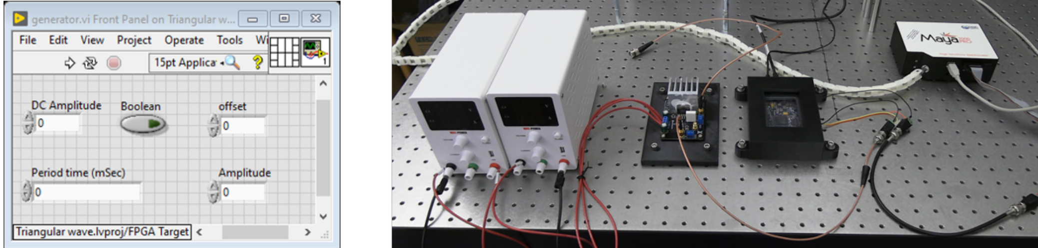

(b) Verdet constant calibration setup - circuit

Figure 4-5: Verdet constant calibration setup

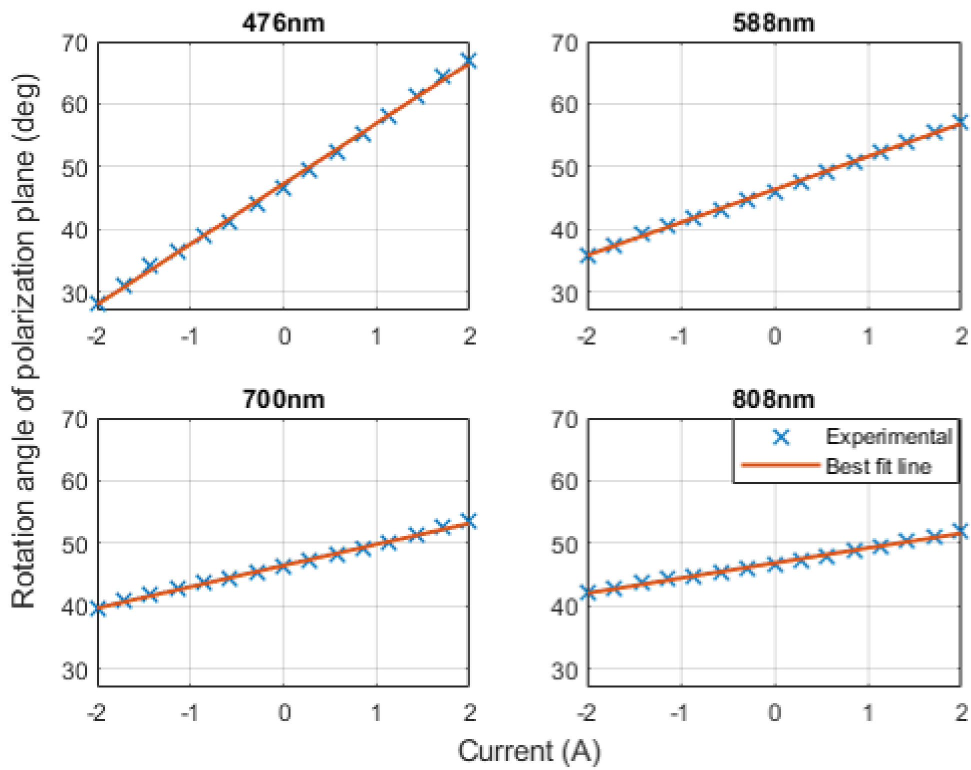

Figure 4-6: Calibration curve at four wavelengths

markers represent the experimental calibration, the red line shows the result from [135], and the green dot shows the result from [136]. Overall, the experiment is in good agreement with the literature. The difference can be due to design and

implementation discrepancies and different experiment conditions. There are several causes for design and implementation discrepancies: the length of the glass rod is not exactly as its nominal value; the longitudinal centers of the glass rod and the solenoid are not precisely aligned; the number of solenoid loops are not exactly the same as the design due to limited fabrication capability. The different environment temperature could also cause different Verdet constant.

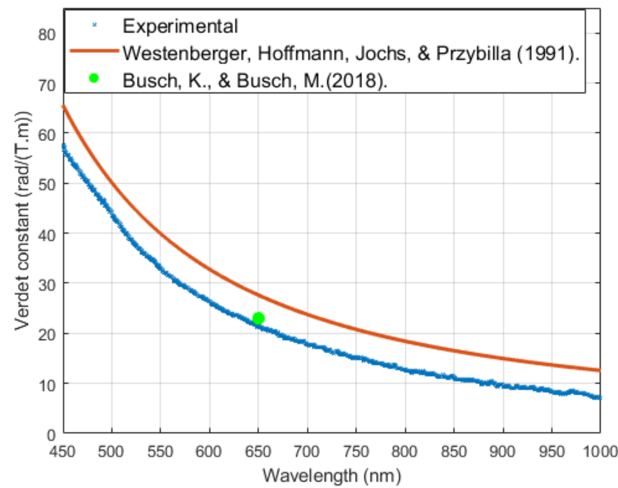

Figure 4-7: Wavelength dependency of Verdet constant

A sawtooth signal was also sent to the Faraday rotator for the purpose of calibration as well as confirming the signal following performance. In Fig. 4-8, the red curve is input sawtooth current to the solenoid, and the blue curve is the rotational angle. The rotation angle is calculated from measured light intensity. As analyzed in Chapter 2, the measured light intensity involves noise, and as a result, the measurement of rotation angle is noisy.

4.4.2 Sample Measurement

Measurements are performed on air and a Si on SiO_2 thin film sample.

The calibrated Faraday rotators are incorporated into the ellipsometer setup, shown in Figure 4-9. The setup consists of an incident arm, a 6-degree of freedom (DOF) sample stage, and a reflective arm. The incident arm is mounted with a fiber connected to the broadband light source, an iris, a collimator, a polarizer, and

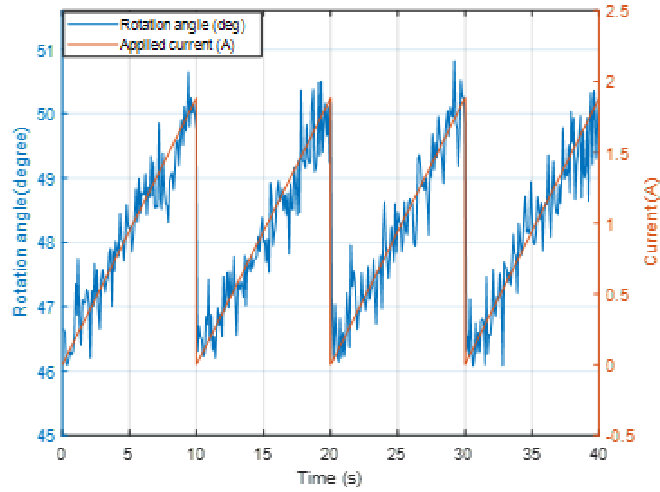

Figure 4-8: Signal following performance

a Faraday rotator. The reflective arm is mounted with a larger Faraday rotator, an analyzer, and an optical fiber connected to the spectrometer. The two optical arms are mounted on coaxial rotary stages with full rotation capability to allow for easy incident angle adjustment.

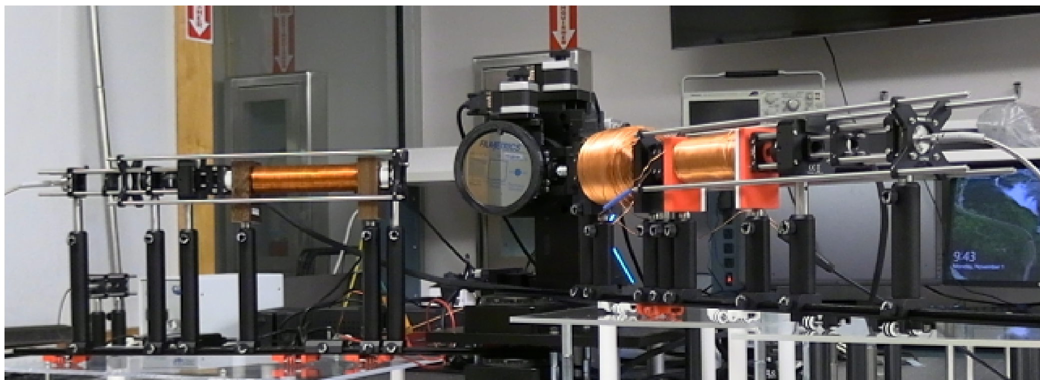

Figure 4-9: Ellipsometer setup incorporating Faraday rotators

Measurement of air is taken with the setup in transmission mode. The spectra of two normalized Mueller matrix elements M_{12} and M_{33} are plotted in Figure 4-10. The Mueller matrix of air should be an identity matrix. The blue lines represent experimental results, and the red lines show the theoretical values. In theory, any normalized Mueller matrix elements should fall in [-1,1]. Here the ranges of the y-axes are adjusted for easy visualization, and do not represent any physical significance. The good match between the experimental and theoretical spectra indicates a well-

functioning ellipsometer. The maximum discrepancy occurs in the spectral region from 450 nm to 550 nm, because the intensity from the light source is low in this region and the Poisson-Gaussian noise induced error is large [137].

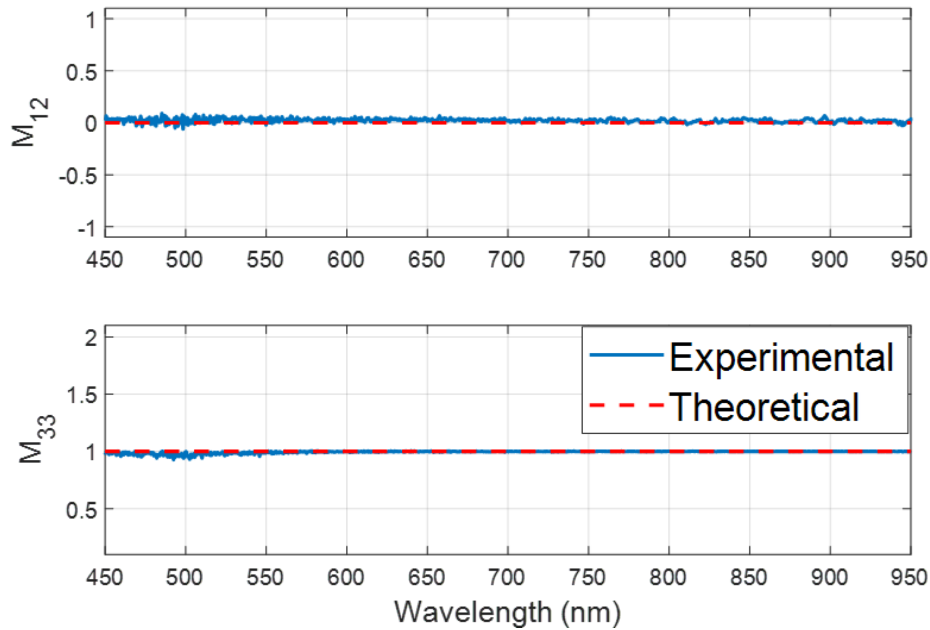

Figure 4-10: Ellipsometric parameters' spectra of air

The measurement result of the Si on SiO_2 thin film sample is presented in Figure 4-11. The measurement is taken at an incident angle of 50°. The blue lines represent the experimental spectra, which are fitted to a rigorous coupled-wave analysis (RCWA) model. The closest match is plotted in red lines. The measured thickness is 322.60 nm, and the value given by the manufacturer is 322.20 nm. The discrepancy is well within an acceptable range.

4.5 Conclusion

This chapter proposes and demonstrates a Faraday rotation-enabled photometric ellipsometer, operating in a parallel wavelength scanning mode. The proposed instrumentation has several advantages. The absence of moving components enables fast and precise control. In addition, the current-rotation angle linearity enables fast and easy signal demodulation. The two advantages improve speed and accuracy in

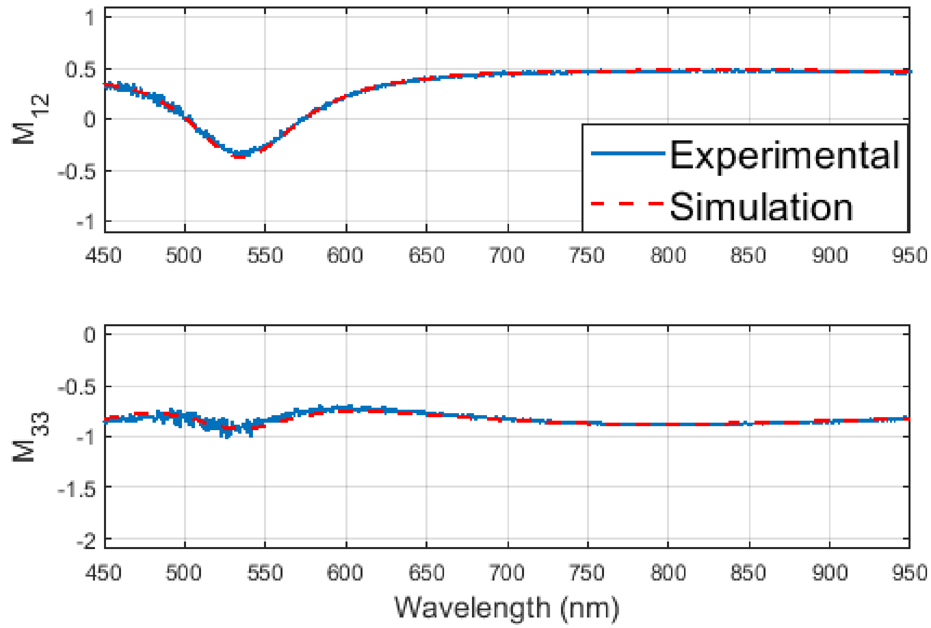

Figure 4-11: Ellipsometric parameters' spectra of thin film

ellipsometer measurement. The third major advantage is the controllable modulation frequency. It can interface with most detection system. In this chapter, the setup, data reduction, and calibration procedures are described, and the experimental measurement on air and thin film is presented. The measurement on air shows good agreement with theory, and the instrument measures a thickness of 332.6nm, while that provided by the manufacturer is 322.2 nm. This advancement can enable higher-speed measurement and better catch real-time processes. One configuration is designed and demonstrated in this chapter, capable of measuring the ellipsometric parameters. More complicated configurations incorporating Faraday rotators can be designed in the future to measure all Mueller matrix elements.

Chapter 5

Experiment Setup and Procedures

5.1 Introduction

This chapter describes the experiment setup and procedures. The ellipsometer setup, the integration of Faraday rotator, and the experiment procedures are introduced in each section. Two ellipsometer systems have been implemented. The first system is a dual-rotating compensator ellipsometer, with two rotating compensators. The second system is a Faraday-rotator enabled photometric ellipsometer, which does not involve moving components. The rest of this chapter develops as follows. Section 5.2 describes the in-house ellipsometer setup in detail, Section 5.3 describes the integration of Faraday rotators into the ellipsometer, and Section 5.4 describes the experiment procedures including sample mounting, motion control, and data collection.

5.2 Ellipsometer Setup

This section describes the in-house dual-rotating compensator ellipsometer setup. As an overview, Fig. 5-1 displays the SolidWorks design of the dual-rotating compensator ellipsometer setup. The setup mostly consists of an incident optical arm connected to a light source (1), a 6-DOF sample stage (2), and a reflective arm connected to a spectrometer (3). The three parts are connected through an elevated platform (4). The implemented setup is presented in Fig. 5-2 in its reflection mode. Fig. 5-1 and

5-2 show the complete setup. Zooming in on the key components, Fig. 5-3 is a zoomed view on the key components.

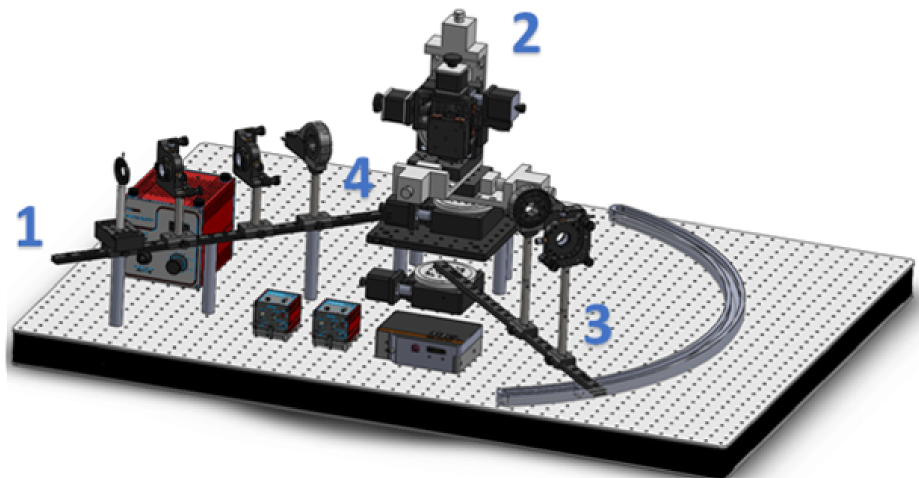

Figure 5-1: In-house dual-rotating compensator ellipsometer

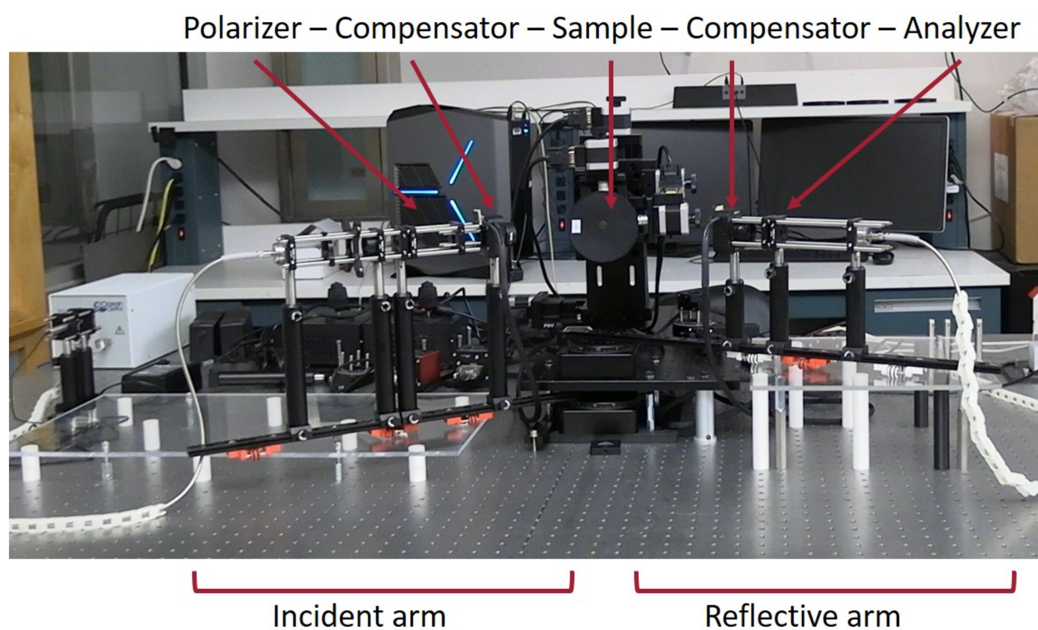

Figure 5-2: DRCE in reflection mode

The incident light arm consists of a fiber connected to the light source, a dovetail beam mounted with a fiberport collimator, an iris, a polarizer, and a compensator installed in a rotary mount. Fig. 5-4 shows the broadband light source and a laser source, used for measurement and alignment respectively. The laser is aligned with

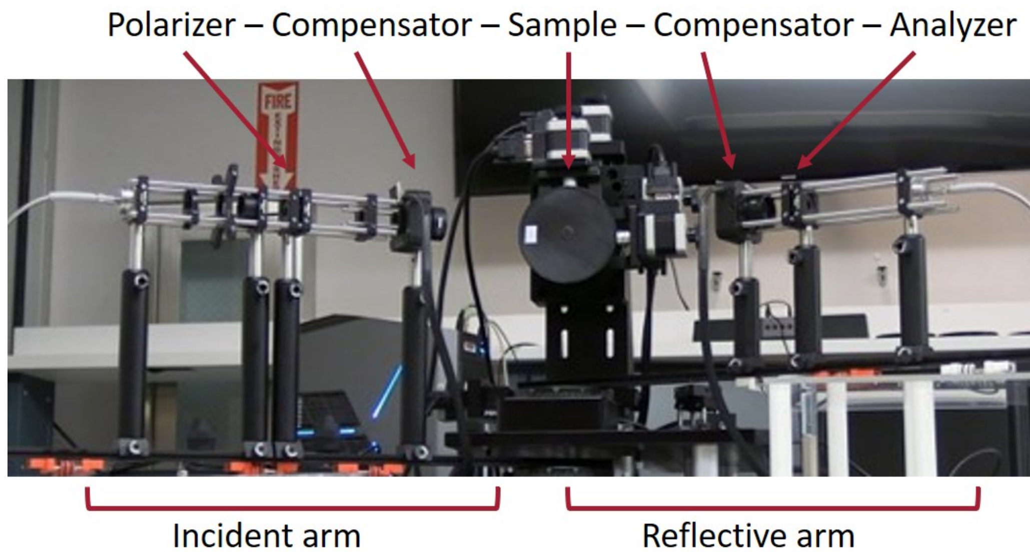

Figure 5-3: DRCE in reflection mode zoomed

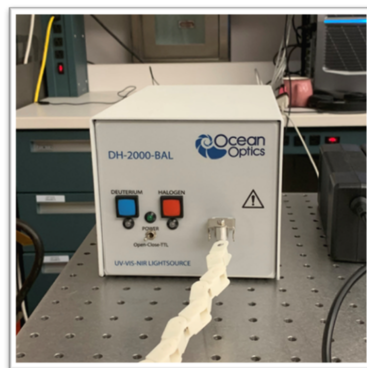

(a) Broadband light source

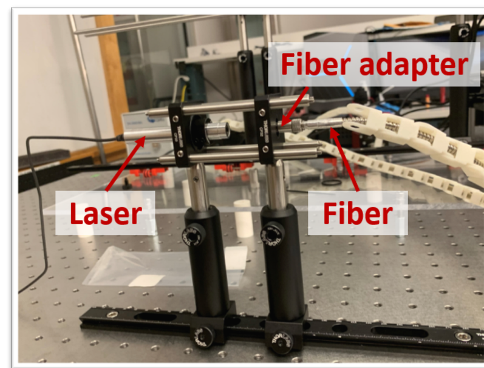

(b) Laser source

Figure 5-4: Broadband and laser light sources

a fiber adapter to allow for easy fiber connection. The rotary mount of the compensator is capable of full rotation in the plane perpendicular to the light's propagation direction. The beam is mounted on a rotary stage, which is in turn fixed onto the elevated platform. The rotary stage is capable of full rotation in the x-y plane. Fig. 5-5a shows the fixture of the beam onto the rotary state, and Fig. 5-5b shows the roller supporting the beam.

The reflective arm consists of a compensator installed in a rotary mount, an analyzer, and a fiber connected to the spectrometer. Similarly to the setup of the incident beam, the rotary mount of the compensator is capable of full rotation in the plane

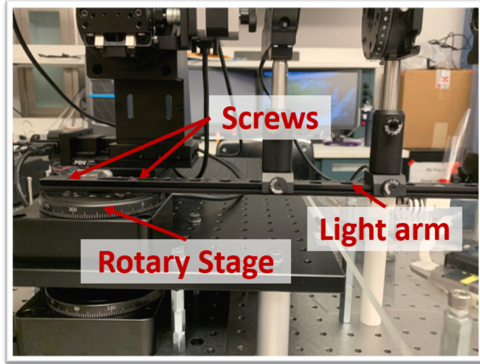

(a) Beam mounted on a rotary stage

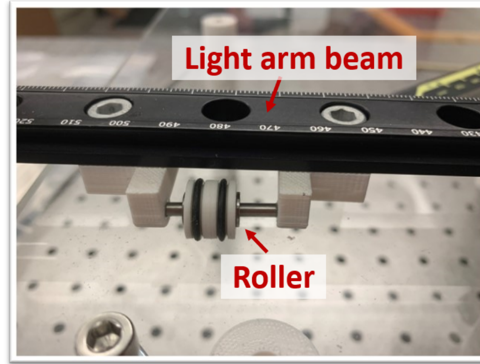

(b) Beam roller

Figure 5-5: Incident arm fixture

perpendicular to the light's propagation direction. The beam is mounted on a rotary stage, which is in turn fixed onto the elevated platform. The rotary stage is capable of full rotation in the x-y plane. The centers of the two rotary stages are aligned vertically to ensure the two light paths intersect at the same location regardless of the rotation of the two beams. Fig. 5-6 shows the fiber connected to the spectrometer. Fig. 5-7 shows the alignment of the two rotary stages.

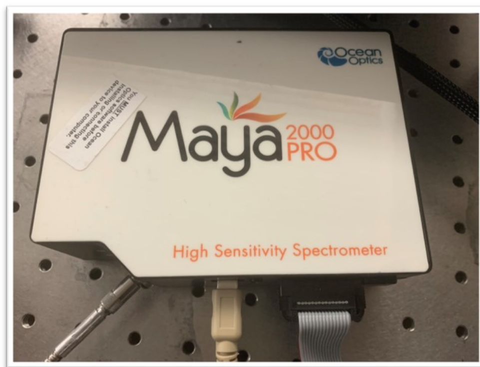

Figure 5-6: Spectrometer

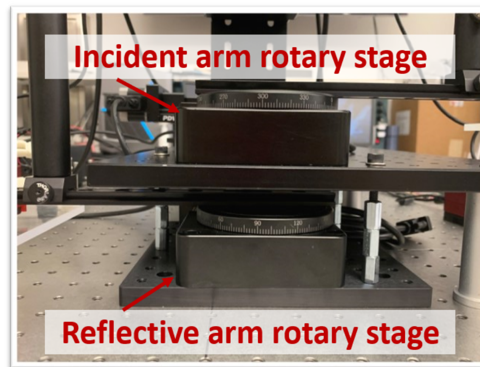

Figure 5-7: Vertically aligned rotary stages

The sample stage is mounted on the elevated platform shown in Fig. 5-1. The sample stage is a 6-DOF motorized stage assembled from three linear stages, two goniometers, and one rotary stage. The stage is shown in Fig. 5-8.

Fig 5-9 is a top-view of the setup, showing the ellipsometer at two different incident angles.

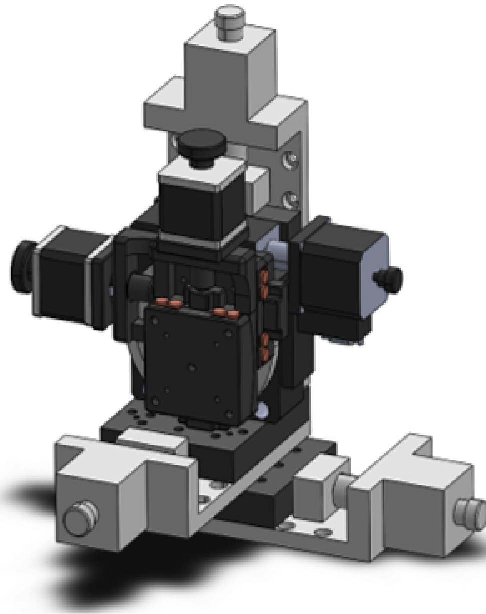

Figure 5-8: 6-DOF sample stage

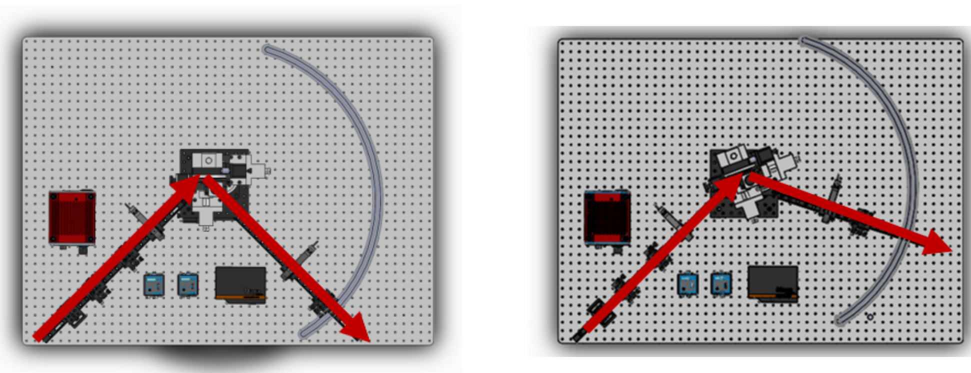

Figure 5-9: The ellipsometer at two different incident angles

5.3 Faraday Rotator Integration

The mechanical integration of the Faraday rotators is enabled by the glass holder and the utilization of cage systems of different sizes. Fig. 5-10 shows an exploded view of the holder. The glass rod is inserted in to the 3D-printed holder. The opening in the middle allows for position adjustment of the glass rod. Fig. 5-11 shows a Faraday rotator integrated into the light path. A cage system of larger size than the rest of the light path is adopted to accommodate the Faraday rotator. The ends of the holder fit into the adapter plate, and the holder rests on the posts.

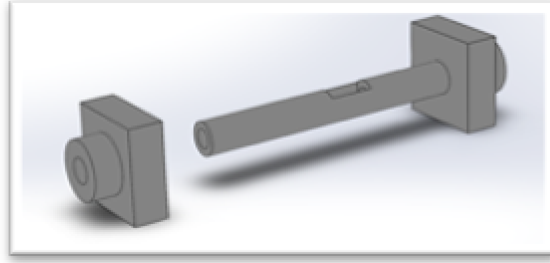

Figure 5-10: Glass holder

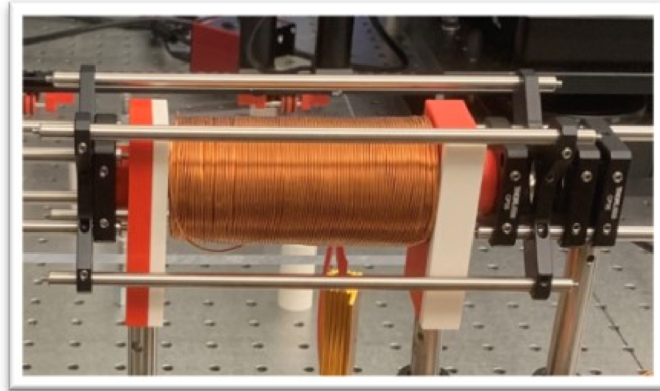

Figure 5-11: A Faraday rotator in light path

5.4 Experimental Procedure

This section provides information on the important experiment procedures: the sample preparation, the motion control, and the data collection.

5.4.1 Sample Mount

A 3D-printed part is used to hold and attach the thin film standard to the sample stage. Fig. 5-12 shows the drawing of the holder, and the mounted thin film sample. The blue region highlighted by the red circle is the effective region.

To attach the grating to the stage, first the sample is attached to a metal disk, and the disk is attached to a 3D-printed holder. For taking an AFM image, the sample and the attached metal disk are used. The grating sample has a small area, and therefore it may be difficult to observe the 0_{th} order reflection with white light. After sample is mounted, a laser light source is first used for easy visual calibration, which is then replaced with a broadband light source for measurement.

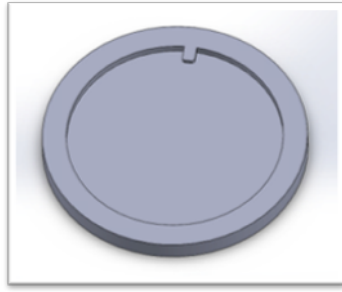

(a) Thin film holder drawing

(b) Mounted thin film sample

Figure 5-12: Mounted thin film sample

(a) Sample and metal disk

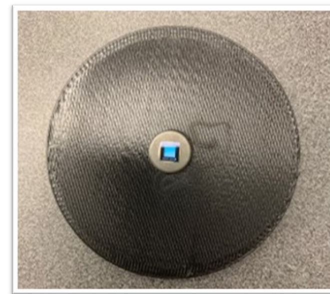

(b) Metal disk on a 3D-printed disk

Figure 5-13: Mounted grating sample

5.4.2 Motion Control

The motion control in this experiment includes the motion control of the rotary mounts of the compensators, and the motion control of the sample stage and the optical arms.

In the dual-rotating compensator ellipsometer, the rotary mounts of the compensators are controlled through ActiveX interfaced with LabVIEW. The LabVIEW front panel is shown in Fig. 5-14, where the speed and initial positions of constant-speed rotation and the speed ratio of the two compensators can be set.

From the analysis in previous sections, the measured light intensity is a sum of harmonics at any specific wavelength, at the frequencies of $2n\omega$. To validate the experimental measurement, DFT is performed on the measured intensity signal at an increment of 0.01ω to identify the peak frequencies. The phase shift from integration is accounted for. From Fig. 5-15, the peak frequencies occur at the expected frequencies. There is leakage at adjust frequencies to the peaks, which is also expected.

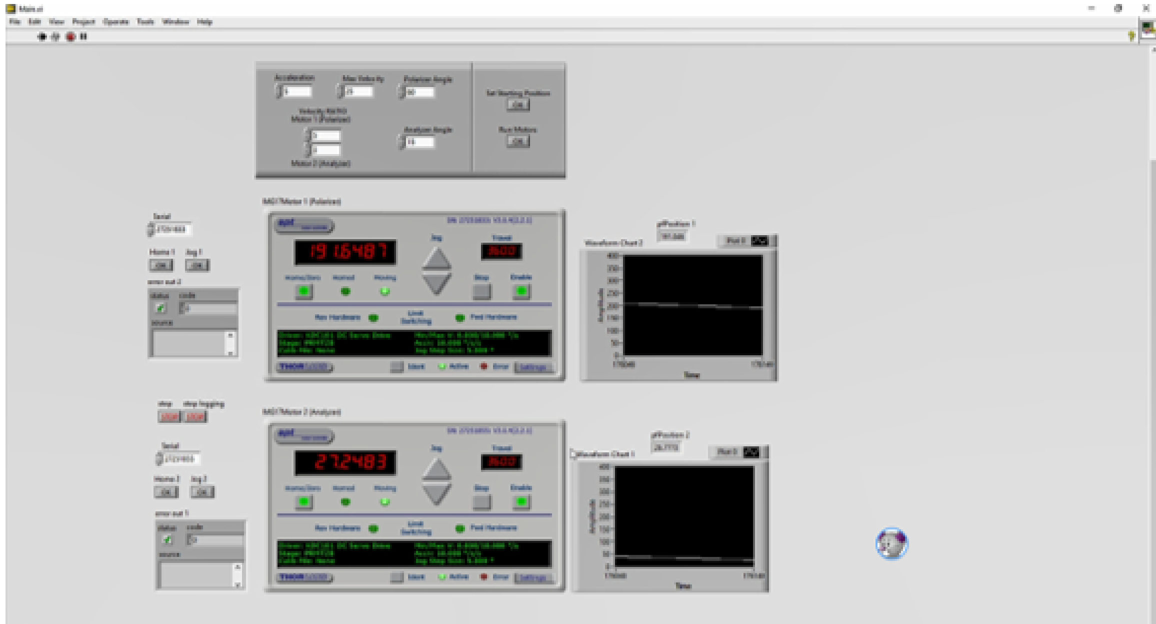

Figure 5-14: Motion control of rotary mounts.

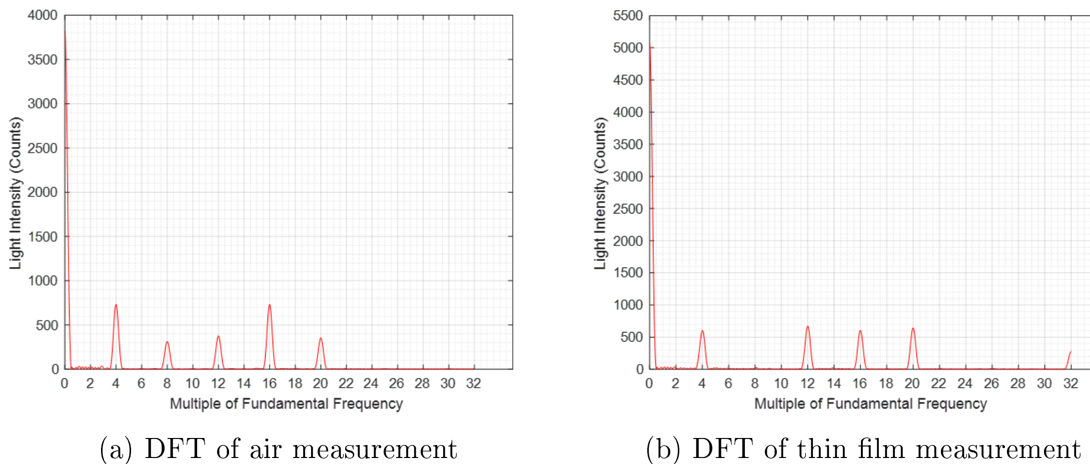

(a) DFT of air measurement (b) DFT of thin film measurement

Figure 5-15: DFT analysis of measurement

Stages that constitute the 6-DOF sample stage and the two rotary stages that carry the beams are controlled through LabVIEW. For each channel, a speed or position command can be set. The user interface is shown in Fig. 5-16.

5.4.3 Data Collection

The integration time, pixel averaging, dark current compensation can be set from the spectrometer's user interface. At the beginning of the constant-speed rotation,

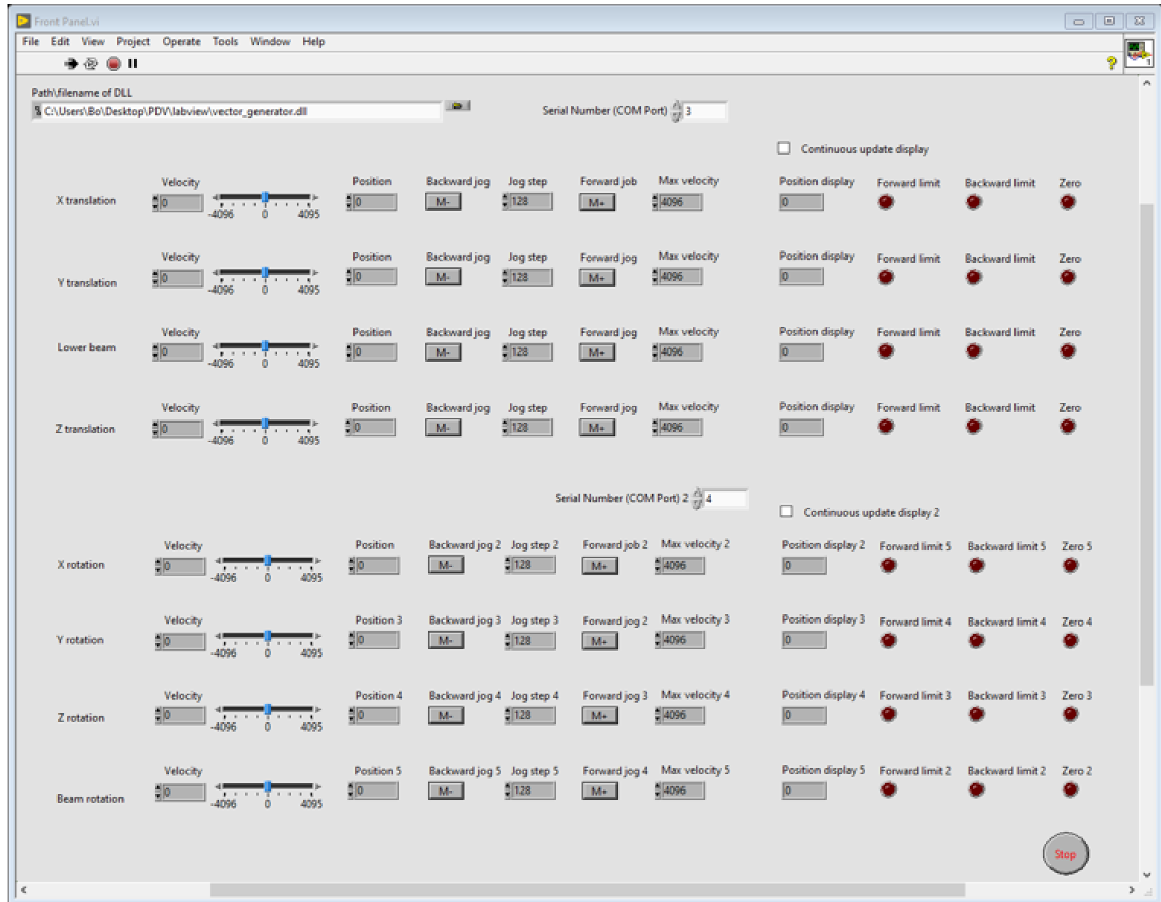

Figure 5-16: Motion control of the stage and the light arms

the controller of the compensators' rotary mounts sends sends a 5V level trigger to the spectrometer, which starts collecting and transmitting data upon receiving the trigger signal. Fig. 5-17 shows the trigger signal connection from the controller to the spectrometer. The *MATLAB* parser of the data can be found in Appendix D.

5.5 Summary

This chapter presents the in-house experiment setup and procedures in detail. Two ellipsometer systems have been implemented. The first system is a dual-rotating compensator ellipsometer, with two rotating compensators. The second system is a Faraday-rotator enabled photometric ellipsometer, which does not involve moving components. The ellipsometer setup and the integration of Faraday rotators are described, as well as the experiment procedures, including the sample mounting, motion

(a) Trigger from controller

(b) Trigger to spectrometer

Figure 5-17: Trigger from controller to spectrometer

control, and data collection. The content of this chapter supports the contributions in Chapters 2, 3 and 4.

Chapter 6

Conclusions & Recommendations

This chapter summaries the worth of this thesis in 6.1 and provides suggestions for future work in 6.2.

6.1 Conclusions

Ellipsometry, as a metrology and inspection tool, has been applied in many industries including material characterization, thin film manufacturing, and medical inspection. High-performance ellipsometry can further promote its application in nano-manufacturing. This thesis improved the performance of ellipsomtery through three aspects.

In order to improve ellipsometery's measurement accuracy and precision, this thesis proposed and verified a noise-mitigating method in ellipsometry. The measurement accuracy of ellipsometry can be significantly affected by Poisson-Gaussian noise originated from detection and environment. This thesis firstly characterized and quantified the noise through experiments on an in-house setup. The thesis then performed error propagation analysis, and provided measurement error quantification in terms of normalized Mueller matrix. Specifically, the distribution of the normalized Mueller matrix elements error was derived to analyze nonlinear propagation occurring at the normalization step. The effects of system parameters on the Poisson-Gaussian noise induced errors were studied, including signal strength, the signal sampling frequency,

and the first-order coefficient between the signal variance and mean. As expected, the error is reduced with increasing signal strength, increasing sampling frequency, and decreasing first order coefficient of the signal's variance to mean. In practice, this analysis gives the confidence interval for various experiment configuration and provides an evaluation to measurements on a spectroscopic ellipsometer, and can serve as a guidance for improving the system performance or making trade-offs in an industrial scenario. The analysis was verified by Monte Carlo simulations. This thesis then proposed a signal demodulation method in spectroscopic ellipsometry based on maximum likelihood, in order to reduce the effects of mixed Poisson-Gaussian noise. The method accounts for the signal's statistical distribution and solves for the Fourier coefficients by maximizing the probability of observed signal. The method's capability of achieving higher Mueller matrix accuracy as well as higher dimension precision and accuracy is demonstrated against DFT.

To improve the dimension reconstruction precision, this thesis developed a reconstruction method. The method improves the reconstruction's sensitivity to changes in dimensions. Higher weights are given to the critical configurations, where the measurement is sensitive to changes in dimensions. The weight selection and reconstruction algorithm are formulated. The weights are selected as partial derivative of signature with respect to dimensions. Two types of samples were experimentally measured to verify the improved precision resulted from the method. The first type of sample is thin film standard, and the thickness of which is reconstructed. The second type of sample is a grating sample, and the step height and ridge width of which are reconstructed. Two criteria were proposed to determine the range of reconstructed dimension. In all scenarios, the proposed reconstruction and weight selection demonstrated higher dimension reconstruction precision.

Lastly, a Faraday effect-based photometric ellipsometer was designed and demonstrated. The instrument has several advantages. The elimination of mechanical motion enables high-speed and high-accuracy. In addition, the linear relationship between the applied current and the rotation of the polarization plane enables fast and easy demodulation. Lastly, the operating frequency of the Faraday rotator is con-

trollable, making it compatible with most detection systems. In contrast to previous application of Faraday rotator in "null" ellipsometers, the proposed instrument operates in a photometric manner, and therefore is capable of parallel wavelength scanning. The design, data reduction, and calibration are developed. One configuration is designed and demonstrated in this thesis, capable of measuring the ellipsometric parameters. More complicated configurations incorporating Faraday rotators can be designed in the future to measure all Mueller matrix elements. Experiments are performed on air and thin film sample. The measurement on air showed good agreement with theory, and the instrument measured a thickness of 332.6 nm, while that provided by the manufacturer is 322.2 nm. This advancement will enable higher-speed measurement and better catch real-time processes.

6.2 Recommendations

This thesis opens up future research directions.

Denoising in imaging ellipsometry: In imaging ellipsometry, the accuracy and precision of the measurement could be significantly affected by the presence of mixed Poisson-Gaussian noise. This thesis proposed a Poisson denoising method in temporal polarization change-based ellipsometry. The method can be extended to imaging ellipsometry. The maximum likelihood estimation method can be applied in both temporal and spatial domain, in order to achieve higher measurement accuracy and precision in imaging ellipsometry.

Faraday effect-based photometric Mueller matrix ellipsometry: This thesis proposed a Faraday effect-based photometric ellipsometer, capable of measurement spectra of ellipsometric parameters, but cannot measure the depolarization and anisotropicity of the sample. Mueller matrix ellipsometers can measure complex samples with anistropicity and depolarization effects, and is becoming increasingly important in nanomanufacturing and material development. Future work can further develop a Faraday effect-based photometric Mueller matrix ellipsometer. The minimum requirements of the ellipsometer will be determined, including the number of Faraday rotators, the minimum rotation angle of each Faraday rotator, and the other

required optical components.

Compact design of Faraday effect-based photometric ellipsometry: One disadvantage of the proposed Faraday effect-enabled photometric ellipsometer is its large size. Future work should be devoted to the compact design of the proposed design.

Large-range scanning ellipsometer: The proposed ellipsometer measures a single spot at one time, and is capable of large-range scanning by moving the sample. The performance of the method can be affected by the positioning accuracy of the sample stage, and the large-range measurement speed is limited by the motion speed of the sample stage. To improve on the speed and positioning performance, an approach is to redirect the light beam to scan through a large-range surface. A suggested future work is to develop an ellipsometer with a light beam that can be redirected to achieve high-speed large-range scanning.

Appendix A

Supplementary Results

A.1 Supplementary Results of Chapter 2

In Chapter 2, the Monte Carlo simulation results of a grating sample is presented. In this appendix, the Monte Carlo simulation results of air is presented. The results provide supplementary support to the conclusions in Chapter 2. The number of simulations of air measurements is 4000. Fig. A-1 shows the histogram of normalized Mueller matrix elements. The blue bars represent the probability density function

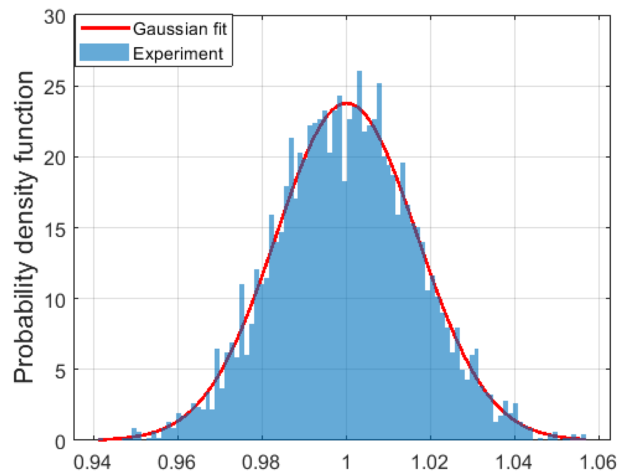

Figure A-1: Histogram of normalized air M_{33}^{n} values from simulations

from the simulations, and the red lines show the Gaussian fit. Fig. A-2 shows the probability-probability plot (P-P plot) of each MM element against a Gaussian dis-

tribution. The blue markers show the data from simulations, and the red line shows the normal distribution reference line. The air simulation also validates the approximation that each normalized MM element follows a Gaussian distribution except for M_{11}, which is a constant of 1 due to the normalization. The Gaussian approximation is also examined and verified for a smaller number of simulations. Fig. 2-9 shows the P-P plot of 200 simulations. The convergence of the Monte Carlo simulations is presented for air in Fig. A-4.

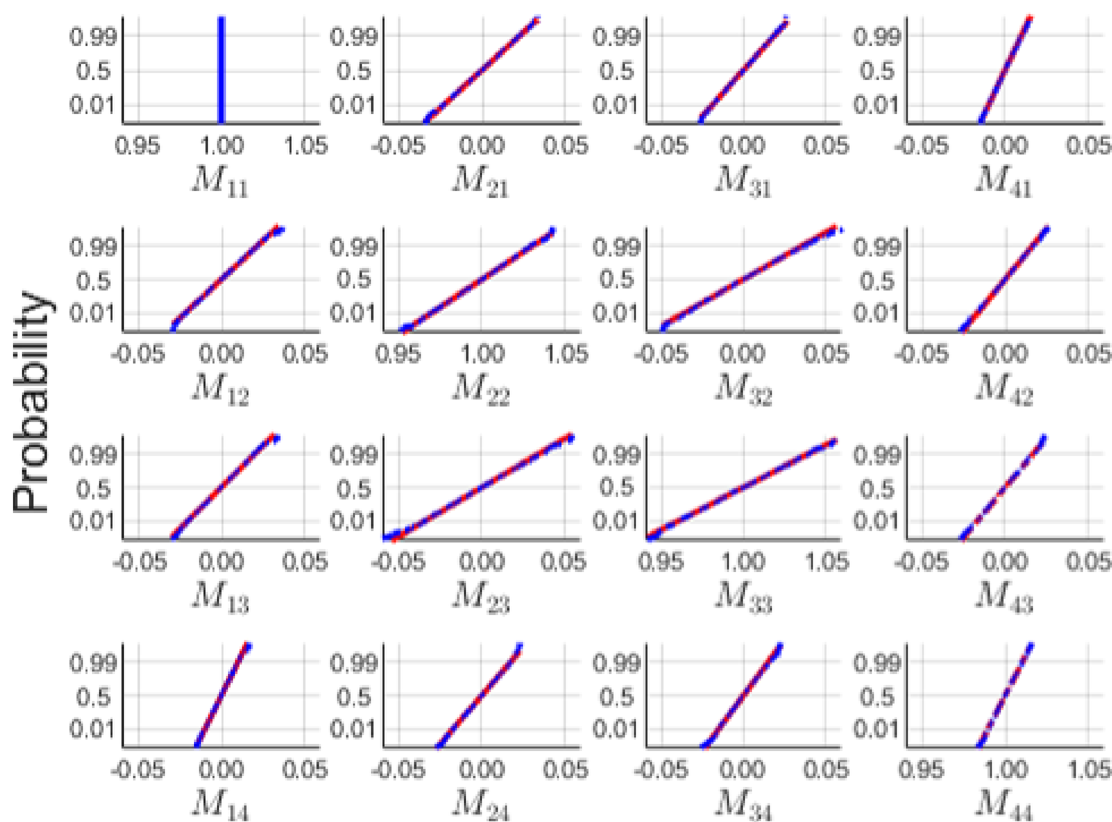

Figure A-2: Normal probability plot of normalized air MM from simulations

The derivation of normalized Mueller matrix error is also verified with Monte Carlo simulations for air. Fig. A-5 plots the mean absolute error of normalized Mueller matrix elements versus the first-order coefficient of signal variance to mean. The blue lines are from the Monte Carlo simulations and the red lines are from statistical analysis. Again the good match validates the error analysis. Same trends can be reasoned and concluded for the effects of light intensity, sampling frequency, and the first-order coefficient of signal variance to mean.

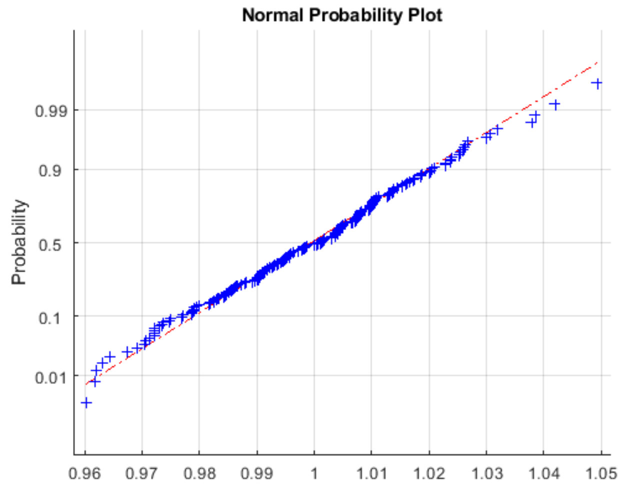

Figure A-3: Normal plot of M_{33} using 200 simulations

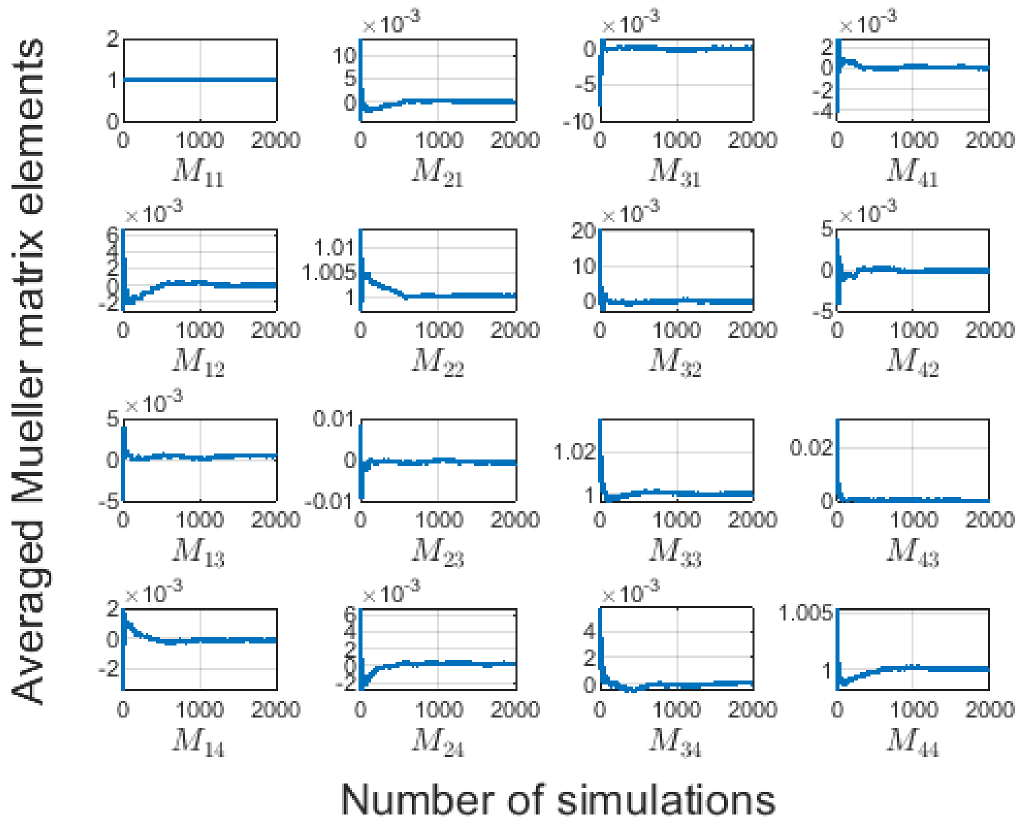

Figure A-4: Averaged Mueller matrix elements converges

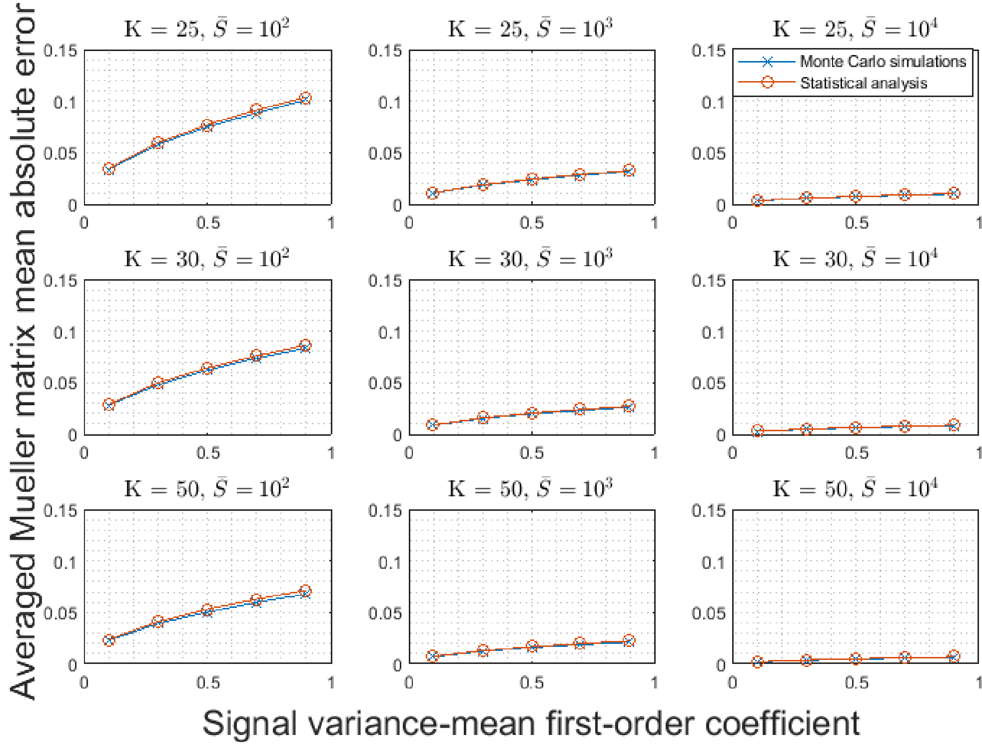

Figure A-5: The induced measurement error increases with γ_1

A.2 Supplementary Results of Chapter 3

Fig. A-6 and A-7 provides a visualization on how some configurations are more critical than the others. Fig. A-6 is the simulated Mueller matrix spectrum of a grating sample. The S_iO_2 grating is formed on S_i. The measurement is at an azimuthal angle of 0° and an incident angle of 55°. A step height of 1200 nm, and a pitch of 3010 nm and 3020 nm is simulated. The blue lines show the spectrum corresponding to a pitch of 3010 nm, and the red lines show that corresponding to a pitch of 3020 nm. Zooming in on M_{12}, it can be observed that the maximum difference between the two lines occur around 820 nm, and therefore this region is most useful in differentiating the two dimensions.

Fig. A-7a presents the sensitivity of the normalized Mueller matrix element M_{12} with respect to pitch at different wavelengths. The horizontal axis represents the wavelength, and the vertical axis represent the grating pitch. It can be observed

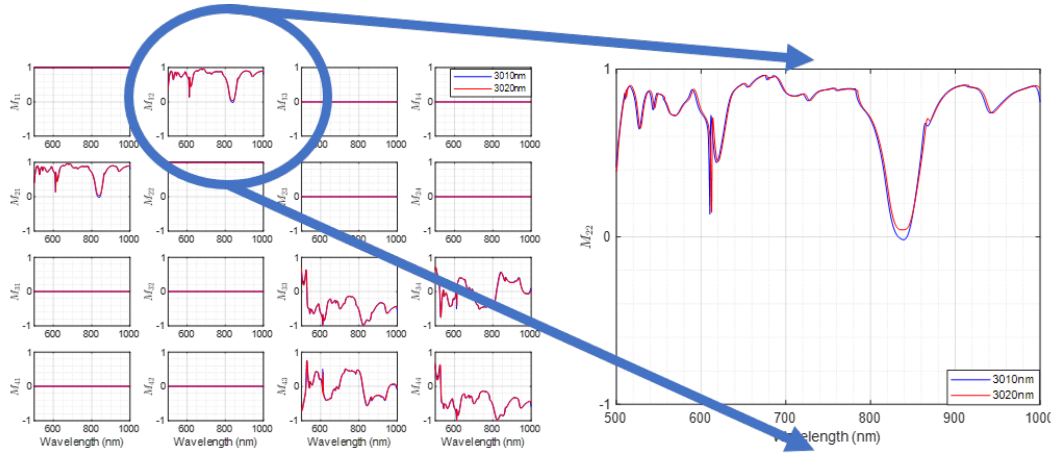

Figure A-6: Simulated Mueller matrix spectrum of a grating sample with a step height of 1250 nm

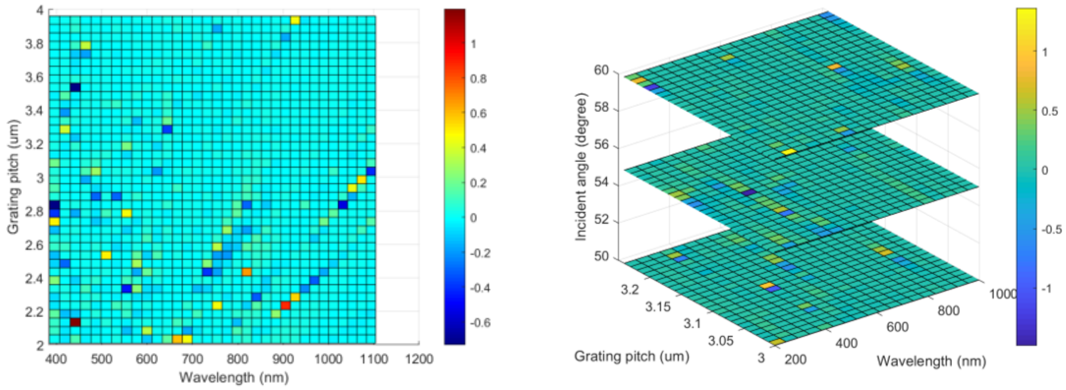

(a) Sensitivity of M_{12} to pitch

(b) Sensitivity of M_{12} at three configurations

Figure A-7: Color map

that for one pitch value, the measurement is sensitive to the pitch value at certain wavelengths, and at other wavelengths for another pitch value. Taking measurements at more configurations can further enhance measurement accuracy [138]. In Fig. A-7b, each layer represents one incident angle. Therefore, the critical configurations can be determined and given higher weights in dimension reconstruction.

The second thin film standard has a thickness of approximately 322.2 nm, and the third thin film standard has a thickness of 1031.9 nm. The pictures of the two mounted samples are shown in Fig. A-8a and A-8b respectively.

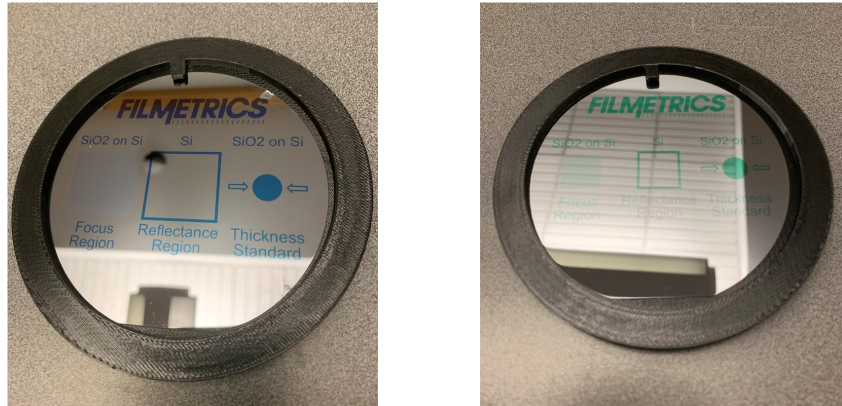

(a) Thin film sample 2 (b) Thin film sample 3

Figure A-8: Mounted thin film standards

The experimental and fitted Mueller matrix spectrum of sample 1 at incident angles of 50° and 60° are presented in Fig. A-9 and A-10 respectively.

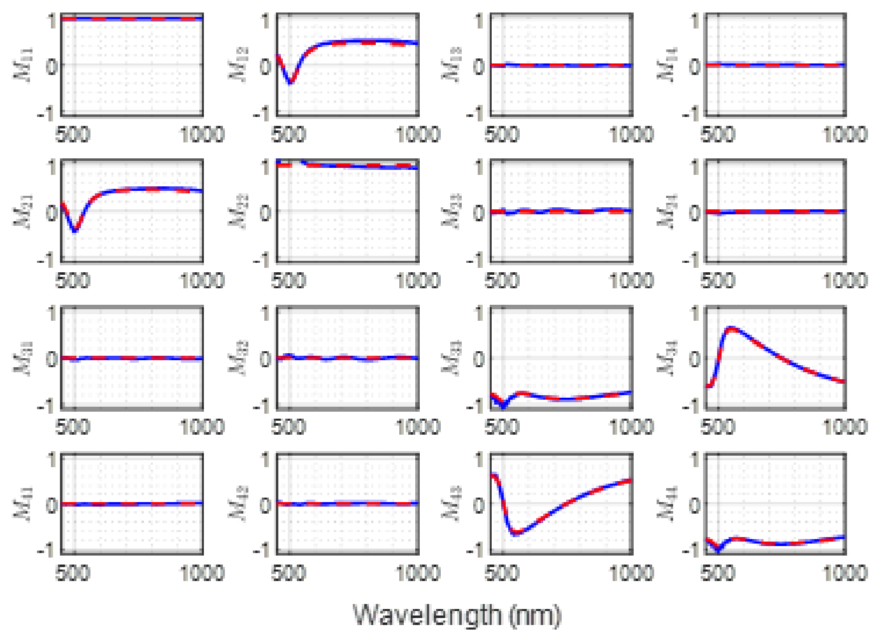

Figure A-9: Experimental and fitted Mueller matrix spectrum of thin film sample 1 at 50° incident angle

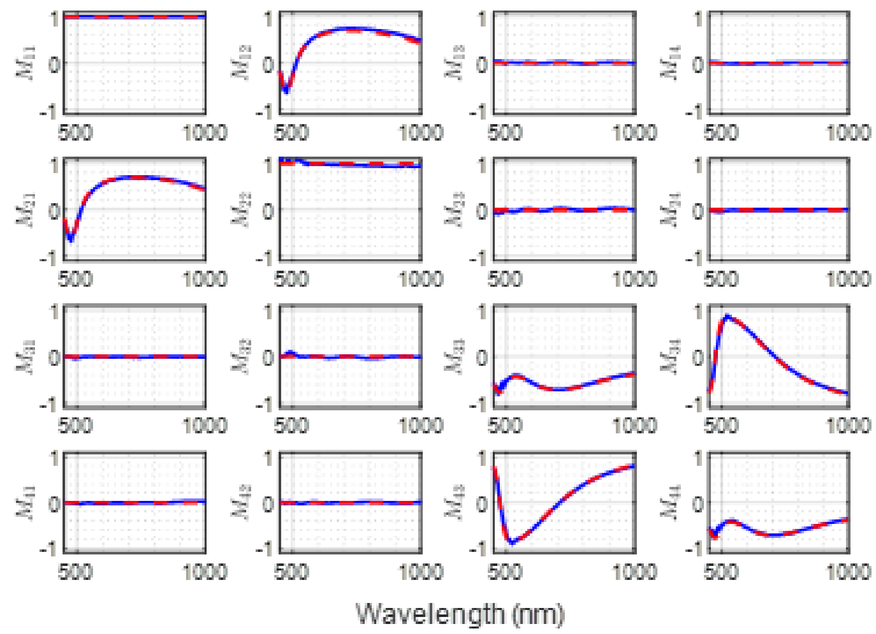

Figure A-10: Experimental and fitted Mueller matrix spectrum of thin film sample 1 at 60° incident angle

The experimental and fitted Mueller matrix spectrum of sample 2 at incident angles of 40°, 50°, and 60° are presented in Fig. A-11, A-12, and A-13 respectively.

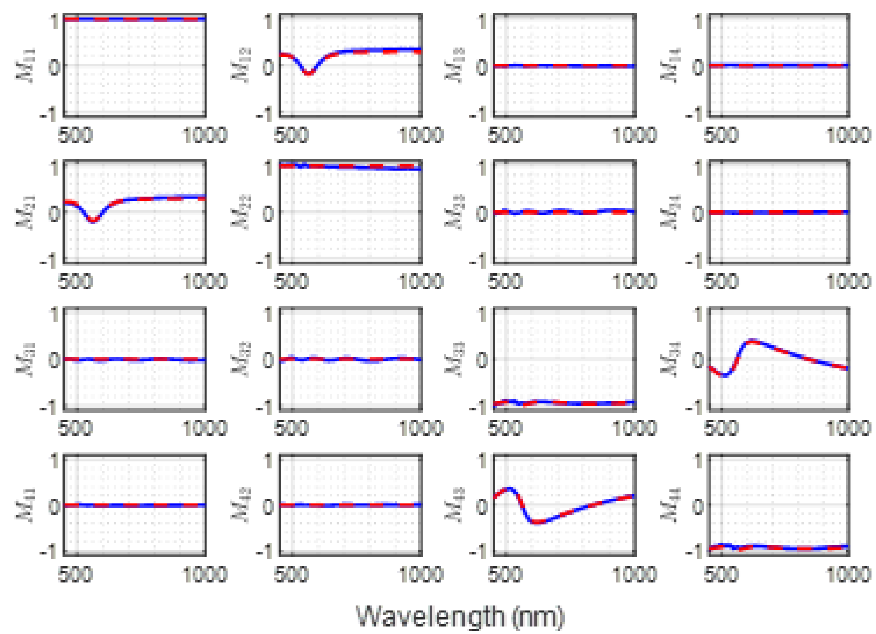

Figure A-11: Experimental and fitted Mueller matrix spectrum of thin film sample 2 at 40° incident angle

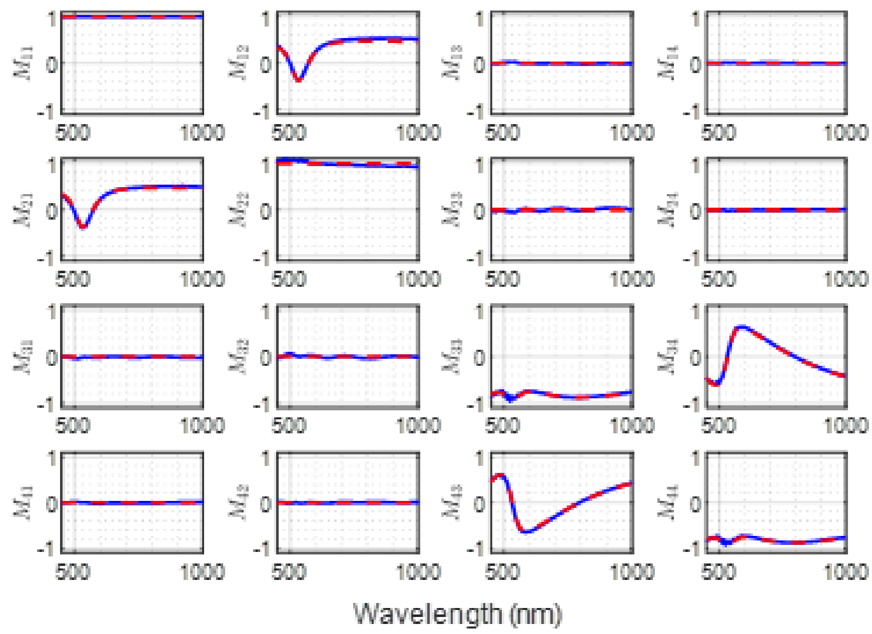

Figure A-12: Experimental and fitted Mueller matrix spectrum of thin film sample 2 at 50° incident angle

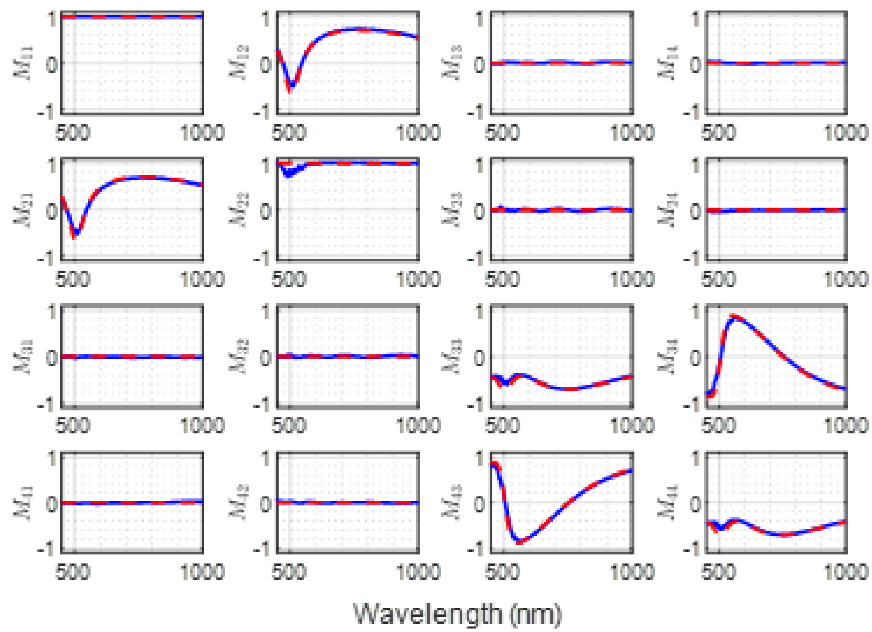

Figure A-13: Experimental and fitted Mueller matrix spectrum of thin film sample 2 at 60° incident angle

The experimental and fitted Mueller matrix spectrum of sample 3 at incident angles of 50° and 60° are presented in Fig. A-14 and A-15 respectively.

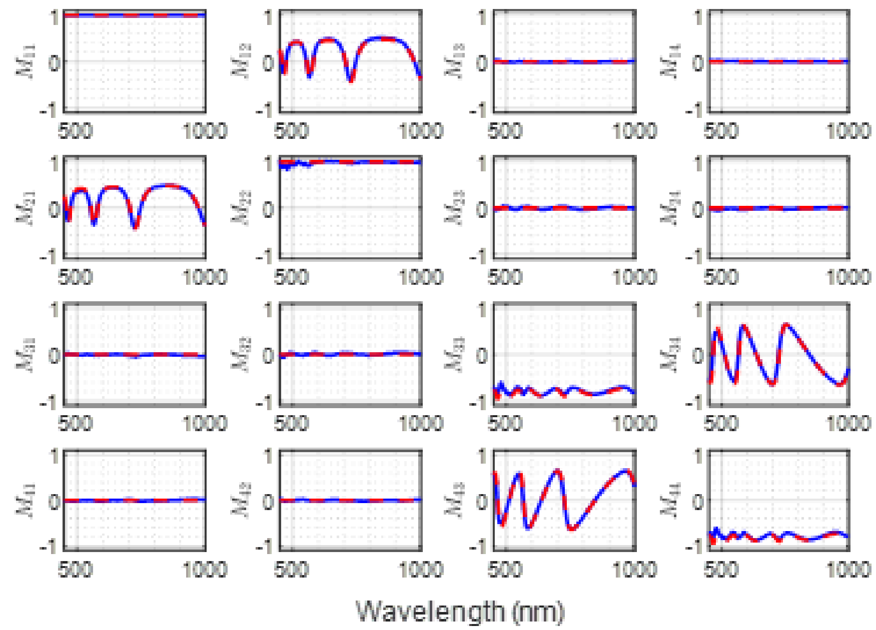

Figure A-14: Experimental and fitted Mueller matrix spectrum of thin film sample 3 at 50° incident angle

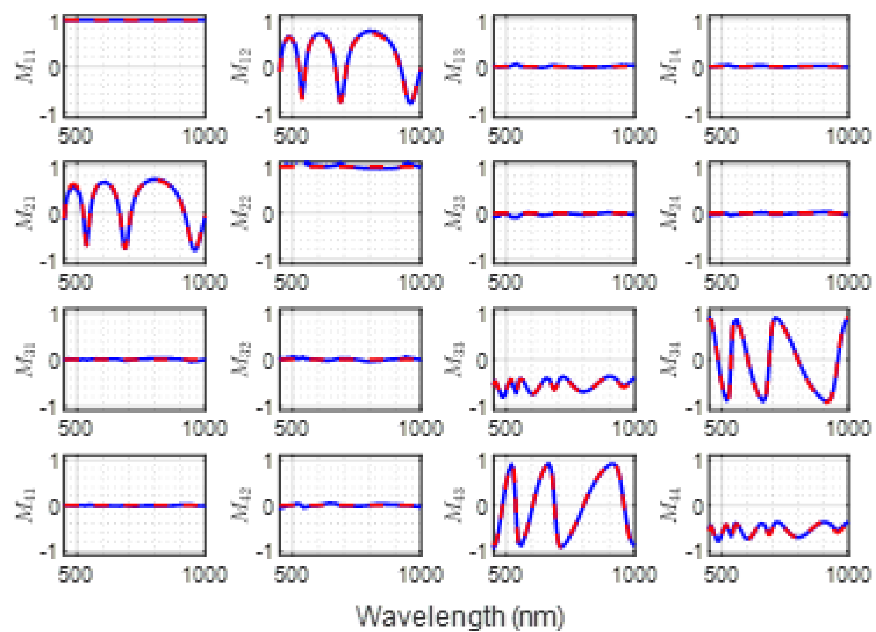

Figure A-15: Experimental and fitted Mueller matrix spectrum of thin film sample 3 at 60° incident angle

Appendix B

Bill of Materials

This appendix presents the bill of materials and the supplementary figures. The bill of materials are split into the following categories: light sources and detection system, major optical components, cage system construction components, motors and motion control components, Faraday rotators and the required electronics, construction components, fasteners, and samples. For the tables in this appendix, "Qty" is an abbreviation for "quantity".

Table B.1: Bill of materials - light sources and detection system

Component	**Vendor**	**Model**	**Qty**
Deuterium-Tungsten Halogen source	Ocean Insight	DH-2000-BAL	1
Extreme solarization resistant fibers	Ocean Insight	QP600-2-XSR	2
Spectrometer	Ocean Insight	MAYA2000PRO	1
OceanView spectrometer software	Ocean Insight	OceanView 2.0	1
Collimated laser diode module, 520 nm	Thorlabs	CPS520	1
Collimated laser diode module, 635 nm	Thorlabs	CPS635	1
5 V DC regulated power supply	Thorlabs	LDS5	1

Table B.2: Bill of materials - major optical components

Component	**Vendor**	**Model**	**Qty**
FiberPort collimator	Thorlabs	PAF2S-A4A	2
30 mm cage system iris diaphragm	Thorlabs	CP20S	1
Mounted achromatic collimator	Thorlabs	AC254-100-A-ML	1
α-BBO Rochon polarizer	Edmund	68-827	2
Achromatic quarter-wave compensator	Thorlabs	AQWP05M-600	2

Table B.3: Bill of materials - motors and motion control components

Component	Vendor	Model	Qty
Motorized linear stage	PDV	PP110-50	3
Motorized rotary stage	PDV	PX110-200	3
Motorized goniometer	PDV	PJ110-15	2
PDV controller	PDV	KZ-100	2
Compact direct drive rotation mount	Thorlabs	DDR25	2
K-Cube brushless DC servo driver	Thorlabs	KBD101	2
2.4 A Power Supply Unit	Thorlabs	KPS101	2

Table B.4: Bill of materials - Faraday rotators and the required electronics

Component	Vendor	Model	Qty
Solenoid	-	customized	2
Glass rod	TeachSpin	-	2
myRIO	National Instruments	-	1
Audio power amplifier	Taidacent	OPA549	1
DC power supply	Amazon	B07X2VZSL9	2
Heat shrink tube	Amazon	B08W2CX5F5	1

Table B.5: Bill of materials - construction components

Component	Vendor	Model	Qty
Large breadboard	PDV	PT-02PB-300x600	1
Small breadboard	Thorlabs	MB2020/M	1
Heavy-duty posts	PDV	PCB05 (25.4-76.2)	6
Acrylic sheet, 12 x 12 x 1/4 in	McMaster-Carr	4615T37	1
Acrylic sheet, 24 x 24 x 1/4 in	McMaster-Carr	8589K83	2
18-8 stainless steel dowel pin	McMaster-Carr	90145A477	12
Oil-resistant Buna-N O-ring	McMaster-Carr	9262K127	24
Stainless steel ball bearing	McMaster-Carr	57155K313	12
Push-on external retaining ring	McMaster-Carr	92133A107	24

Table B.6: Bill of materials - optical cage system construction components

Component	Vendor	Model	Qty
SM05-threaded 30 mm cage plate	Thorlabs	CP32	2
SM1-threaded 30 mm cage plate	Thorlabs	CP33	12
Drop-in 30 mm cage mount	Thorlabs	DCP1	1
Cage plate stop	Thorlabs	ERCPS	8
30 mm to 60 mm cage plate adapter	Thorlabs	LCP6X	6
30 mm to 16 mm cage plate adapter	Thorlabs	SP05	2
Cage assembly rod, 6 in long	Thorlabs	ER6	12
Cage assembly rod, 8 in long	Thorlabs	ER8	12
Cage assembly rod, 10 in long	Thorlabs	ER10	8
Cage assembly rod, 18 in long	Thorlabs	ER18	8
Compact cage assembly rod, 1 in long	Thorlabs	SR1	4
Compact cage assembly rod, 2 in long	Thorlabs	SR2	4
Dovetail optical rail, 6 in long	Thorlabs	RLA0600	1
Dovetail optical rail, 12 in long	Thorlabs	RLA1200	2
Dovetail optical rail, 24 in long	Thorlabs	RLA2400	2
Dovetail rail carrier, 1 in x 1 in	Thorlabs	RC1	12
Dovetail rail carrier, 2 in x 1 in	Thorlabs	RC2	4
Ø1/2 in post holder, 2 in long	Thorlabs	PH2	6
Ø1/2 in post holder, 3 in long	Thorlabs	PH3	4
Ø1/2 in post holder, 6 in long	Thorlabs	PH6	6
Ø1/2 in optical post, 2 in long	Thorlabs	TR2	4
Ø1/2 in optical post, 3 in long	Thorlabs	TR3	6
Ø1/2 in optical post, 6 in long	Thorlabs	TR6	6
Fixed laser mounting adapter	Thorlabs	AD11F	1
FiberPort adapter for 30 mm cage system	Thorlabs	CP08FP	2
SMA fiber thread adapter plate	Thorlabs	SM05SMA	3
SM05-SM1 thread adapter	Thorlabs	SM1A1	2
SM1 thread to Ø1 in mount adapter	Thorlabs	SM1P1	2

Table B.7: Bill of materials - fasteners

Component	Vendor	Model
Balldriver and hex key kit with stand	Thorlabs	TC2
Threaded stud and rod driver	McMaster-Carr	6197A21
Motor winding wire, 18 Gauge	McMaster-Carr	7588K63
Threaded rod, 1/4 in-20 thread, 1/2 in long	McMaster-Carr	95412A538
Threaded rod, 1/4 in-20 thread, 1 in long	McMaster-Carr	98750A011
Threaded rod, 1/4 in-20 thread, 1-1/4 in long	McMaster-Carr	98750A013
threaded rod, 1/4 in-20 thread, 4 in long	McMaster-Carr	90322A652
Threaded rod, M6 x 1 mm thread, 10 mm long	McMaster-Carr	93805A312
Threaded rod, M6 x 1 mm thread, 16 mm long	McMaster-Carr	93805A316
4-40 cap screw, 5/16 in long	Thorlabs	SH4S031
4-40 cap screw, 3/8 in long	Thorlabs	SH4S038
1/4 in-20 screw set	Thorlabs	HW-KIT2
Flat head screw, 1/4 in-20, 1 in long	McMaster-Carr	92210A542
Flat head screw, 1/4 in-20, 2 in long	McMaster-Carr	92210A550
Socket head screw, M6 x 1 mm, 6 mm long	McMaster-Carr	91290A310
Socket head screw, M6 x 1 mm, 8 mm long	McMaster-Carr	91274A135
Socket head screw, M6 x 1 mm, 30 mm long	McMaster-Carr	91290A332
Socket head screw, M6 x 1 mm, 60 mm long	McMaster-Carr	91290A207
Socket head screw, M6 x 1 mm, 70 mm long	McMaster-Carr	91290A208
Coupling nut, 1/4 in-20 thread Size, 3 in long	McMaster-Carr	90268A215
Coupling nut, 1/4 in-20 thread Size, 7/8 in long	McMaster-Carr	90977A130
Coupling nut, M6 x 1 mm thread, 18 mm long	McMaster-Carr	93355A330

Table B.8: Bill of materials - samples

Component	Vendor	Model	Qty
Thin film standard	Filmetrics	TS-Focus-SiO2-4-3100	2
Thin film standard	Filmetrics	TS-Focus-SiO2-4-10000	1
Grating	K-TEK Nanotechnology	TGZ2	1

The following supplementary figures provide a more complete description of the experiment setup. Fig. B-1 shows the isometric view, side view, and back view of the 6-DOF sample stage, and how the platform is clamped to the heavy-duty optical posts.

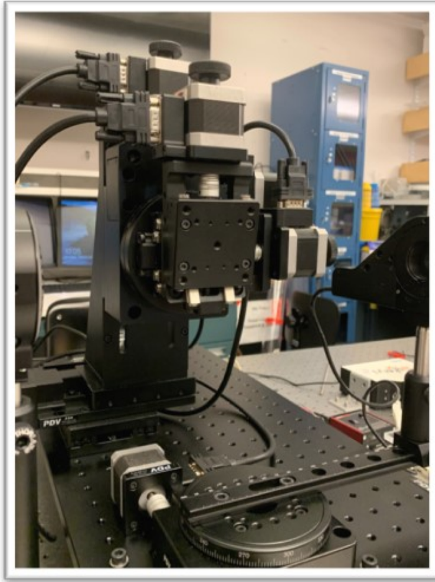

(a) Isometric view of the 6-DOF stage

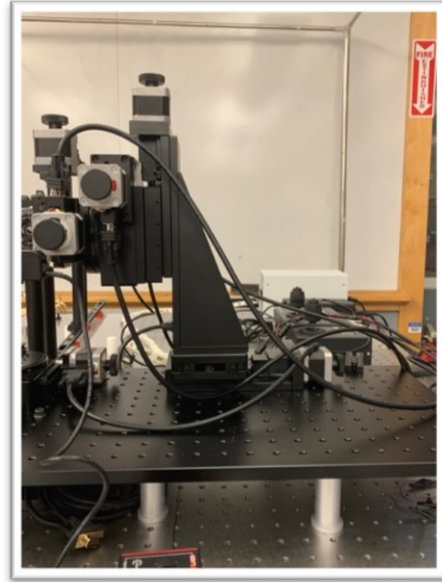

(b) Side view of the 6-DOF stage

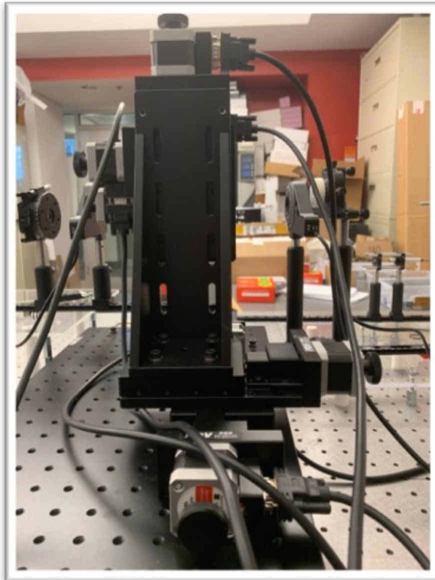

(c) Back view of the 6-DOF stage

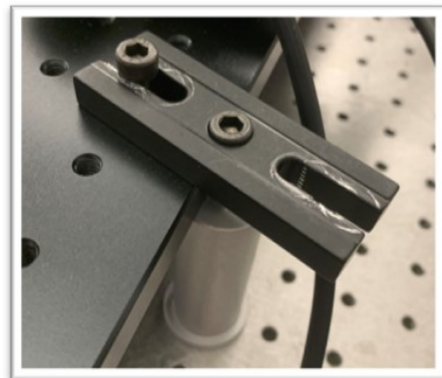

(d) Platform clamped to a heavy-duty optical post

Figure B-1: Isometric, side, and back view of the 6-DOF sample stage

Fig. B-2 shows a mounted polarizer. It is clamped between two cage plates for secure fixation. Fig. B-3 shows a compensator inside a rotary mount.

Figure B-2: Mounted polarizer

Figure B-3: Mounted compensator

Fig. B-4 shows the solenoid of a Faraday rotator. Fig. B-5 shows a glass rod, and the 3D printed part designed to hold the glass rod. The solenoid is mounted on the glass holder to construct the Faraday rotator in Fig. 5-11.

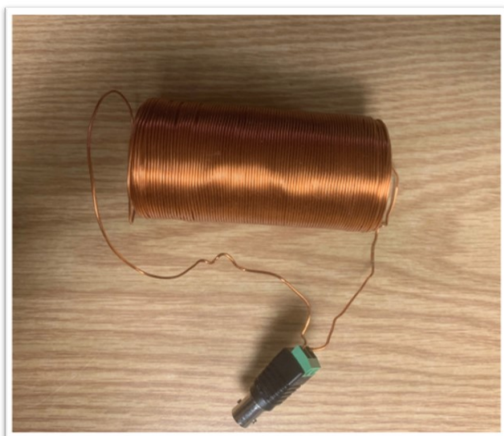

Figure B-4: Solenoid

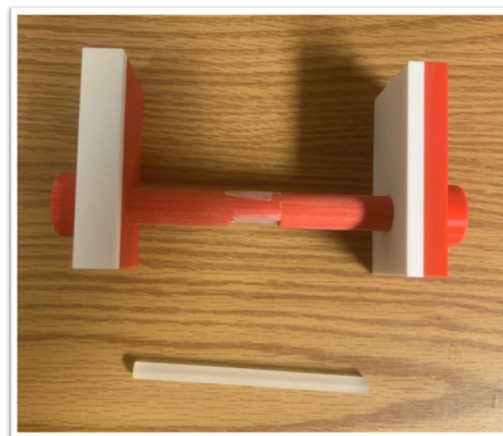

Figure B-5: Glass rod and its holder

Appendix C

Fundamental concepts in statistics and computation

C.1 Statistics

Mean: The mean of a random variable is its averaged value [139].

Variance and covariance: The variance of a random variable measures how spread out it is from its mean. The variance of a random variable is calculated as the squared difference from its mean [139].

Correlation and auto-correlation: The correlation between two random variables measures how strongly they are linearly related [139]. Autocorrelation is the correlation between a time series and a lagged copy of itself [139].

Lilliefors test: The Lilliefors test can test a data set to a null hypothesis and decide if the data set is from a normal distribution [140].

C.2 Processes:

Folded normal distribution: Taking the absolute value of a normally distributed random variable, the formed distribution is a folded normal distribution [141].

Poisson distribution: Poisson distribution is a discrete probability distribution.

It describes the probability of a given number of events occurring in a fixed time interval. The events occur with a known constant mean rate and the probability of event occurring is independent of the elapsed time since the last event [142].

Cauchy distribution: Given two independent normally distributed random variables with zero mean, Cauchy distribution is the distribution of the ratio of the two random variables [139].

Chi-squared distribution: Chi-squared distribution is obtained by summing k independent standard standard normal random variables [141].

C.3 Computation methods

Monte Carlo simulation: Monte Carlo simulations are used to model the probability of different outcomes by repeatedly and randomly sample from a distribution [143].

Maximum likelihood estimation: Maximum likelihood estimation is a method for estimating the value of one more parameters of probability distributions based on observations. The objective function is the probability of the observation occurring, and should be maximized [139].

Discrete Fourier Transform: Discrete Fourier Transform (DFT) converts a series of equally spaced samples of a signal or function to a sequence of complex numbers in the frequency domain [144].

Hadamard Transform: is a generalized Fourier transform method [145] Only real number additions and subtractions are required in the computation, and therefore a high computation speed is achievable.

Anscombe Transform: Anscombe transform stabilizes the variance of a Poisson random variable by converting it into a random variable with an approximately standard Gaussian distribution [146].

Rigorous Couple Wave Analysis: Rigorous coupled-wave analysis (RCWA) is a semi-analytical method. It describes the diffraction of electromagnetic waves scatted from by period dielectric structures [147].

Appendix D

Codes

In this appendix, the important codes to support the work in this thesis are listed.

- Listing D.1 is the parser of spectrometer data.
- Listing D.2 and D.3 shows the high-level codes of Monte Carlo simulations to study the effects and mitigation of Poisson-Gaussian noise in Chapter 2.
- Listing D.4 shows the top-level file of processing data from Dual-Rotating Compensator Ellipsometer.
- Listing D.5 is the dimension reconstruction codes in Chapter 3.
- Listing D.6 is for calibrating the Verdet constant in Chapter 4.
- Listing D.7 shows the calibration and signal processing presented in 4.

Listing D.1: Spectrometer data parser

```
1  clear all; close all; clc;
2
3  %% extract files
4  dirfol = '';
5
6  % find all files in the specified folder and extract the ...
       filenames as an array
7  addpath(dirfol);
8  listing = dir(dirfol);
9  filenames = [];
10 for i = 3:size(listing,1)
11     filenames = [filenames string(listing(i).name)];
12 end
13
14 %% extract the time, wavelength, intensity and save with the filename
15 for i = 1:size(filenames,2)
16     filename = filenames(i);
17     maya_table = readtable(filename);
18     maya_time = maya_table(:,1);
19     maya_time = table2array(maya_time);
20     maya_data = maya_table(:,3:end);    % one row contains all ...
           wavelengths at one time
21     maya_data = table2array(maya_data);
22     filename = strrep(filename,'.txt','.mat');
23     file = strcat(dirfol,'/',filename);
24     save(file, 'maya_time', 'maya_data');
25 end
```

Listing D.2: Monte Carlo simulations of broadband light source

```
clear all; close all; clc;

% user defined parameters
load('f')
n_sim = 6000;
P_exp = 0;     Ps = 0;      Pp = P_exp-Ps;
A_exp = 0;     As = 0;      Ap = A_exp-As;
n_Fcoeff     = 1; % 0 is air, 1 is grating sample
int_int      = 1; % 1 if using number of measurements, 0 if using dt
multi_int    = 1; % 1 if using int matrix, 0 if using single value
multi_scale = 1; % 1 if using scale matrix, 0 if using a single value
multi_f      = 1; % 1 if using multiple values

% intensity scale
if multi_scale
    scale_m = logspace(1,4,4);
else
    scale_m = 1e3;
end
n_scale = size(scale_m,2);

% noise magnitude (variance-mean first-order coefficients)
if multi_f
    p1_m = [0.1 f.p1 1/2 1];
else
    p1_m = f.p1;
end
n_f   = size(p1_m,2);

% number of integrations during one optical period
if multi_int
    n_int_m = [25 40 50 70];
else
    n_int_m = 45;
end
```

```
36 n_n_int = size(n_int_m,2);
37
38 % divide signal
39 n_int = 16;
40 omega = 5/180*pi;
41 T = pi/omega;
42 if int_int == 1
43     dt = T/n_int;
44 elseif int_int == 0
45     dt = 30/1000;
46     n_int = T/dt;
47 end
48
49 % load parameters
50 ind_wave = 51:10:111;
51 n_wave = max(size(ind_wave));
52 ind_thick = 5;
53 ind_pitch = 250;
54 ind_phi = 1;
55 ind_theta = 2;
56 if n_Fcoeff
57     load('Mueller8')
58     M_multi = squeeze(Mueller(:,:,ind_wave,...
59         ind_thick,:,:,ind_pitch, ind_phi,ind_theta));
60     clear('Mueller')
61 else
62     M_multi = zeros(4,4,n_wave);
63     for i_wave = 1:n_wave
64         M_multi(:,:,i_wave) = eye(4);
65     end
66 end
67 Δ1 = 2*pi/4;
68 Δ2 = 2*pi/4;
69
70 cali = 0;
71 M_log_wave   = zeros(n_wave, n_n_int, n_scale, n_sim, n_f, 6, 4, 4);
72 Sn_log_wave  = zeros(n_wave, n_n_int, n_scale, n_sim, n_f, ...
```

```
    max(n_int_m));
73 Sm_log_wave   = zeros(n_wave, n_n_int, n_scale, n_sim, n_f, ...
    max(n_int_m));
74 Hs_wave       = zeros(n_wave, n_n_int, n_scale, n_sim, n_f);
75
76 for i_wave = 1:n_wave
77     M = squeeze(M_multi(:,:,i_wave));
78     [M_log, Sn_log, Sm_log, Hs] = max_like_single(cali, M, Pp, ...
79         Ap, Δ1, Δ2, T, n_int_m, n_n_int, scale_m, n_scale, ...
80         p1_m, n_f, n_sim, omega, i_wave);
81     M_log_wave(i_wave,:,:,:,:,:,:,:)     = M_log;
82     Sn_log_wave(i_wave,:,:,:,:,:,:)      = Sn_log;
83     Sm_log_wave(i_wave,:,:,:,:,:,:)      = Sm_log;
84     Hs_wave(i_wave,:,:,:,:)              = Hs;
85 end
```

Listing D.3: Monte Carlo simulations at a single wavelength

```
function [M_log, Sn_log, Sm_log, Hs] = max_like_single(cali, M, ...
    Pp, Ap, Δ1, Δ2, T, n_int_m, n_n_int, scale_m, n_scale, ...
    p1_m, n_f, n_sim, omega, i_wave)

    ind = [1 2 3 4 5 6 7 8 10 11 13 16];
    empty = setdiff(1:16,ind);
    [I0_p alpha_p beta_p] = M2coeff(M,Pp,Ap,Δ1,Δ2);
    save('I0_p','I0_p')
    save('alpha_p','alpha_p')
    save('beta_p','beta_p')

    %% simulate many experiments and compare the two methods: ...
        minimize RMSE and maximize probability
    % pseudo code
    % for i_n_int = 1:n_n_int
    %      calcualte Sm
    %      calculate M
    %      for i_scale = 1:n_scale
    %          scale Sm
    %          for i_f = 1:n_f
    %              reset f.p1
    %              for i_sim = 1:n_sim
    %                  calcualte Sn
    %              end
    %          end
    %      end
    % end
    M_log   = zeros(n_n_int, n_scale, n_sim, n_f, 6, 4, 4);
    Sn_log  = zeros(n_n_int, n_scale, n_sim, n_f, max(n_int_m));
    Sm_log  = zeros(n_n_int, n_scale, n_sim, n_f, max(n_int_m));
    Hs      = zeros(n_n_int, n_scale, n_sim, n_f);

    % for each integration number, calculate coefficients, A matrix
    for i_n_int = 1:n_n_int
        n_int = n_int_m(i_n_int);
```

```
35          dt = T/n_int;
36          tm = 0:dt:dt*(ceil(T/dt));
37          Sm = zeros(size(tm,2)-1, 1);
38          load('I0_p'); load('alpha_p'); load('beta_p');
39          for i = 1:size(Sm,1)
40              tmin = tm(i);
41              tmax = tm(i+1);
42              Sm(i) = I0_p*(tmax-tmin);
43              for i_ind = 1:16
44                  Sm(i) = Sm(i) + 1/i_ind/omega * ...
                        sin((tmax-tmin)*i_ind*omega) * ( ...
                        alpha_p(i_ind)*cos((tmin+tmax)*i_ind*omega) + ...
                        beta_p(i_ind)*sin((tmin+tmax)*i_ind*omega) );
45              end
46          end
47          A = zeros(n_int,32);     % find A matrix correlating ...
                Fourier coefficients to Sm
48          for i_int = 1:n_int
49              tmin = (i_int-1)*pi/(n_int*omega);
50              tmax = i_int*pi/(n_int*omega);
51              for i_ind = 1:16
52                  A(i_int,i_ind) = 1/i_ind/omega * ...
                        sin((tmax-tmin)*i_ind*omega) * ...
                        cos((tmin+tmax)*i_ind*omega);
53                  A(i_int,i_ind+16) = 1/i_ind/omega * ...
                        sin((tmax-tmin)*i_ind*omega) * ...
                        sin((tmin+tmax)*i_ind*omega);
54              end
55          end
56          A(:, [empty,empty+16]) = [];
57          Ac2s = [ones(n_int,1)*dt A];
58          xa = [I0_p; alpha_p(ind); beta_p(ind)];
59          Am2c = m2c_getA(Δ1,Δ2,Pp,Ap);
60          Ax = Ac2s*Am2c;
61
62          % for each scale, scale Sm
63          for i_scale = 1:n_scale
```

```
64              scale = scale_m(i_scale);
65              Sm_scale = scale*Sm;
66              Sm_scale(Sm_scale<0) = 0;
67              xa_scale = scale*xa;
68              alpha_p = zeros(16,1);
69              beta_p = zeros(16,1);
70              if cali
71                  alpha_p(ind) = xa_scale(2:13);
72                  beta_p(ind) = xa_scale(14:25);
73                  [I0, alpha, beta, Ps, As, ¬] = ...
                       unprime(xa_scale(1), alpha_p, beta_p);
74                  Δ1 = 2*atan(sqrt(sqrt(alpha_p(4)^2+beta_p(4)^2) ...
75                      /sqrt(alpha_p(6)^2+beta_p(6)^2)));
76                  Δ2 = 2*atan(sqrt(sqrt(alpha_p(4)^2+beta_p(4)^2)...
77                      /sqrt(alpha_p(10)^2+beta_p(10)^2)));
78                  Pp=P_exp-Ps; Ap=A_exp-As;
79              else
80                  xa = linsolve(Ac2s,Sm_scale);
81                  I0 = xa(1);
82                  alpha(ind) = xa(2:13);
83                  beta(ind)  = xa(14:25);
84              end
85              Ma= m_eqns_pc_dft(I0,alpha,beta,Δ1,Δ2,Pp,Ap);
86
87              % for each noise magnitude, add noise
88              for i_f = 1:n_f
89                  f.p1 = p1_m(i_f);
90                  for i_sim = 1:n_sim
91                      Sn = zeros(size(Sm_scale));
92                      S_var = f.p1*Sm_scale+f.p2;
93                      S_var(S_var<0) = 0;
94                      for i_int = 1:n_int
95                          Sn(i_int) = normrnd(Sm_scale(i_int),...
96                              sqrt(S_var(i_int)));
97                      end
98                      Sn(Sn<0) = 1;
99                      % 1) a system of linear equations to minimize ...
```

```
            rmse
100     x_lin = linsolve(Ac2s, Sn);
101     % 2) a system of nonlinear equations to ...
            maximize probability
102     x0 = x_lin;
103     fun = @(x) prob_eqn(x, Ac2s, Sn, f);
104     options_eqn = ...
            optimoptions('fsolve','Display','none');
105     x_eqn = fsolve(fun,x0,options_eqn);
106     % calculate probability solution
107     H = compute_Hessian(x_eqn,Ac2s,Sn,f);
108     if min(eig(H))>0
109         Hs(i_n_int, i_scale,i_sim,i_f) = 1;
110     end
111     % 3) an optimization to maximize probability
112     x0 = x_lin;
113     fun = @(x) probfun_int(x, Sn, Ac2s, f);
114     Af = -Ac2s;
115     b = zeros(size(Sn));
116     options = ...
            optimoptions('fmincon','Display','off');
117     x_prob = fmincon(fun, x0, Af, b, [], [], [], ...
            [], [], options);
118
119     alpha_p = zeros(16,1);
120     beta_p = zeros(16,1);
121     alpha = zeros(16,1);
122     beta = zeros(16,1);
123     if cali
124         alpha_p(ind) = x_lin(2:13);
125         beta_p(ind) = x_lin(14:25);
126         [I0, alpha, beta, Ps, As, ¬] = ...
127             unprime(x_lin(1), alpha_p, beta_p);
128         ∆1 = 2*atan...
129             (sqrt(sqrt(alpha_p(4)^2+beta_p(4)^2)...
130             /sqrt(alpha_p(6)^2+beta_p(6)^2)));
131         ∆2 = 2*atan...
```

```
132                         (sqrt(sqrt(alpha_p(4)^2+beta_p(4)^2)...
133                         /sqrt(alpha_p(10)^2+beta_p(10)^2)));
134                     Pp=P_exp-Ps; Ap=A_exp-As;
135                     M_lin= m_eqns_pc_dft(I0,alpha,beta, ...
136                         Δ1,Δ2,Pp,Ap);
137
138                     alpha_p = zeros(16,1);
139                     alpha_p(ind) = x_eqn(2:13);
140                     beta_p = zeros(16,1);
141                     beta_p(ind) = x_eqn(14:25);
142                     [I0, alpha, beta, Ps, As, ¬] = ...
143                         unprime(x_eqn(1), alpha_p, beta_p);
144                     Δ1 = 2*atan...
145                         (sqrt(sqrt(alpha_p(4)^2+beta_p(4)^2)...
146                         /sqrt(alpha_p(6)^2+beta_p(6)^2)));
147                     Δ2 = 2*atan...
148                         (sqrt(sqrt(alpha_p(4)^2+beta_p(4)^2)...
149                         /sqrt(alpha_p(10)^2+beta_p(10)^2)));
150                     Pp=P_exp-Ps; Ap=A_exp-As;
151                     M_eqn= ...
                            m_eqns_pc_dft(I0,alpha,beta,Δ1,Δ2,Pp,Ap);
152                 else
153                     I0 = x_lin(1);
154                     alpha(ind) = x_lin(2:13);
155                     beta(ind) = x_lin(14:25);
156                     M_lin= ...
                            m_eqns_pc_dft(I0,alpha,beta,Δ1,Δ2,Pp,Ap);
157                     I0 = x_eqn(1);
158                     alpha(ind) = x_eqn(2:13);
159                     beta(ind) = x_eqn(14:25);
160                     M_eqn= ...
                            m_eqns_pc_dft(I0,alpha,beta,Δ1,Δ2,Pp,Ap);
161                     I0 = x_prob(1);
162                     alpha(ind) = x_eqn(2:13);
163                     beta(ind) = x_prob(14:25);
164                     M_prob = ...
                            m_eqns_pc_dft(I0,alpha,beta,Δ1,Δ2,Pp,Ap);
```

```
165                         end
166
167                         M1 = reshape((Ax'*Ax)^(-1)*Ax'*Sn,[4,4]);
168                         M2 = reshape(linsolve(Am2c,x_lin),[4,4]);
169                         M_log(i_n_int,i_scale,i_sim,i_f,1,:,:)=M_lin;
170                         M_log(i_n_int,i_scale,i_sim,i_f,2,:,:)=M_eqn;
171                         M_log(i_n_int,i_scale,i_sim,i_f,3,:,:)=Ma;
172                         M_log(i_n_int,i_scale,i_sim,i_f,4,:,:)=M1;
173                         M_log(i_n_int,i_scale,i_sim,i_f,5,:,:)=M2;
174                         M_log(i_n_int,i_scale,i_sim,i_f,6,:,:)=M_prob;
175                         Sn_log(i_n_int,i_scale,i_sim,i_f,1:n_int)=Sn;
176                         Sm_log(i_n_int,i_scale,i_sim,i_f,1:n_int)=Sm_scale;
177                     end
178                 end
179             end
180         end
181     end
```

Listing D.4: Top-level file of DRCE processing

```
1  clear all; close all; clc;
2  restoredefaultpath;
3
4  %% define parameters
5  addpath(dirfol);
6  addpath('data');
7
8  listing = dir(dirfol);
9  file_strs = [];
10 for i = 3:size(listing)
11     file_strs = [file_strs string(listing(i).name)];
12 end
13 file_strs = sort(file_strs);
14
15 P = 0;
16 A = 0;
17 omega = 5/180*pi;
18 n_p = 2;        % number of periods to use
19 width = 1;      % decide the spectral width of the light sources
20 scale = 1;      % scale up/down the integrated intensity
21
22 t_interval = 30/1000;
23 t_initial = 0;
24
25 solver_ind = 1;
26 if solver_ind == 1
27     solver = 'dft';
28 elseif solver_ind == 2
29     solver = 'hadamard_linear';
30 elseif solver_ind == 3
31     solver = 'Fourier_maximum';
32 end
33 % solver takes 'dft', 'hadamard_nl', 'hadamard_linear'
34
35 load('maya_wavelen');
```

```
36 w = maya_wavelen(maya_wavelen>450 & maya_wavelen<950);
37 w = w';
38 wl = min(w);
39 wu = max(w);
40
41 %% measure unknown sample(s)
42 Ps   = Ps_m;
43 As   = As_m + Ps;
44 Cs1 = Cs1_m + Ps ;
45 Cs2 = Cs2_m + Ps;
46
47 for i = 1:max(size(file_strs))
48     file_str = file_strs(i);
49     mode = 'calibrated';
50     [M_unknown, error_unknown, ¬] = air_pc(file_str, omega, ...
51         n_p, P, A, w, width, scale, ∆_air, t_interval, ...
52         t_initial, mode, solver, Ps, As, Cs1, Cs2);
53
54     error_m(i,:) = error_unknown;
55     M(:,:,:,i) = M_unknown;
56
57     sample = 'general';
58     plot_results(sample, w, M_unknown, error_m)
59 end
```

Listing D.5: Thin film thickness reconstruction

```
clear all; close all; clc;

inc_m    = [40 50 60];
n_inc    = size(inc_m,2);
diff_l   = 550;
diff_u   = 1800;
n_diff   = diff_u - diff_l+1;
load('maya_wavelen')
n_wave   = size(maya_wavelen,2);

for i_sample = 1:3
    % load simulated data
    if i_sample == 1
        load('../new_data/sim/s303_Mueller');
        dim = 292:0.1:312;
    elseif i_sample == 2
        load('../new_data/sim/s322_Mueller');
        dim = 312:0.1:332;
    elseif i_sample == 3
        load('../new_data/sim/s1000_Mueller');
        dim = 1022:0.1:1042;
    end
    n_dim = size(dim,2);
    e_m   = zeros(n_dim,1);

    M = zeros(4,4,n_wave,n_inc);     % measured data
    for i_inc = 1:n_inc
        M(:,:,:,i_inc) = find_M1(i_sample,i_inc);
    end
    M_reshape = M(:,:,diff_l:diff_u,:);
    M_reshape = reshape(M_reshape,[4*4*n_diff*n_inc,1]);
    n_y       = size(M_reshape,1);

    Mueller_dim = zeros(4*4*n_diff*n_inc,1);     % simulated data
    for i_dim = 1:n_dim
```

```
36          t = squeeze(Mueller(:,:,diff_l:diff_u,i_dim,1,1,1,1,:));
37          Mueller_dim(:,i_dim) = reshape(t,[4*4*n_diff*n_inc,1]);
38      end
39
40      for i_dim = 1:n_dim
41          diff = M_reshape-squeeze(Mueller_dim(:,i_dim));
42          w = zeros(n_y,1);
43          % calculate derivative for each signature
44          for i_y = 1:n_y
45              if i_dim == 1
46                  w(i_y) = Mueller_dim(i_y,i_dim+1) - ...
                        Mueller_dim(i_y,i_dim);
47              elseif i_dim == n_dim
48                  w(i_y) = Mueller_dim(i_y,i_dim) - ...
                        Mueller_dim(i_y,i_dim-1);
49              else
50                  w(i_y) = (Mueller_dim(i_y,i_dim+1) - ...
                        Mueller_dim(i_y,i_dim-1))/2;
51              end
52          end
53          w = abs(w);         % weighted
54          w = ones(n_y,1);    % averaged
55
56          % t = sqrt(diff.^2).*w;
57          % e1 = mean(t);         % MAE
58          % t = mean(diff.^2.*w);
59          % e1 = sqrt(t);         % RMSE
60          % e1 = mean(diff.^2.*w);% MSE
61          e_m(i_dim) = e1;
62      end
63      [a b] = min(e_m);
64      disp(dim(b))
65      figure()
66      plot(dim,e_m)
67
68  end
```

Listing D.6: Verdet constant calibration

```
1  clear all; close all; clc;
2  restoredefaultpath;
3
4  % choose experiment
5  exper = '../FR_data/Verdet_H';   % two solenoids result
6  addpath(genpath(exper))
7  addpath('../param_data')
8
9  P        = load_P(exper);
10 [c v]    = load_cv(exper);        % the current and voltage
11 n_c      = size(c,2);             % number of calibration points
12
13 Iind     = load_Iind(exper);      % interested wavelength index
14 n_Iind   = size(Iind,1);          % number of interested wavelengths
15 [I_back I0 Ia] = load_preI(exper,Iind);  % background, I0, 0deg ...
       analyzer
16 I0 = I0-I_back;
17
18 files = load_files(exper);
19 n_file = size(files,2);
20 I = zeros(n_Iind,n_file); % find all the light intensities minus ...
       background
21 for i_file = 1:n_file
22     file_name = strcat(files{i_file},'.mat');
23     load(file_name);
24     I_temp = mean(maya_data);
25     I_temp = I_temp(Iind);
26     I_temp = I_temp' - I_back;
27     I(:,i_file) = I_temp;
28 end
29 I = I(:,1:end);
30
31 % calculate the Verdet constant at each wavelength
32 theta = zeros(n_Iind,n_c);   % Faraday rotation angles
33 Verdet = zeros(n_Iind,1);    % Verdet constant
```

```
34 f = zeros(n_Iind,2);
35 Rsq = zeros(n_Iind,1);
36 for i_Iind = 1:n_Iind
37     theta(i_Iind,:) = acos(sqrt( I(i_Iind,:)./I0(i_Iind) ));
38     theta(i_Iind,:) = rad2deg(theta(i_Iind,:));
39     x = c;
40     y = theta(i_Iind,:);
41     f_temp = polyfit(x,y,1);
42         y_fit = f_temp(1)*x+f_temp(2);
43         SStot = sum((y-mean(y)).^2);
44         SSres = sum((y-y_fit).^2);
45     Rsq(i_Iind,:) = 1-SSres/SStot;
46     f(i_Iind,:) = f_temp';
47     Verdet(i_Iind) = f_temp(1)/P;
48 end
49 
50 % plot the Verdet callibration curve at four wavelengths
51 plot_ind = 600:250:1600;
52 fig = figure;
53 for i_plot = 1:4
54     subplot(2,2,i_plot)
55     plot(c,theta(plot_ind(i_plot),:),...
56         'x','markersize',8,'linewidth',1); hold on;
57     plot(c,f(plot_ind(i_plot),1)*c+f(plot_ind(i_plot),2),...
58         'linewidth',1.5); hold on;
59     maya_wavelen_Iind = maya_wavelen(Iind);
60     title(num2str(maya_wavelen_Iind(plot_ind(i_plot))));
61     axis([-2.1 2.1 27 70])
62     grid on;
63 end
64 subplot(2,2,1); title('476nm');
65 subplot(2,2,2); title('588nm');
66 subplot(2,2,3); title('700nm');
67 subplot(2,2,4); title('808nm');
68 legend('Experimental','Best fit line')
69 sgtitle('Verdet calibration curve at four wavelengths')
70 han=axes(fig,'visible','off');
```

```
71 han.XLabel.Visible='on';
72 xlabel(han,'Current (A)');
73 han.YLabel.Visible='on';
74 ylabel(han,'Rotation angle of polarization plane (deg)');
75
76 % plot the Verdet constant versus wavelength
77 wave_SF59 = maya_wavelen*1e-9;
78 a = 2843.2e-9;
79 b = 112.5192e-20;
80 lambda0 = 175.3e-9;
81 V_SF59 = pi./wave_SF59 .* (a+b./(wave_SF59.^2-lambda0^2));
82 figure()
83 plot(maya_wavelen(Iind), abs(Verdet), 'x', 'markersize', 3); hold on;
84 plot(wave_SF59*1e9,V_SF59,'linewidth',2); hold on;
85 scatter(650, 23, 'o', 'MarkerFaceColor', 'g')
86 legend('Experimental','From paper [1]','From paper ...
       [2]','fontsize',18)
87 xlabel('Wavelength (nm)')
88 ylabel('Verdet constant (rad/(T.m))')
89 title('Verdet constant depends on wavelength')
90 axis([450 1000 0 100])
91 grid on
```

Listing D.7: Faraday effect-enabled photometric ellipsometer codes

```
1  %% 1. Air measurement
2  restoredefaultpath;
3  addpath('../param_data');
4  load('maya_wavelen');
5  load('beta'); beta_angle = deg2rad(beta);
6  addpath(genpath('../FR_data/49_20211002/Air_rotating_H'));
7  light='H'; P=90; A_start=0;
8
9  % set motion parameters
10 n_P = size(P,2);
11 n_A = size(A_start,2);
12 n_w = size(maya_wavelen,2);
13 dt = 100/1000;
14
15 % load A, P calibration
16 A_cali = load_A_cali(light);
17 P_cali = (P+P_shift)*ones(n_w,1);
18
19 % initialize matrices
20 [I0_p_m, alpha_p_m, beta_p_m, alpha_m, beta_m] = ...
       intialize_mat(n_A,n_w);
21
22 % extract Fourier coefficients
23 for i_A = 1:n_A
24     filename = strcat('P',num2str(P),...
25         'A',num2str(A_start(i_A)),'_24s_100ms.mat');
26     load(filename);
27
28     for i_w = 1:n_w
29         omega = beta_angle(i_w)/24;
30         % calculate As from calibration, motion, and starting ...
               position
31         A_start=-rad2deg(beta_angle(i_w))/2;
32         As = calc_A_s_FR(A_cali, P_cali, A_start(i_A)); % in rad
33
```

```
34          int = maya_data(:,i_w);
35          [I0_p, alpha_p, beta_p] = hadamard_PSAr(int, omega, dt);
36          alpha_p = alpha_p/I0_p;
37          beta_p = beta_p/I0_p;
38          % account for phase angle
39          alpha = cos(2*As(i_w))*alpha_p + sin(2*As(i_w))*beta_p;
40          beta = -sin(2*As(i_w))*alpha_p + cos(2*As(i_w))*beta_p;
41
42          % log
43          I0_p_m(i_A,i_w)      = I0_p;
44          alpha_p_m(i_A,i_w)   = alpha_p;
45          beta_p_m(i_A,i_w)    = beta_p;
46          alpha_m(i_A,i_w)     = alpha;
47          beta_m(i_A,i_w)      = beta;
48      end
49  end
50
51  % calculate M11,M12,M33
52  M11 = zeros(n_P,n_w);
53  M12 = zeros(n_P,n_w);
54  M33 = zeros(n_P,n_w);
55  for i_P = 1:n_P
56      for i_w = 1:n_w
57          Ps_i = deg2rad(P(i_P)-P_cali(i_w));
58          A = [1 cos(2*Ps_i) 0;
59              cos(2*Ps_i) 1 0;
60              0 0 sin(2*Ps_i)];
61          B = [I0_p_m(i_P,i_w);
62              alpha_m(i_P,i_w)*I0_p_m(i_P,i_w);
63              beta_m(i_P,i_w)*I0_p_m(i_P,i_w)];
64          temp = linsolve(A,B);
65          M11(i_P,i_w) = temp(1);
66          M12(i_P,i_w) = temp(2);
67          M33(i_P,i_w) = temp(3);
68      end
69  end
70  M12n = M12./M11;
```

```
71 M33n = M33./M11;
72 plot_M12_M33(M12n,M33n,light,maya_wavelen)
73
74 %% 2. Thin film measurement
75 clear all; close all; clc;
76 addpath('../param_data');  load('maya_wavelen');
77 addpath(genpath('../FR_data/47_20210820/5_Film_H'));
78 light = 'H';
79 P = load('P_discrete');
80 A_start=0; A_shift=0;
81
82 % load motion parameters
83 n_P = size(P,2);
84 n_w = size(maya_wavelen,2);
85
86 % initialize matrices
87 [I0_p_m, alpha_p_m, beta_p_m, alpha_m, beta_m] = ...
       intialize_mat(n_P,n_w);
88 R_m = zeros(n_P,n_w);
89
90 % extract Fourier coefficients
91 for i_P = 1
92     filename = strcat('P',num2str(P(i_P)),'A0_100ms.mat');
93     load(filename);
94     maya_data = maya_data(3:end,:);
95
96     for i_w = 1:n_w
97         int = maya_data(:,i_w);
98         [I0_p, alpha_p, beta_p] = hadamard_PSAr(int, omega, dt);
99         alpha_p = alpha_p/I0_p;
100        beta_p = beta_p/I0_p;
101
102        % log
103        I0_p_m(i_P,i_w) = I0_p;
104        alpha_p_m(i_P,i_w) = alpha_p;
105        beta_p_m(i_P,i_w) = beta_p;
106        R_m(i_P,i_w) = 1- (alpha_p^2+beta_p^2);
```

```
107     end
108 end
109
110 f = fit2parab(P,R_m,n_w);
111 P_cali = v2angle(-f(:,2)./(2*f(:,1)),Verdet);
112 A_cali = load_A_cali(light)+a_pass;
113
114 % calculate M11,M12,M33
115 Ps = zeros(n_P,n_w);
116 M11 = zeros(n_P,n_w);
117 M12 = zeros(n_P,n_w);
118 M33 = zeros(n_P,n_w);
119
120 for i_P = 1:n_P
121     % calculate As from calibration, motion, and starting position
122     As = calc_A_s(omega, acc, A_cali, P_cali, A_start, A_shift); ...
            % in rad
123
124     for i_w = 1:n_w
125         alpha = cos(2*As(i_w))*alpha_p_m(i_P,i_w) + ...
126             sin(2*As(i_w))*beta_p_m(i_P,i_w);
127         beta = -sin(2*As(i_w))*alpha_p_m(i_P,i_w) + ...
128             cos(2*As(i_w))*beta_p_m(i_P,i_w);
129
130         Ps_i = deg2rad(P(i_P)-P_cali(i_w));
131         A = [1 cos(2*Ps_i) 0;
132             cos(2*Ps_i) 1 0;
133             0 0 sin(2*Ps_i)];
134         B = [I0_p_m(i_P,i_w);
135             alpha*I0_p_m(i_P,i_w);
136             beta*I0_p_m(i_P,i_w)];
137         temp = linsolve(A,B);
138
139         alpha_m(i_P,i_w) = alpha;
140         beta_m(i_P,i_w) = beta;
141         Ps(i_P,i_w) = Ps_i;
142         M11(i_P,i_w) = temp(1);
```

```
143         M12(i_P,i_w) = temp(2);
144         M33(i_P,i_w) = temp(3);
145     end
146 end
147 plot_M12_M33(M12./M11,M33./M11,light,maya_wavelen)
148 subplot(2,1,1)
149 hold on;
150 plot(maya_wavelen,squeeze(TF_Mueller_o(1,2,:,4)), 'r--', ...
        'linewidth',1.5);
151 axis([450 950 -1 1])
152 subplot(2,1,2)
153 hold on;
154 plot(maya_wavelen,squeeze(TF_Mueller_o(3,3,:,4)), 'r--', ...
        'linewidth',1.5);
155 axis([450 950 -1 1])
```

Nomenclature

$2N$	Maximum harmonic order
$2n$	Harmonic order
α_2	Fourier coefficient
α_{2n}	Fourier coefficient associated with order $2n$
$\bar{n}$	Averaged refractive index of right-handed and left-handed polarized light
β	Rotation angle of the polarization plane
$\beta(\lambda)$	Rotation angle of the polarization plane at wavelength λ
β_2	Fourier coefficient
β_{2n}	Fourier coefficient associated with order $2n$
$\mathbf{\Phi}$	Coefficient matrix associated with the integrated intensities
$\boldsymbol{\theta}$	Vector consisting of the DC term and the Fourier coefficients
$\boldsymbol{\phi}_k$	Coefficient vector associated with the k_{th} integrated intensity
$\Delta\mathbf{S}$	The noise of the integrated intensity, a K by 1 vector
$\Delta\theta$	Rotation angle of the polarization plane
Δn	Difference between n_+ and n_-
Δt	Integration duration

η	Angle between TZ and the z-axis
γ	Empirical constant
γ_1	The first-order coefficient of integrated light intensity variance to mean
γ_2	The offset of integrated light intensity variance to mean
$\hat{\boldsymbol{\theta}}$	The estimated value of $\boldsymbol{\theta}$
$\hat{\mathbf{x}}$	Reconstructed dimensions, a n_x by 1 vector
$\hat{S}_k$	The expected k_{th} integrated intensity
λ	Wavelength of incident light
$\mathbf{A}$	Coefficient matrix transforming $\mathbf{S}$ to $\mathbf{M}^u$, a K by 16 matrix
$\mathbf{A}_1$	The first row of $\mathbf{A}$, a K by 1 vector
$\mathbf{A}_k$	The k_{th} row of $\mathbf{A}$, a K by 1 vector
$\mathbf{B}$	Coefficient matrix associated with the vector of the Fourier coefficients
$\mathbf{f}(\mathbf{x})$	Simulated signature, a m by 1 vector
$\mathbf{H}$	Hessian matrix
$\mathbf{M}$	Normalized Mueller matrix
$\mathbf{M}^u$	Unnormalized Mueller matrix, reshaped to a 16 by 1 column vector
$\mathbf{M}_A$	Mueller matrix of the analyzer
$\mathbf{M}_n$	Normalized Mueller matrix elements, reshaped to a 16 by 1 column vector
$\mathbf{M}_P$	Mueller matrix of the polarizer
$\mathbf{M}_S$	Mueller matrix of the sample
$\mathbf{M}_{FR_1}$	Mueller matrix of the first Mueller matrix

$\mathbf{M}_{FR_2}$	Mueller matrix of the second Mueller matrix
$\mathbf{R}(-P_s)$	Rotation Mueller matrix associated with $-P_s$
$\mathbf{R}(A_s)$	Rotation Mueller matrix associated with A_s
$\mathbf{S}$	Integrated intensity vector, a K by 1 vector
$\mathbf{S}_i$	Input Stokes vector
$\mathbf{S}_n$	Noisy integrated intensities, a K by 1 vector
$\mathbf{S}_o$	Exit Stokes vector
$\mathbf{u}$, $\mathbf{v}$	Orthogonal unit vectors
$\mathbf{u}_n$, $\mathbf{v}_n$	New orthogonal unit vectors
$\mathbf{W}$	Weight matrix, an m by m matrix
$\mathbf{x}$	Dimensions, a n_x by 1 vector
$\mathbf{x}_n$	Nominal dimensions, a n_x by 1 vector
$\mathbf{y}$	Measured signature, an m by 1 vector
$\mathcal{N}$	Normal distribution
μ_0	Vacuum permeability
μ_e	Mean of the normalized Mueller matrix element error
μ_k	Slack variable
μ_{Q_D}	Mean of Q_D
μ_{Q_N}	Mean of Q_N
Ω	Dimensions' domain
ω	The rotating components' fundamental frequency

ω_l	Light frequency
ϕ	The angle between the polarizer and the analyzer transmission axes
ψ, Δ	Ellipsometric parameters
σ	Standard deviation of fitting error
$\sigma^2_{M^n_k}$	Variance of the approximated Gaussian distribution of a normalized Mueller matrix element
$\sigma^2_{Q_D}$	Variance of Q_D
$\sigma^2_{Q_N}$	Variance of Q_N
σ^2_e	Variance of the normalized Mueller matrix element error
σ^2_k	The variance associated with the k_{th} integrated light intensity
A_s	Azimuthal offset of the analyzer
A_{1i}	The element of $\mathbf{A}$ in the first row and i_{th} column
A_{ki}	The element of $\mathbf{A}$ in the k_{th} row and i_{th} column
A_{kj}	The element of $\mathbf{A}$ in the k_{th} row and j_{th} column
B	Magnetic flux density
B_z	Magnetic field generated by a single loop along the z-direction
c	Light speed
D	Parameter of the solenoid and the material
d_i	Inner diameter of the glass holder
d_o	Outer diameter of the glass holder
d_w	Diameter of electrical wire
dB_z	Magnetic field generated by the infinitesimal segment along the z-axis

dl	Length of the infinitesimal loop segment
e	Electron charge
$E[M_k^n]$	Mean of the approximated Gaussian distribution of a normalized Mueller matrix element
E_+	Electric field of the right-handed polarized light
E_-	Electric field of the left-handed polarized light
E_{in}	Electric field of the light beam before a Faraday rotator
E_{out}	Electric field of the light beam exiting a Faraday rotator
f	Objective function
$f_i(\mathbf{x})$	The i_{th} simulated signature
G	Electrical wire gauge
g_k	Constraint function
H_{ij}	Element of H in the i_{th} row and j_{th} column
$I(t)$	Light intensity exiting the light path at time t
I_c	Current through the solenoid
i_c	Index of the solenoid loop per layer
I_l	Light intensity transmitted through the analyzer
i_l	Index of the solenoid layer
I_o	DC term of the light intensity
I_{lo}	Intensity of linearly polarized light incident on the analyzer
J	Constant
L	Length of holder

L_m	Length of the optically active medium (glass rod) length
L_w	Total length of electrical wire
m	Length of the signature vector
m_1	Amplitude of right-handed polarized light
M_1^u	The first element in $\mathbf{M}^u$
m_2	Amplitude of left-handed polarized light
m_e	Electron mass
M_k^u	The k_{th} element in $\mathbf{M}^u$
M_{12}	Element of normalized Mueller matrix in the first row and second column
M_{33}	Element of normalized Mueller matrix in the third row and third column
n	Refractive index
n_+	Refractive index of right-handed polarized light
n_-	Refractive index of left-handed polarized light
n_c	Number of loops per layer in the Faraday rotator
n_l	Number of coil layers
n_x	Length of the dimension vector
O	Coordinate origin
p	Likelihood function of all integrated intensities taking on the observed values
$P(S_k^n)$	Probability of the k_{th} intensity taking on the observed value
P_a	Polarizer angle
P_s	Azimuthal offset of the polarizer

Q_D	The denominator of the normalized Mueller matrix elements
Q_N	The numerator of the normalized Mueller matrix elements
R	Resistance per unit length
R^2	Coefficient of determination
R_p	Length of TZ
r_{i_l}	Radius of the loop in layer i_l
S_k	k_{th} integrated light intensity
T	Point on the z-axis
t	Time
t_1	Starting time of the integration period
t_2	Ending time of the integration period
V	Verdet constant
$V(\lambda)$	Verdet constant as function of wavelength
W	Wire weight
w	wire weight per unit length
w_i	The element of $\mathbf{W}$ in the i_{th} row and i_{th} column
Z	Point on the infinitesimal segment
z	Light's propagation direction
z_{i_c}	Longitudinal position of the loop i_c

Bibliography

[1] Anysilicon. (2021) Semiconductor technology node history and roadmap. [Online]. Available: https://anysilicon.com/semiconductor-technology-node-history-roadmap/

[2] Forbes. (2018) The u.s. already has bleeding edge technology manufacturing with globalfoundries fab 8 in malta, ny. [Online]. Available: https://www.forbes.com/sites/patrickmoorhead/2018/02/04/the-u-s-already-has-bleeding-edge-technology-manufacturing-with-\\globalfoundries-fab-8-in-malta-ny/?sh=23ad37fb23af

[3] Screen. (2021) Semiconductor manufacturing processe. [Online]. Available: https://www.screen.co.jp/spe/en/process

[4] I. S. Bozchalooi, A. C. Houck, J. AlGhamdi, and K. Youcef-Toumi, "Design and control of multi-actuated atomic force microscope for large-range and high-speed imaging," *Ultramicroscopy*, vol. 160, pp. 213–224, 2016.

[5] C. Yang, J. Yan, M. Dukic, N. Hosseini, J. Zhao, and G. E. Fantner, "Design of a high-bandwidth tripod scanner for high speed atomic force microscopy," *Scanning*, vol. 38, no. 6, pp. 889–900, 2016.

[6] C. Yang, R. Winkler, M. Dukic, J. Zhao, H. Plank, and G. E. Fantner, "Probing the morphology and evolving dynamics of 3d printed nanostructures using high-speed atomic force microscopy," *ACS applied materials & interfaces*, vol. 9, no. 29, pp. 24 456–24 461, 2017.

[7] J. D. Adams, A. Nievergelt, B. W. Erickson, C. Yang, M. Dukic, and G. E. Fantner, "High-speed imaging upgrade for a standard sample scanning atomic force microscope using small cantilevers," *Review of Scientific Instruments*, vol. 85, no. 9, p. 093702, 2014.

[8] J. I. Goldstein, D. E. Newbury, J. R. Michael, N. W. Ritchie, J. H. J. Scott, and D. C. Joy, *Scanning electron microscopy and X-ray microanalysis.* Springer, 2017.

[9] K. Vernon-Parry, "Scanning electron microscopy: an introduction," *III-Vs Review*, vol. 13, no. 4, pp. 40–44, 2000.

[10] M. Hayat, *Basic techniques for transmission electron microscopy.* Elsevier, 2012.

[11] E. Ruska, "Past and present attempts to attain the resolution limit of the transmission electron microscope," in *Advances in Imaging and Electron Physics*. Elsevier, 2017, vol. 200, pp. 1–59.

[12] Y. H. Lo, L. Zhao, M. Gallagher-Jones, A. Rana, J. J. Lodico, W. Xiao, B. Regan, and J. Miao, "In situ coherent diffractive imaging," *Nature communications*, vol. 9, no. 1, pp. 1–10, 2018.

[13] M. J. Cherukara, R. Pokharel, T. S. O'Leary, J. K. Baldwin, E. Maxey, W. Cha, J. Maser, R. J. Harder, S. J. Fensin, and R. L. Sandberg, "Three-dimensional x-ray diffraction imaging of dislocations in polycrystalline metals under tensile loading," *Nature communications*, vol. 9, no. 1, pp. 1–6, 2018.

[14] P. Gao, B. Prunsche, L. Zhou, K. Nienhaus, and G. U. Nienhaus, "Background suppression in fluorescence nanoscopy with stimulated emission double depletion," *Nature Photonics*, vol. 11, no. 3, p. 163, 2017.

[15] G. Vicidomini, P. Bianchini, and A. Diaspro, "Sted super-resolved microscopy," *Nature methods*, vol. 15, no. 3, pp. 173–182, 2018.

[16] H. Shroff, H. White, and E. Betzig, "Photoactivated localization microscopy (palm) of adhesion complexes," *Current protocols in cell biology*, vol. 58, no. 1, pp. 4–21, 2013.

[17] H. Zhong, "Photoactivated localization microscopy (palm): an optical technique for achieving˜ 10-nm resolution," *Cold Spring Harbor protocols*, vol. 2010, no. 12, pp. pdb–top91, 2010.

[18] W. Gao, S. Goto, K. Hosobuchi, S. Ito, and Y. Shimizu, "A noncontact scanning electrostatic force microscope for surface profile measurement," *CIRP annals*, vol. 61, no. 1, pp. 471–474, 2012.

[19] K. Hosobuchi, E. Oertel, and E. Manske, "Metrological investigation of a scanning electrostatic force microscope on a nano-positioning and nano-measuring machine," *Measurement Science and Technology*, 2021.

[20] M. G. Gustafsson, "Surpassing the lateral resolution limit by a factor of two using structured illumination microscopy," *Journal of microscopy*, vol. 198, no. 2, pp. 82–87, 2000.

[21] L. Schermelleh, P. M. Carlton, S. Haase, L. Shao, L. Winoto, P. Kner, B. Burke, M. C. Cardoso, D. A. Agard, M. G. Gustafsson *et al.*, "Subdiffraction multicolor imaging of the nuclear periphery with 3d structured illumination microscopy," *Science*, vol. 320, no. 5881, pp. 1332–1336, 2008.

[22] F. Wang, L. Liu, P. Yu, Z. Liu, H. Yu, Y. Wang, and W. J. Li, "Three-dimensional super-resolution morphology by near-field assisted white-light interferometry," *Scientific reports*, vol. 6, p. 24703, 2016.

[23] T. Taubner, D. Korobkin, Y. Urzhumov, G. Shvets, and R. Hillenbrand, "Near-field microscopy through a sic superlens," *Science*, vol. 313, no. 5793, pp. 1595–1595, 2006.

[24] Y. Yan, L. Li, C. Feng, W. Guo, S. Lee, and M. Hong, "Microsphere-coupled scanning laser confocal nanoscope for sub-diffraction-limited imaging at 25 nm lateral resolution in the visible spectrum," *Acs Nano*, vol. 8, no. 2, pp. 1809–1816, 2014.

[25] D. Lu and Z. Liu, "Hyperlenses and metalenses for far-field super-resolution imaging," *Nature communications*, vol. 3, no. 1, pp. 1–9, 2012.

[26] Z. Jacob, L. V. Alekseyev, and E. Narimanov, "Optical hyperlens: far-field imaging beyond the diffraction limit," *Optics express*, vol. 14, no. 18, pp. 8247–8256, 2006.

[27] Z. Liu, H. Lee, Y. Xiong, C. Sun, and X. Zhang, "Far-field optical hyperlens magnifying sub-diffraction-limited objects," *science*, vol. 315, no. 5819, pp. 1686–1686, 2007.

[28] C. Raymond, "Overview of scatterometry applications in high volume silicon manufacturing," in *AIP Conference Proceedings*, vol. 788, no. 1. American Institute of Physics, 2005, pp. 394–402.

[29] S. Liu, X. Chen, and C. Zhang, "Development of a broadband mueller matrix ellipsometer as a powerful tool for nanostructure metrology," *Thin Solid Films*, vol. 584, pp. 176–185, 2015.

[30] L. Jin, T. Tanaka, E. Kondoh, B. Gelloz, and M. Uehara, "Extracting calibrated parameters from imaging ellipsometric measurement," *Japanese Journal of Applied Physics*, vol. 56, no. 11, p. 116602, 2017.

[31] H. Chouaib and Q. Zhao, "Nanoscale optical critical dimension measurement of a contact hole using deep ultraviolet spectroscopic ellipsometry," *Journal of Vacuum Science & Technology B, Nanotechnology and Microelectronics: Materials, Processing, Measurement, and Phenomena*, vol. 31, no. 1, p. 011803, 2013.

[32] G. R. Muthinti, B. L. Peterson, R. K. Bonam, and A. C. Diebold, "Characterization of e-beam patterned grating structures using mueller matrix based scatterometry," *Journal of Micro/Nanolithography, MEMS, and MOEMS*, vol. 12, no. 1, p. 013018, 2013.

[33] H.-T. Huang and F. L. Terry Jr, "Spectroscopic ellipsometry and reflectometry from gratings (scatterometry) for critical dimension measurement and in situ, real-time process monitoring," *Thin Solid Films*, vol. 455, pp. 828–836, 2004.

[34] J. Lee, J. Koh, and R. Collins, "Multichannel mueller matrix ellipsometer for real-time spectroscopy of anisotropic surfaces and films," *Optics letters*, vol. 25, no. 21, pp. 1573–1575, 2000.

[35] ——, "Dual rotating-compensator multichannel ellipsometer: Instrument development for high-speed mueller matrix spectroscopy of surfaces and thin films," *Review of Scientific Instruments*, vol. 72, no. 3, pp. 1742–1754, 2001.

[36] C.-W. Kuo, C.-Y. Han, J.-Y. Jhou, and Z.-Y. Peng, "Using a fast dual-wavelength imaging ellipsometric system to measure the flow thickness profile of an oil thin film," *Applied Surface Science*, vol. 421, pp. 465–470, 2017.

[37] Z. F. Yu, C. W. Pirnstill, and G. L. Coté, "Dual-modulation, dual-wavelength, optical polarimetry system for glucose monitoring," *Journal of Biomedical Optics*, vol. 21, no. 8, p. 087001, 2016.

[38] G. W. Kattawar and M. J. Raković, "Virtues of mueller matrix imaging for underwater target detection," *Applied optics*, vol. 38, no. 30, pp. 6431–6438, 1999.

[39] G. W. Kattawar and D. J. Gray, "Mueller matrix imaging of targets in turbid media: effect of the volume scattering function," *Applied optics*, vol. 42, no. 36, pp. 7225–7230, 2003.

[40] P.-W. Zhai, G. W. Kattawar, and P. Yang, "Mueller matrix imaging of targets under an air-sea interface," *Applied optics*, vol. 48, no. 2, pp. 250–260, 2009.

[41] F. Iglesias, A. Feller, K. Nagaraju, and S. Solanki, "High-resolution, high-sensitivity, ground-based solar spectropolarimetry with a new fast imaging polarimeter-i. prototype characterization," *Astronomy & Astrophysics*, vol. 590, p. A89, 2016.

[42] A. Berdyugin, V. Piirola, and J. Poutanen, "Optical polarimetry: Methods, instruments and calibration techniques," in *Astronomical Polarisation from the Infrared to Gamma Rays.* Springer, 2019, pp. 33–65.

[43] L. Broch, A. E. Naciri, and L. Johann, "Systematic errors for a mueller matrix dual rotating compensator ellipsometer," *Optics express*, vol. 16, no. 12, pp. 8814–8824, 2008.

[44] D. H. Kim, Y. H. Yun, and K.-N. Joo, "Sparse (spatially phase-retarded spectroscopic ellipsometry) for real-time film analysis," *Optics letters*, vol. 42, no. 16, pp. 3189–3192, 2017.

[45] H. Tompkins and E. A. Irene, *Handbook of ellipsometry.* William Andrew, 2005.

[46] E. Garcia-Caurel, A. De Martino, J.-P. Gaston, and L. Yan, "Application of spectroscopic ellipsometry and mueller ellipsometry to optical characterization," *Applied spectroscopy*, vol. 67, no. 1, pp. 1–21, 2013.

[47] L. Augel, I. Fischer, F. Hornung, M. Dressel, A. Berrier, M. Oehme, and J. Schulze, "Ellipsometric characterization of doped ge 0.95 sn 0.05 films in the infrared range for plasmonic applications," *Optics letters*, vol. 41, no. 18, pp. 4398–4400, 2016.

[48] R. Synowicki, C. M. Herzinger, J. T. Hall, and A. Malingowski, “Optical constants of electroplated gold from spectroscopic ellipsometry,” *Applied Surface Science*, vol. 421, pp. 824–830, 2017.

[49] G. Jayaswal, Z. Dai, X. Zhang, M. Bagnarol, A. Martucci, and M. Merano, “Measurement of the surface susceptibility and the surface conductivity of atomically thin mos 2 by spectroscopic ellipsometry,” *Optics letters*, vol. 43, no. 4, pp. 703–706, 2018.

[50] W. Zhou, Y. Liu, Y. Yin, W. Ma, and Z. Huang, “Investigation on the optical properties of annealed mn-co-ni-o thin films by spectroscopic ellipsometry,” *Optics Letters*, vol. 44, no. 11, pp. 2701–2704, 2019.

[51] J. Dilts, C. Hong, A. Siahmakoun, M. Syed, and H. Alisafaee, “Low-mse extraction of permittivity in optical hyperbolic metamaterials,” *Optics letters*, vol. 44, no. 17, pp. 4303–4306, 2019.

[52] N. G. Orji, M. Badaroglu, B. M. Barnes, C. Beitia, B. D. Bunday, U. Celano, R. J. Kline, M. Neisser, Y. Obeng, and A. Vladar, “Metrology for the next generation of semiconductor devices,” *Nature electronics*, vol. 1, no. 10, pp. 532–547, 2018.

[53] C. Wang, X. Chen, H. Gu, H. Jiang, C. Zhang, and S. Liu, “On the limits of low-numerical-aperture imaging scatterometry,” *Optics express*, vol. 28, no. 6, pp. 8445–8462, 2020.

[54] D. Aspnes, “Spectroscopic ellipsometry-past, present, and future,” *Thin Solid Films*, vol. 571, pp. 334–344, 2014.

[55] A. B. Bulykina, V. A. Ryzhova, and V. V. Korotaev, “In vivo skin surface study by scattered ellipsometry method,” in *Optical Methods for Inspection, Characterization, and Imaging of Biomaterials IV*, vol. 11060. International Society for Optics and Photonics, 2019, p. 110601F.

[56] H. Liu, W. Liu, and G. Jin, “Detection of exosomes using total internal reflected imaging ellipsometry,” *Biosensors*, vol. 11, no. 5, p. 164, 2021.

[57] B. Fodor, P. Kozma, S. Burger, M. Fried, and P. Petrik, “Effective medium approximation of ellipsometric response from random surface roughness simulated by finite-element method,” *Thin Solid Films*, vol. 617, pp. 20–24, 2016.

[58] C. Negara, T. Längle, and J. Beyerer, “Imaging ellipsometry for curved surfaces,” *Journal of Vacuum Science & Technology B, Nanotechnology and Microelectronics: Materials, Processing, Measurement, and Phenomena*, vol. 38, no. 1, p. 014016, 2020.

[59] Y. Hayashi, M. Kawano, A. Sanpei, and S. Masuzaki, “Mie-scattering ellipsometry system for analysis of dust formation process in large plasma device,” *IEEE Transactions on Plasma Science*, vol. 44, no. 6, pp. 1032–1035, 2016.

[60] P. Friš and A. Dubroka, “Vacuum variable-angle far-infrared ellipsometer,” *Applied Surface Science*, vol. 421, pp. 430–434, 2017.

[61] A. Ebner, R. Zimmerleiter, C. Cobet, K. Hingerl, M. Brandstetter, and J. Kilgus, “Sub-second quantum cascade laser based infrared spectroscopic ellipsometry,” *Optics letters*, vol. 44, no. 14, pp. 3426–3429, 2019.

[62] Z. Fan, Y. Tang, K. Wei, and Y. Zhang, “Calibration of focusing lens artifacts in a dual rotating-compensator mueller matrix ellipsometer,” *Applied optics*, vol. 57, no. 15, pp. 4145–4152, 2018.

[63] R. H. Muller and J. C. Farmer, “Fast, self-compensating spectral-scanning ellipsometer,” *Review of scientific instruments*, vol. 55, no. 3, pp. 371–374, 1984.

[64] H. Mathieu, D. McClure, and R. Muller, “Fast self-compensating ellipsometer,” *Review of Scientific Instruments*, vol. 45, no. 6, pp. 798–802, 1974.

[65] J. C. Farmer and R. H. Muller, “Effect of rhodamine-b on the electrodeposition of lead on copper,” *Journal of the Electrochemical Society*, vol. 132, no. 2, p. 313, 1985.

[66] S. T. Mayer and R. H. Muller, “Nucleation of silver (i) oxide investigated by spectroscopic ellipsometry,” *Journal of the Electrochemical Society*, vol. 135, no. 9, p. 2133, 1988.

[67] J. Lee, P. I. Rovira, I. An, and R. Collins, “Rotating-compensator multichannel ellipsometry: Applications for real time stokes vector spectroscopy of thin film growth,” *Review of scientific instruments*, vol. 69, no. 4, pp. 1800–1810, 1998.

[68] D. Aspnes, “Photometric ellipsometer for measuring partially polarized light,” *JOSA*, vol. 65, no. 11, pp. 1274–1278, 1975.

[69] J. M. Bueno, “Polarimetry using liquid-crystal variable retarders: theory and calibration,” *Journal of Optics A: Pure and Applied Optics*, vol. 2, no. 3, p. 216, 2000.

[70] N. J. Pust and J. A. Shaw, “Dual-field imaging polarimeter using liquid crystal variable retarders,” *Applied Optics*, vol. 45, no. 22, pp. 5470–5478, 2006.

[71] A. De Martino, Y.-K. Kim, E. Garcia-Caurel, B. Laude, and B. Drévillon, “Optimized mueller polarimeter with liquid crystals,” *Optics letters*, vol. 28, no. 8, pp. 616–618, 2003.

[72] B. Laude-Boulesteix, A. De Martino, B. Drévillon, and L. Schwartz, “Mueller polarimetric imaging system with liquid crystals,” *Applied optics*, vol. 43, no. 14, pp. 2824–2832, 2004.

[73] E. Garcia-Caurel, A. De Martino, and B. Drevillon, “Spectroscopic mueller polarimeter based on liquid crystal devices,” *Thin Solid Films*, vol. 455, pp. 120–123, 2004.

[74] J. Ladstein, F. Stabo-Eeg, E. Garcia-Caurel, and M. Kildemo, "Fast near-infrared spectroscopic mueller matrix ellipsometer based on ferroelectric liquid crystal retarders," *physica status solidi c*, vol. 5, no. 5, pp. 1097–1100, 2008.

[75] L. M. S. Aas, D. G. Skåre, P. G. Ellingsen, P. A. Letnes, and M. Kildemo, "Design, optimization and realization of a ferroelectric liquid crystal based mueller matrix ellipsometer using a genetic algorithm," *Thin solid films*, vol. 571, pp. 522–526, 2014.

[76] P. A. Letnes, I. S. Nerbø, L. M. S. Aas, P. G. Ellingsen, and M. Kildemo, "Fast and optimal broad-band stokes/mueller polarimeter design by the use of a genetic algorithm," *Optics express*, vol. 18, no. 22, pp. 23 095–23 103, 2010.

[77] X. Chen, S. Liu, H. Gu, and C. Zhang, "Formulation of error propagation and estimation in grating reconstruction by a dual-rotating compensator mueller matrix polarimeter," *Thin Solid Films*, vol. 571, pp. 653–659, 2014.

[78] Y. J. Cho, W. Chegal, J. P. Lee, and H. M. Cho, "Universal evaluations and expressions of measuring uncertainty for rotating-element spectroscopic ellipsometers," *Optics express*, vol. 23, no. 12, pp. 16 481–16 491, 2015.

[79] Y. J. Cho, W. Chegal, and H. M. Cho, "Fourier analysis for rotating-element ellipsometers," *Optics letters*, vol. 36, no. 2, pp. 118–120, 2011.

[80] R. Collins and J. Koh, "Dual rotating-compensator multichannel ellipsometer: instrument design for real-time mueller matrix spectroscopy of surfaces and films," *JOSA A*, vol. 16, no. 8, pp. 1997–2006, 1999.

[81] E. A. Irene and H. G. Tompkins, *Handbook of ellipsometry.* William Andrew Pub., 2005.

[82] L. Jin, Y. Iizuka, T. Iwao, E. Kondoh, M. Uehara, and B. Gelloz, "Calibration of the retardation inhomogeneity for the compensator-rotating imaging ellipsometer," *Applied Optics*, vol. 58, no. 33, pp. 9224–9229, 2019.

[83] M. Khazimullin and Y. A. Lebedev, "Fourier transform approach in modulation technique of experimental measurements," *Review of Scientific Instruments*, vol. 81, no. 4, p. 043110, 2010.

[84] T. M. El-Agez and S. A. Taya, "A fourier ellipsometer using rotating polarizer and analyzer at a speed ratio 1: 1," *Journal of Sensors*, vol. 2010, 2010.

[85] C. Chen, I. An, G. Ferreira, N. Podraza, J. Zapien, and R. Collins, "Multichannel mueller matrix ellipsometer based on the dual rotating compensator principle," *Thin Solid Films*, vol. 455, pp. 14–23, 2004.

[86] O. Arteaga, M. Baldrís, J. Antó, A. Canillas, E. Pascual, and E. Bertran, "Mueller matrix microscope with a dual continuous rotating compensator setup and digital demodulation," *Applied optics*, vol. 53, no. 10, pp. 2236–2245, 2014.

[87] C. Li, S. Chen, and Y. Zhu, “Maximum likelihood estimation of optical path length in spectral interferometry,” *Journal of Lightwave Technology*, vol. 35, no. 22, pp. 4880–4887, 2017.

[88] C. DeForest, “Noise-gating to clean astrophysical image data,” *The Astrophysical Journal*, vol. 838, no. 2, p. 155, 2017.

[89] D. Li, C. Sun, J. Yang, H. Liu, J. Peng, and L. Zhang, “Robust multi-frame adaptive optics image restoration algorithm using maximum likelihood estimation with poisson statistics,” *Sensors*, vol. 17, no. 4, p. 785, 2017.

[90] X. Li, H. Hu, H. Wang, and T. Liu, “Optimal measurement matrix of partial polarimeter for measuring ellipsometric parameters with eight intensity measurements,” *IEEE Access*, vol. 7, pp. 31 494–31 500, 2019.

[91] X. Li, H. Hu, L. Wu, and T. Liu, “Optimization of instrument matrix for mueller matrix ellipsometry based on partial elements analysis of the mueller matrix,” *Optics express*, vol. 25, no. 16, pp. 18 872–18 884, 2017.

[92] X. Li, F. Goudail, H. Hu, Q. Han, Z. Cheng, and T. Liu, “Optimal ellipsometric parameter measurement strategies based on four intensity measurements in presence of additive gaussian and poisson noise,” *Optics express*, vol. 26, no. 26, pp. 34 529–34 546, 2018.

[93] N. Quan, C. Zhang, and T. Mu, “Optimal configuration of partial mueller matrix polarimeter for measuring the ellipsometric parameters in the presence of poisson shot noise and gaussian noise,” *Photonics and Nanostructures-Fundamentals and Applications*, vol. 29, pp. 30–35, 2018.

[94] K. Meng, B. Jiang, C. D. Samolis, M. Alrished, and K. Youcef-Toumi, “Unevenly spaced continuous measurement approach for dual rotating–retarder mueller matrix ellipsometry,” *Optics express*, vol. 27, no. 10, pp. 14 736–14 753, 2019.

[95] X. Chen, S. Liu, C. Zhang, and J. Zhu, “Improved measurement accuracy in optical scatterometry using fitting error interpolation based library search,” *Measurement*, vol. 46, no. 8, pp. 2638–2646, 2013.

[96] X. Chen, S. Liu, C. Zhang, and H. Jiang, “Improved measurement accuracy in optical scatterometry using correction-based library search,” *Applied optics*, vol. 52, no. 27, pp. 6726–6734, 2013.

[97] J. Zhu, H. Jiang, Y. Shi, X. Chen, C. Zhang, and S. Liu, “Improved nanostructure reconstruction by performing data refinement in optical scatterometry,” *Journal of Optics*, vol. 18, no. 1, p. 015605, 2015.

[98] J. Zhu, H. Jiang, C. Zhang, X. Chen, and S. Liu, “Data refinement for robust solution to the inverse problem in optical scatterometry,” in *Metrology, Inspection, and Process Control for Microlithography XXIX*, vol. 9424. International Society for Optics and Photonics, 2015, p. 94240Y.

[99] J. Zhu, H. Jiang, Y. Shi, C. Zhang, X. Chen, and S. Liu, "Fast and accurate solution of inverse problem in optical scatterometry using heuristic search and robust correction," *Journal of Vacuum Science & Technology B, Nanotechnology and Microelectronics: Materials, Processing, Measurement, and Phenomena*, vol. 33, no. 3, p. 031807, 2015.

[100] J. Zhu, S. Liu, H. Jiang, C. Zhang, and X. Chen, "Improved deep-etched multilayer grating reconstruction by considering etching anisotropy and abnormal errors in optical scatterometry," *Optics letters*, vol. 40, no. 4, pp. 471–474, 2015.

[101] J. Zhu, S. Liu, X. Chen, C. Zhang, and H. Jiang, "Robust solution to the inverse problem in optical scatterometry," *Optics express*, vol. 22, no. 18, pp. 22 031–22 042, 2014.

[102] X. Chen, C. Zhang, and S. Liu, "Depolarization effects from nanoimprinted grating structures as measured by mueller matrix polarimetry," *Applied Physics Letters*, vol. 103, no. 15, p. 151605, 2013.

[103] L. Halagačka, K. Postava, and J. Pištora, "Analysis and modeling of depolarization effects in mueller matrix spectroscopic ellipsometry data," *Procedia Materials Science*, vol. 12, pp. 112–117, 2016.

[104] J. N. Hilfiker, J. S. Hale, C. M. Herzinger, T. Tiwald, N. Hong, S. Schöche, and H. Arwin, "Estimating depolarization with the jones matrix quality factor," *Applied Surface Science*, vol. 421, pp. 494–499, 2017.

[105] Z. Dong, X. Chen, X. Wang, Y. Shi, H. Jiang, and S. Liu, "Dependence-analysis-based data-refinement in optical scatterometry for fast nanostructure reconstruction," *Applied Sciences*, vol. 9, no. 19, p. 4091, 2019.

[106] J. Zhu, S. Liu, C. Zhang, X. Chen, and Z. Dong, "Identification and reconstruction of diffraction structures in optical scatterometry using support vector machine method," *Journal of Micro/Nanolithography, MEMS, and MOEMS*, vol. 12, no. 1, p. 013004, 2013.

[107] J. López-Téllez and N. Bruce, "Mueller-matrix polarimeter using analysis of the nonlinear voltage–retardance relationship for liquid-crystal variable retarders," *Applied Optics*, vol. 53, no. 24, pp. 5359–5366, 2014.

[108] J. Bailey, L. Kedziora-Chudczer, D. V. Cotton, K. Bott, J. Hough, and P. Lucas, "A high-sensitivity polarimeter using a ferro-electric liquid crystal modulator," *Monthly Notices of the Royal Astronomical Society*, vol. 449, no. 3, pp. 3064–3073, 2015.

[109] J. López-Téllez and N. Bruce, "Stokes polarimetry using analysis of the nonlinear voltage-retardance relationship for liquid-crystal variable retarders," *Review of Scientific Instruments*, vol. 85, no. 3, p. 033104, 2014.

[110] Thorlabs. (2021) Full-wave liquid crystal variable retarders/wave plates. [Online]. Available: https://www.thorlabs.com/newgrouppage9.cfm?objectgroup_id=6339

[111] N. C. Bruce, O. G. Rodríguez-Herrera, J. M. López-Téllez, and O. Rodríguez-Nuñez, "Experimental limits for eigenvalue calibration in liquid-crystal mueller-matrix polarimeters," *Optics Letters*, vol. 43, no. 11, pp. 2712–2715, 2018.

[112] H. O. Ltd. (2021) Faraday effect apparatus. [Online]. Available: https://www.holmarc.com/faraday_effect_multi_wavelength.php

[113] S. V. Pooja, "Measurement of verdet constant for some materials," *Global Journal of Science Frontier Research*, 2019. [Online]. Available: https://journalofscience.org/index.php/GJSFR/article/view/2505

[114] R. Serber, "The theory of the faraday effect in molecules," *Physical review*, vol. 41, no. 4, p. 489, 1932.

[115] D. W. Preston and E. R. Dietz, *The art of experimental physics.* John Wiley & Sons, 1991.

[116] Thorlabs. (2021) Optical isolators. [Online]. Available: https://www.thorlabs.com/navigation.cfm?guide_id=2015

[117] Newport. (2021) Faraday optical isolators. [Online]. Available: https://www.newport.com/c/faraday-optical-isolators

[118] Edmund. (2021) Free-space optical isolators. [Online]. Available: https://www.edmundoptics.com/f/free-space-optical-isolators/33067/

[119] E. O. Components. (2021) Optical isolators - faraday rotators. [Online]. Available: https://www.eoc-inc.com/optics-coatings/attenuators-isolators-rotators/optical-isolators-faraday-rotators/

[120] Agiltron. (2021) Optical isolators/circulators. [Online]. Available: https://agiltron.com/category/optical-isolators/

[121] E.-O. Technology. (2021) Faraday rotators & isolators. [Online]. Available: https://www.eotech.com/cart/category30/faraday-rotators-and-isolators

[122] CrystaLaser. (2021) Optical isolators - faraday isolators. [Online]. Available: http://www.crystalaser.com/new/optical-isolator.html

[123] C. O. Technology. (2021) Faraday rotator & isolator. [Online]. Available: https://csrayzer.cn/Products-Free-Space-Components.html

[124] A. Technologies. (2021) Polarization maintaining faraday mirror. [Online]. Available: http://www.afwtechnologies.com.au/sm_isolator.html

[125] M. Syed, J. Monarch, W. Li, and N. Fried, "Use of ac faraday rotation as a complementary technique in material characterization," *AIP Advances*, vol. 9, no. 12, p. 125242, 2019.

[126] C. Hu, Y. Huang, C. Deng, and T. Wang, "High sensitivity faraday effect measurement in presence of intrinsic birefringence in optical fibers," in *Advanced Sensor Systems and Applications VIII*, vol. 10821. International Society for Optics and Photonics, 2018, p. 108210U.

[127] M. Arshad, M. Shiraz Ahmad, and R. Abbas, "Measurement of verdet constant by faraday rotation," 12 2017.

[128] D. Huang, P. Pintus, S. Srinivasan, and J. E. Bowers, "Integrated compact optical current sensors with high sensitivity," in *Optical Components and Materials XIII*, vol. 9744. International Society for Optics and Photonics, 2016, p. 97440D.

[129] Q. Chen, H. Wang, Q. Wang, and Q. Chen, "Faraday rotation influence factors in tellurite-based glass and fibers," *Applied Physics A*, vol. 120, no. 3, pp. 1001–1010, 2015.

[130] J. Cruz, M. Andres, and M. Hernandez, "Faraday effect in standard optical fibers: dispersion of the effective verdet constant," *Applied optics*, vol. 35, no. 6, pp. 922–927, 1996.

[131] P. A. Ade, D. Chuss, S. Hanany, V. Haynes, B. Keating, A. Kogut, J. Ruhl, G. Pisano, G. Savini, and E. Wollack, "Polarization modulators for cmbpol," in *Journal of Physics: Conference Series*, vol. 155, no. 1. IOP Publishing, 2009, p. 012006.

[132] C. Tan and J. Arndt, "Wavelength dependence of the faraday effect in glassy sio2," *Journal of physics and chemistry of solids*, vol. 60, no. 10, pp. 1689–1692, 1999.

[133] A. Schreckenberger, D. Allspach, D. Barak, J. Bohn, C. Bradford, D. Cauz, S. P. Chang, A. Chapelain, S. Chappa, S. Charity *et al.*, "The fast non-ferric kicker system for the muon g- 2 experiment at fermilab," *Nuclear Instruments and Methods in Physics Research Section A: Accelerators, Spectrometers, Detectors and Associated Equipment*, vol. 1011, p. 165597, 2021.

[134] H. Fujiwara, *Spectroscopic ellipsometry: principles and applications.* John Wiley & Sons, 2007.

[135] G. Westenberger, H. J. Hoffmann, W. W. Jochs, and G. Przybilla, "Verdet constant and its dispersion in optical glasses," in *Passive Materials for Optical Elements*, vol. 1535. International Society for Optics and Photonics, 1991, pp. 113–120.

[136] K. W. Busch and M. A. Busch, "Light polarization and signal processing in chiroptical instrumentation," in *Chiral Analysis.* Elsevier, 2018, pp. 73–151.

[137] B. Jiang, K. Meng, and K. Youcef-Toumi, "Quantification and reduction of poisson-gaussian mixed noise induced errors in ellipsometry," *Optics Express*, vol. 29, no. 17, pp. 27 057–27 070, 2021.

[138] M. Sendelbach, A. Vaid, P. Herrera, T. Dziura, M. Zhang, and A. Srivatsa, "Use of multiple azimuthal angles to enable advanced scatterometry applications," in *Metrology, Inspection, and Process Control for Microlithography XXIV*, vol. 7638. International Society for Optics and Photonics, 2010, p. 76381G.

[139] L. Wasserman, *All of statistics: a concise course in statistical inference.* Springer, 2004, vol. 26.

[140] W. J. Conover, *Practical nonparametric statistics.* john wiley & sons, 1999, vol. 350.

[141] C. Walck *et al.*, "Hand-book on statistical distributions for experimentalists," *University of Stockholm*, vol. 10, 2007.

[142] F. A. Haight, "Handbook of the poisson distribution," Tech. Rep., 1967.

[143] D. Vose, *Risk analysis: a quantitative guide.* John Wiley & Sons, 2008.

[144] W. L. Briggs and V. E. Henson, *The DFT: an owner's manual for the discrete Fourier transform.* SIAM, 1995.

[145] R. Wang, *Introduction to orthogonal transforms: with applications in data processing and analysis.* Cambridge University Press, 2012.

[146] M. Makitalo and A. Foi, "Optimal inversion of the anscombe transformation in low-count poisson image denoising," *IEEE transactions on Image Processing*, vol. 20, no. 1, pp. 99–109, 2010.

[147] J. M. Jarem and P. P. Banerjee, *Computational methods for electromagnetic and optical systems.* CRC press, 2016.